To my loving parents

Mr. M.E. “Saphula mthetho” Sosibo (R.I.P.)

and

Mrs. B.M. “MaMjuda” Sosibo

## THESIS SUMMARY

### Synthesis and Cytotoxicity Studies of Gold Nanoparticle Systems

The thesis entails an in-depth experimental work on modern aqueous and nonaqueous techniques for the synthesis and characterization of colloidal gold nanoparticles of various sizes and functionalities. Further, heterofunctional monolayer protected clusters (MPCs) of gold were synthesized through ligand exchange reactions on gold nanoparticle surfaces. Covalent and noncovalent biofunctionalisation techniques such as carbodiimide coupling, biotin-avidin interactions and Ni-NTA-histidine interactions were used to further introduce proteins and peptides on the surface of the gold nanoparticles resulting in bioconjugates. These systems were characterized using such techniques as TEM, UV-Vis and agarose gel electrophoresis. The three nanoparticle systems i.e. colloidal gold nanoparticles, monolayer protected clusters and bioconjugates were investigated for their inherent biologic effects on live cells through end-point based *in vitro* assays, neutral red and APOP*ercentage*™. The cytotoxicity profiles of the nanomaterials under investigation were elucidated and they showed benign, dose-dependent responses, with higher doses resulting in lower cell viability. This work demonstrated protocols for the synthesis of colloidal gold nanoparticles, MPCs and bioconjugates and subsequently the *in vitro* evaluation of these systems. This work has paved the way for the use of gold nanoparticle systems as drug delivery and diagnostic tools.

# CHAPTER 1: INTRODUCTION

## 1.1. INTRODUCTION

### 1.1.1. Aims and Approach of the Study

The objective of the study is to prepare and develop a number of gold nanoparticle systems that possess surface chemistry that could be utilised in applications such as targeted drug delivery and diagnostics. Specific-reactivity ligands would allow such incorporation of a variety of molecular handles for further surface exploitation. Due to the intended applications of these systems in addressing pharmaceutical and medical applications, their cellular interactions and responses need to be examined. Milestones for this work were set as follows:

a) Synthesis of different sized colloidal gold nanoparticles and monolayer protected clusters (MPCs).
b) Custom surface functionalisation of gold nanoparticles equipped with surface chemical recognition groups.
c) Generation of bioconjugates by surface immobilisation of biomolecules.
d) *In vitro* cellular interactions of the colloidal gold nanoparticles, MPCs and bioconjugates.

The resultant systems should be stable in all environments of application.

### 1.1.2. Gold: A Historical Perspective

In the Middle Ages the developments in Alchemy saw a concerted effort in the art of transmutation, whereupon base metals were supposedly converted into gold, employing the intangible philosopher's stone [1]. The search for the philosopher's stone became so much a subject for the alchemists that a foundation for modern chemistry was laid, through the discovery of physical and chemical properties of many substances used [2]. The cultures of that day sanctified the sun and the lustre of gold was associated with the warmth of the sun and its life-giving light. Gold was subsequently seen as the earthly form of the sun, with its use by the magico-healers from Egypt to India, seeing it crafted as amulets and necklaces that ostensibly protected the wearer from evil spells and spirits that might cause illness [3].

Perhaps the most prominent use of gold was in decorative applications such as ruby glass and colouring ceramics with the most well-known example being the Lycurgus Cup, which formed part of the Roman vessels known as *cage cups* or *diatreta*, that are dated to fourth century A.D. The glass of the cup is dichroic, having a translucent ruby red colour in transmitted light and green colour in reflected light, owing to the presence of gold colloids [4]. Between the 13$^{th}$ and 16$^{th}$ century the alchemists focused on making the gold drinkable, which could promote it to therapeutic applications; the potable gold or *aurum potabile* was a resultant of the discovery of *aqua regia*, the much needed "royal" solvent of gold, prepared by the addition of *sal ammoniac* (ammonium chloride) to *aqua fortis* [5].

In the early 17$^{th}$ century, the drinkable gold found applications in treating conditions such as melancholy since gold "made one's heart happy" [6]. By the late 17$^{th}$ to the early 18$^{th}$ century the use of colloidal gold in highest quality colour manufacturing for pottery and enamels had been established [7], with Purple of Cassius (a combination of colloidal gold and stannic acid) widely exploited in glass, pottery and porcelain works continuing to this day [8]. At that stage, new recipes for the synthesis of gold with therapeutic properties led to the treatment of diseases such as syphilis and scrofula, employing a double chloride of gold [3]. To this day, gold compounds such as gold sodium thiomalate (Myochrysine) and gold thioglucose (Solgonal) are still used for the treatment of rheumatoid arthritis [9].

### 1.1.3. The Nanoscale of Things

Gold in bulk form is an inert, yellowish soft metal having a face centered cubic (fcc) structure with a melting point as high as 1064 °C. Gold has a legendary status of being known as the "king of the metals" or the most "noble" of all the metals, owing to the resistance of gold to surface oxidation. Contrary to the nobility of bulk gold, exciting properties can be attributed to gold at the nanoscale. The interface between the bulk and molecular scales has given birth to matter at the nanoscale, which has fused much excitement to researchers and promises to transform many aspects of materials sciences in the 21$^{st}$ century and beyond.

Materials at this size range obey neither absolute quantum chemistry nor laws of classical physics and have properties that differ markedly from those conventionally expected. This has led to new ways of creating materials and products having a wider range of options through which the process can be influenced. The study of these minute entities has given more focus towards the "neglected dimension" or "fuzzy interface" in materials research, the nanometer size regime, the transition dimension between bulk and molecular regimes. Nanostructured materials are generally referred to as nanoparticles and are characterised by a physical dimension of 1 - 100 nm (from a small atomic cluster to about a single wavelength of near-UV light) [10].

It is interesting to note that metallic (gold) nanoparticles have comparable properties to those of the semiconductor nanoparticles, which have long been studied in detail [11-17]. Similar effects found in semiconductor nanoparticles such as their ability to store excess electrons and positive holes [18], changes in the electronic properties due to surface modifications [19], photoelectron emission [20], and sensitisation of photoreactions of other solutes can also be found in metallic nanoparticles [21]. A brief account of the size related implications of materials in the nanoscale regime is presented in the next section.

### 1.1.4. Nanostructure Effects

The unique properties in the nanosize regime are due to nanoparticles having a high surface-to-volume ratio of their constituent atoms, increased specific surface area and their reduced size in relation to the excitonic radius of the bulk material. The specific area-surface area relationship is given by:

$$\text{Specific surface area} = \frac{4\prod r^2}{\frac{4}{3}\prod r^3 \rho} = \frac{3}{\rho r} \qquad \text{Equation 1.1}$$

where r = radius and ρ = density

The surface area is three orders of magnitude larger at nanoscale as compared to the microscale. In a solid bulk material, the intramolecular bonding energies are much stronger than the intermolecular interactions, meaning the bulk properties can be analysed

as the sum of the individual molecular contributions. The weak intermolecular interactions hardly go beyond the neighbours and the electronic structure of a bulk molecular crystal is therefore independent of the crystal size.

As the particle size is reduced, the ratio of the surface atoms in relation to those in the volume increases, thereby increasing the significance of the surface in determining the properties of the material. In metal nanoparticles, energy level quantization is observed compared to the continuous band as observed in corresponding bulk materials (Figure 1.1).

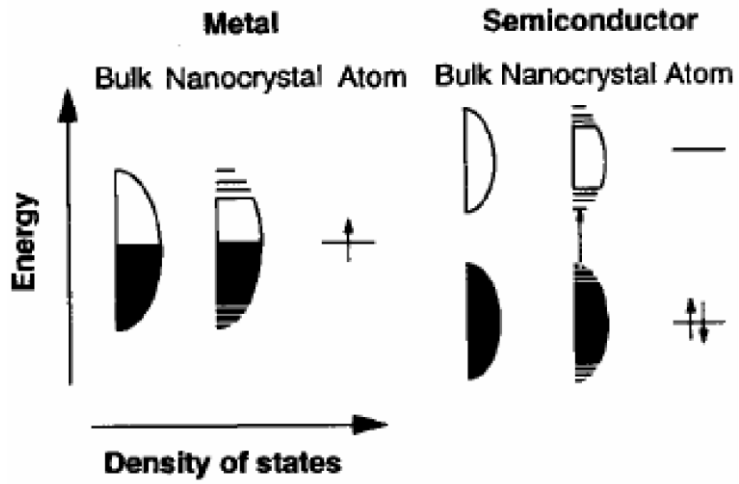


Figure 1.1. *Representation of the transformation of the electronic density of states (DOS) of the valence and conduction bands in metal and semiconductor nanoparticles with comparison to their relevant bulk and atomic states respectively. In metals, the semi-continuous density of states in valence and conduction bands splits into two discrete electronic levels. The level spacing increases with the decrease in particle sizes [22].*

This effect is as a consequence of the confinement of the charge carriers (electrons) within the dimensions of the nanoparticle that is smaller than the bulk delocalisation length. This effect is referred to as the quantum size effect [22-24].

The electronic properties of materials at such small sizes resemble those of a molecule than an extended solid of the same material [25]. The quantum size effect changes the intrinsic properties of the nanoparticles. Generally the surface atoms

contribute to the free energy, and the changes in the thermodynamic properties of nanoparticles such as melting point depression, solid-solid phase transition elevation and can be traced to the quantum size effect [26]. Due to the new and unprecedented properties of these materials, their applications have spawned many different research areas, from molecular biology to nanoelectronics [27-29].

### 1.1.5. Bottom-up and Top-down Approaches

The nanoscale region can both be achieved by bottom-up (solution synthesis of nanoparticle assemblies) and top-down (precision engineering and lithography) approaches. A bottom-up approach is ubiquitous in nature, involving the use of small molecular clusters as the building blocks for nanosized and macrosized shapes and structures. Self-assembly is another form of patterned growth that employs the workings of the bottom-up approach. This approach mimics biological systems by utilising order-inducing factors that are immanent to the system. It therefore can be referred to as a process of "growing" structures [30]. This approach offers simplicity which could go as low as atomic scale, assembling of multi-dimensional structures and potential affordable scaling-up of the materials.

The drawback in the bottom-up techniques is the near impossible prospect of arresting growth at the same time for all the nanoparticles in solution. The top-down fabrication approach involves scaling down of larger materials into the desired shape and size. The order of the desired product is imposed through the preparation process. Many commercially important techniques such as electron beam lithography, photolithography and etching are used in the top-down fabrication of self-assembled structures [31-33]. This technique suffers because of complexity, cost and uncontrollable anisotropy in the case of chemical etching of structures.

## 1.2. SYNTHESIS OF NANOPARTICLES

Synthesis methods for the preparation of nanoparticles have to be reproducible, yielding nanoparticles of a predetermined size, structure, shape and composition [27, 34-37]. A systematic study of synthesis and colours of gold colloids was reported in 1857, through the work of Michael Faraday [38]. In a two-phase reaction, Faraday reported the

formation of ruby red colloidal gold solutions by reducing a gold salt with phosphorus in carbon disulfide. He further studied the interactions of light and the thin films of dried colloids, observing a reversible colour change upon compression. Since this pioneering work, many procedures have been reported for nanoparticle synthesis, reactions and functionalisation. Commonly used methods include transition metal salt reduction, ligand reduction and displacement from organometallics, electrochemical synthesis among many others.

A description of a pick of the leading three methods (citrate-reduction, two-phase Brust-Schriffin and the polyol method) is described, and an account of other techniques is presented next.

### 1.2.1. Citrate Reduction Method

Possibly the most popular wet chemistry method of metal nanoparticles synthesis is the tetrachloroaurate reduction by citrate in water, devised by Turkevitch *et al.* in the 1950s [39, 40]. The experimental observation of the colour changes from pale yellow, colourless, dark blue, purple and then ruby-red has sparked an unprecedented interest in the studies of the citrate-capped gold nanoparticle evolution. Chow *et. al.* studied the structural evolution of the gold nanoparticles under different conditions, employing lower temperatures (50-80 °C) and different citrate-to-gold concentrations [41]. They found the initial transition from dark blue to red on reduction of the gold(III) by citrate, to be associated with the decrease in particle sizes. The large transitory particles were spherical in shape (100 - 200 nm) and composed of smaller and well defined subunits of spherical gold nanoparticles (5 - 15 nm).

Studies by Peng *et. al.* observed that the formation of gold atoms is followed by nucleation resulting in the formation of small nanoclusters of about 5 nm. These nanoclusters assemble in a linear-like fashion into an extensive network of nanowires [42]. More Au atoms adsorb increasing the diameter of the nanowires, subsequently destabilising them. The wires undergo fragmentation and cleave into spherical particles. Aging and Ostwald ripening lead to well-defined spherical citrate-capped gold nanoparticles [43]. The formation of the nanoparticles could be controlled, leading to the synthesis of pre-chosen nanoparticles sizes [44]. In that account, Frens reported the

variations of the ratio between reducing/capping agent to gold to manipulate the sizes of the nanoparticles. The change in the citrate concentration changes both the reduction rate and the nucleation-to-growth ratio, thus blurring the distinction between the stabilising and reducing actions of the citrate.

A wide range of particle sizes have been synthesised using this method (~10 - 150 nm), although polydispersity and morphological variations have been observed for nanoparticles larger than 30 nm [45]. A range of nanoparticle sizes (15 -120 nm) have also been reported, synthesised by variations in the pH of the starting gold salt solution [46]. Henglein *et al.* have reported the synthesis of citrate capped silver nanoparticles [47]. Silver nanoparticles prepared by this method showed limited particle size control [48]. It was further noted that various acids, which are oxidation/decarboxylation products of citrate can be chemisorbed onto the particles and affect the particle growth. Platinum colloids of very small sizes have been synthesized via the citrate method [49, 50]. Palladium nanoparticles can also be synthesised using this route [51]. Kumar *et al.* reported a full kinetic Monte Carlo simulation model for the prediction of particle sizes by varying the citrate-to-gold ratio [52].

### 1.2.2. Two-Phase Reduction: Brust-Schiffrin Method

The use of alkanethiolates of different chain lengths as capping agents for gold nanoparticles can be traced back to 1993 in a report by Giersig *et al.*[53]. The method developed by Brust *et al.* in 1994 has gained tremendous popularity in gold nanoparticle synthesis [54]. This two-phase redox reaction involves dissolving $AuCl_4^-$ in water and transfer of $AuCl_4^-$ into the toluene layer by the action of a phase-transfer reagent, tetraoctylammonium bromide (TOABr). The addition of an alkanethiol reduced gold(III) to Au(I), forming as an alkylthio complex. The addition of a strong reducing agent, sodium borohydride caused a reductive decomposition of the complex leading to nucleation of the metal cluster, and simultaneously the formation of a thiolate monolayer on the surface [55]. This process can be summarised in the following equations:

$$AuCl_4^-(\text{Aqueous}) + N(C_8H_{17})_4^+(\text{Toluene}) \longrightarrow N(C_8H_{17})_4^+AuCl_4^-(\text{Toluene}) \qquad \text{Equation 1.2}$$

$$m AuCl_4^-(\text{Toluene}) + nC_{12}H_{25}SH(\text{Toluene}) + 3\,me^- \longrightarrow 4mCl^-(aq) + (Au_m)(C_{12}H_{25}SH)_n(\text{Toluene}) \qquad \text{Equation 1.3}$$

A one-phase reaction has also been reported as a modification of the two-phase protocol [56]. Since this study, a spate of research has gone into developing other suitable capping ligands, including thiol-, amine-, silane-, phosphine and disulfide-based capping ligands [57]. Surface ligand exchange strategies have also been widely formulated for further exploitation of the gold core properties [58].

Particles of sizes ranging from 1 - 10 nm could be synthesised by varying the stabiliser/gold ratio. The resultant nanoparticles synthesised by this method showed tremendous stability. They could be dried, treated as simple chemical powders and re-dispersed in solvents as colloids [54]. Subsequent observations on this reaction were reported by Templeton *et al*., also reported that (i) larger thiol:gold mole ratios give smaller particle sizes (ii) fast reductant addition and cooled solutions produce smaller, more monodispersed particles, and (iii) quenching the reaction immediately following reduction produces an abundance of very small core sizes (less than 2 nm) [59].

Thiol-functionalised platinum nanoparticles have been reported, using a superhydride as a reducing agent. Nanoparticles with an average size of ~3 nm were obtained capped with octanethiol [60]. Palladium nanoparticles have also been reported to be synthesised by the action of triethylborohydride on a palladium chloride salt in tetrahydrofuran (THF) resulting in small monodispersed nanoparticles at sizes between 1.3 - 4 nm [61]. Very small (1 - 2 nm) nanoparticles of copper have been synthesised by this method. The particles showed remarkable structural modifications after prolonged low temperature thermal annealing. A mixture of spheres, rods, hexagons, pentagons, diamonds and triangles resulted, with the spheres most predominant [62].

### 1.2.3. Polyol Reduction Method

Another method that has gained popularity involved the reduction of a metal salt in the presence of a protecting polymer, usually poly(vinyl pyrolidone) (PVP). This method developed by Figlarz *et al.* entails refluxing the metal precursor (oxides, nitrates and acetates) in ethylene glycol or polyols (polyethelene glycol (PEG)) in the presence of a polymer for a specific period [63]. This method is commonly referred to as the polyol method. Investigations into the reaction mechanism showed a solution based reduction

pathway. This meant that the nanoparticles are formed by nucleation and growth from the solution with the polyol acting as a solvent for the inorganic compound due to its high dielectric constant.

The reaction mechanism involves two stages; (I) the conversion of the inorganic precursor into the intermediate phase in a stepwise sequence, (1) progressive dissolution of the starting inorganic precursor material, and (2) precipitation of the intermediate phase; (II) the conversion of the intermediate phase to the metal particles in a stepwise reaction involving (1) the dissolution of the intermediate phase, (2) reduction in solution, (3) evolution of the volatile products and (4) spontaneous nucleation and growth of metal particles [63]. Tekaia-Elhsissen *et al.* reported the synthesis of monodispersed nanoparticles of Au, Pt, Pd, Ru and Ir by the polyol route, in each case obtaining highly defined nanoparticles of small sizes [64]. The effect of the PVP concentration was also investigated, showing a decrease in average particle size of silver nanoparticles with an increase in PVP concentration [65].

Rao *et al.* prepared nanoparticles of gold via the polyol method demonstrating the effect of pH on the particle sizes observing that the particle sizes increased with the increase in pH [66]. Generally the use of the polyol is advantageous in that the glycol is adsorbed onto the nanoparticle surface, minimising particle surface oxidation.

### 1.2.4. Sonochemical Route

When substances such as water are subjected to strong ultrasound irradiation, it leads to the formation, expansion and collapse of cavitation bubbles by the acoustic fields [67]. The result of which is the production of high-pressure fields at the centers of the bubbles, in a process called acoustic cavitation [68]. This causes the dissociation of the interior water vapour into H and OH radicals. These radicals initiate a sequential abstraction and reduction reactions of dissolved molecules. The estimated temperature of the hot spot has been estimated to be 5000 K, a temperature at which most molecules can be decomposed or reduced [69]. Sonochemical reactions usually employ alcohols such as 2-propanol or surfactants such as sodium dodecyl sulfate (SDS) or a combination of the two as radical scavengers in the colloid formation. An additional polymer has also been incorporated as

a stabilizer. Different nanoparticle types have been synthesized this way including Au [70, 71], Ag [72, 73] and CdS [74].

### 1.2.5. Synthesis in Confined Matrices

The need to manipulate both optical and electronic properties of nanoparticles requires control over their spatial arrangement in 2D and 3D arrays [75]. Materials with distinctly defined cavities (porous or layered) can be employed as host materials in which nanoparticles can be synthesised with properties of the resultant nanoparticles dictated by the microstructure of the host. Zeolites molecular sieves are examples of these matrices. Zeolites, in their natural or synthetic forms, have a 3D aluminosilicate structure and have long been used as hosts to synthesise nanoparticles [76, 77]. Porous alumina [78, 79] and reverse micelles [80, 81] have also been used as hosts for the reduction of metal salts to form nanoparticles.

Pileni *et al.* reported the synthesis of highly monodisperse silver nanoparticles by using a functionalized bis(2-ethylhexyl)sulfosuccinate reverse micelle [82]. Another surfactant that has received as much attention is cetylmethylammonium bromide (CTAB) [83, 84]. Copper nanoparticles have been synthesised similarly [85]. Different metal nanoparticles have been synthesised using the microemulsion method including Rh, Pd, Ir [86], Ni [87] and Co [88]. A common observation was that the particle sizes varies with the water content of the micelle; with larger water contents producing bigger particle sizes.

### 1.2.6. Chemical Vapour Deposition (CVD) Route

CVD is an industrially important tool for the deposition of thin films on a variety of substrates [89, 90]. There is no single universal CVD equipment, but it is individually tailored for specific materials, and whether it is used for research and development or for commercial production. Generally the CVD apparatus consists of three main components, (i) the chemical vapour precursor supply system, which functions by generating the precursor vapour and then supplying it to the reactor chamber, (ii) the CVD reactor which conventionally contains a loadlock for the transport and placement of the substrate, a substrate holder and a heating system with a temperature control and (iii) the effluent gas

handling system, serving to remove by-products and unreacted precursor material.

Formation of the nanosized film takes place in a series of steps (i) the generation of a vapourised gaseous material source, (ii) transportation of the source into the reaction chamber, (iii) phase reactions of the reactants leading to the formation of the intermediate species, (iv) the adsorption of the source onto the hot substrate, (v) diffusion of the heated deposit along the host substrate, forming crystallization centers and subsequent film growth, (vi) the by-products are removed from the boundary layer through diffusion/convection. The deposition temperature can be varied anywhere between 100 – 1000 °C, depending on the substrate and the target deposit. Highly monodispersed Au has been deposited with a variant of CVD, aerosol assisted CVD (AACVD) [91], using $HAuCl_4$ as the metal precursor in the presence of tetraoctyl ammonium bromide (TOABr). Other materials such as carbon nanotubes have been made using this technique [92].

### 1.2.7. Solvothermal/ Hydrothermal Route

The synthesis of nanoparticles inside sealed vessels (steel bombs and autoclaves) can be achieved by elevating the solvent temperature above its boiling point by increasing the autogenous pressures through heating. This process increases the solubility and reactivity of most inorganic complexes and salts at such critical solvent temperatures. Reactions performed this way are referred to as solvothermal processing and hydrothermal processing if water is used as a solvent [93 - 95]. Nanocrystalline phase-pure rutile ($TiO_2$), which is an important photocatalyst has been reported hydrothermally processed by a controlled hydrolysis of $Ti(OEt)_4$ in ethanol [96]. Other oxides such as $CeO_2$, an important catalyst in motor engine catalytic converters, [97] and $\gamma$-$Fe_2O_3$ [98] have been synthesised hydrothermally.

Nanoparticulate chalcogenides, MSe (M = Zn, Cd) have been hydrothermally prepared by heating the metal and Se powder in an autoclave at 180 °C [99]. CdSe nanoparticles were synthesised by incorporating trioctylphosphine oxide (TOPO) as a capping agent [100]. $MSe_2$ and $MS_2$ (M= Ni, Co, Fe, Ni, Mo) were hydrothermally prepared using metal chloride salts and $N_2S_2O_3$ or $Na_2SeSO_3$ as starting materials [101].

Other enhancements, such as microwave-hydrothermal method have been specially developed to synthesise nanostructured mesoporous materials [102].

### 1.2.8. Biosynthesis Route

The "greening" of nanoparticle synthesis and assembly requires the development of environmentally benign synthetic protocols, involving a minimum number of steps, employing less toxic materials, involving as few reagents as possible under commonly prevalent laboratory conditions. This has led to a plethora of biomimetic synthetic approaches for the synthesis of nanomaterials and the subsequent growth of advanced structures [103]. The most commonly observed instances of inorganic materials synthesised by microorganisms include magnetite nanoparticles (magnetotactic bacteria) [104] siliceous materials (diatoms) [105] and gypsum and calcium carbonate layers (S-layer bacteria) [106].

Inorganic metal salt ions are generally toxic to most microorganisms, resulting in the said microorganism activating defence mechanisms once in contact with these foreign species. This process culminates in the change of redox states of the foreign ions inside the cell that form the core of microorganisms being applied in areas such as bioremediation, nanoparticle synthesis and microbial corrosion [107]. Both eukaryotic (yeast) [108] and prokaryotic (bacteria) [109] microorganisms have been shown to produce nanoparticles within their cell walls. Gold [103] and silver nanoparticles [103] have been synthesised by reacting the metal salt ions with *Verticullium*, a genus of fungi in the genus of Ascomycota, resulting in the intracellular deposition of nanoparticles. The fungus *Fusarium oxyporum* has been reported to produce important semiconductor nanoparticles, such as CdS [103c]. *Klebsiella aerogenes* bacterium has also been used to synthesise CdS nanoparticles [110]. *Lactobacillus* strains, which are present in buttermilk, have been used for large-scale production of silver and gold alloys when exposed simultaneously to the metal salts of both metals [111].

## 1.3. FORMATION OF THE NANOPARTICLE

The formation of the nanoparticles follows a simple process first investigated by LaMer *et al.* in formation of the sulphur sols [112]. Considerable attention has subsequently been afforded to the understanding of these processes. An exhaustive summary is presented next.

### 1.3.1 Precipitation of Nanoparticles

The nanoparticle formation in solution occurs via a chemical reaction, forming stable nuclei followed subsequently by growth of the nanoparticle. This process is often referred to as precipitation. When a multicomponent material is required, co-precipitation takes place instead in a systematic combination of materials. Special care is needed in the conditions for the latter process if chemical homogeneity is sought. This becomes important when the ions in solution precipitate under different conditions, such as pH and temperature. Once the reactants (reducing agents and metal salts) are mixed together in a solvent of a specific dielectric constant, the chemical reaction occurs and the product supersaturates the solution, driving the chemical system far from the minimum free energy configuration [112b].

The reaction design is generally such that the products have a reasonably low solubility and reach supersaturation quickly. Condensation of the formed nuclei of the product restores the thermodynamic state of the reaction system. The size of the resultant nanoparticles is sandwiched between the kinetic factors and the competing thermodynamics in particle growth with the kinetic factors affected by reactant concentration, reactant addition order, temperature, pH and stirring rate; the structure and crystallinity of the nanoparticles is influenced by reaction rates [113]. The morphology of the nanoparticles is controlled by supersaturation, nucleation and growth rates, colloidal stability and secondary processes such as Ostwald ripening and aggregation [114]. Small, well-formed nanoparticles are formed at low supersaturation, with their shape depending on the crystal structure and surface energies. Larger particles form at higher supersaturation, with smaller compacted agglomerated particles forming at even higher supersaturation levels. Particle growth in solution is interface-controlled when the

particles are small, and after reaching a certain critical size becoming diffusion-controlled.

The conditions to achieve monodispersity can be deduced from the LaMer diagram (Figure 1.2**)**: (i) the nucleation process must not be lengthy, but rather an explosion of nuclei must be formed in a short space of time, ii) the nuclei growth must be fast enough to limit the overall number of particles forming and (iii) the growth rate must be slow enough and drag on compared with the nucleation process, resulting in fine particles as a consequence of the finite nucleation period [115].

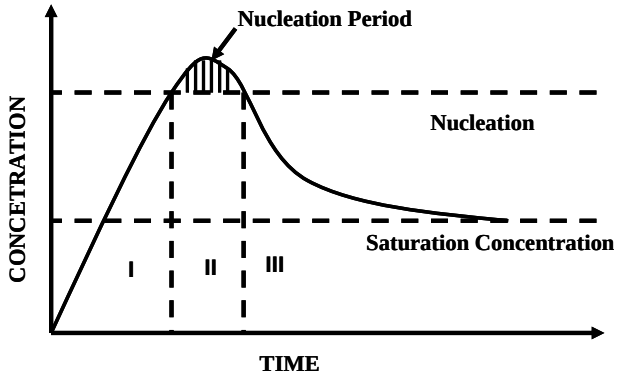


Figure 1.2. *The LaMer diagram, showing the time dependence of the concentration required to achieve monodispersity [112]. I. Prenucleation phase, II. Nucleation stage and III. Growth step.*

Tailoring the monodispersity of the nanoparticles can be engineered by controlling these processes.

### 1.3.2. Stabilisation of Nanoparticles

Fine particles in the nanosize range have a tendency to approach and then separate through Brownian motion [116]. Random agglomeration of the nanoparticles takes place, when the particles form larger aggregates and settle due to their weight. This is further enhanced by the large surface area of the nanoparticles, which heightens their van der Waals interactions. Nanoparticles have only kinetic stability, and the process of aggregation allows them to form bulk, which in turn affords them thermodynamic stability. Chemical synthesis methods have to therefore be devised such that there is a

balance between the attractive forces. The stabilisation process can be achieved in two ways: electrostatic (or charge or inorganic) and steric (or organic) stabilisation. The electrostatic stabilization is achieved as a result of the formation of an electrical double layer (likely multi-) or "counterions" arising from the charged ions absorbed on the surface of the particle. If the electrostatic repulsion is high enough, Coulombic repulsions between the nanoparticles will prevent agglomeration [Figure 1.3].

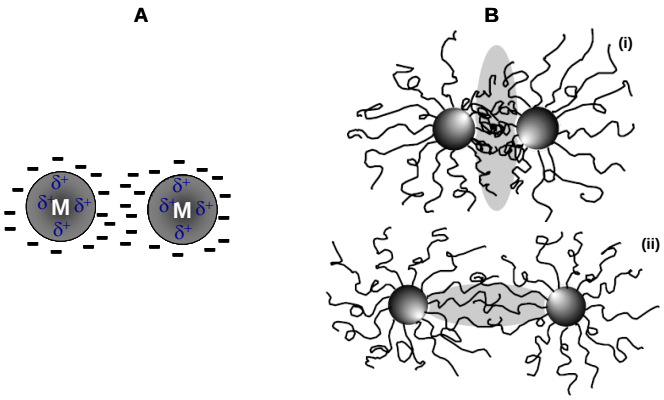


Figure 1.3. *Electrostatic stabilisation (A), charged ions adsorb on the surface of the metal nanoparticle creating an electrostatic double layer providing a Coulombic repulsion between the nanoparticles. Steric-stabilisation (B), of the nanoparticles by bulky ligands or polymers: (i) entropic effect and (ii) osmotic effect.*

The net repulsive or attractive forces between particles are therefore the sum of the attractive and repulsive van der Waals forces. The Derjaguin-Landau-Verwey-Overbeek (DLVO) theory describes attractive and repulsive forces as a function of distance [117]. Steric stabilization can be attained by surrounding the nanoparticles with sterically bulky materials, such as surfactants and polymers (Figure 1.3b). The adsorbates form a steric barrier preventing contact between the particles. Two effects describe this stabilisation mode, the volume restriction contribution (entropic contribution) and the osmotic contribution and they both contribute to the interaction free energy, $DG_s$ [118].

### 1.3.3. Full-Shell "Magic Number" Clusters

Nanoparticles, as an ensemble of clusters of atoms, have properties dictated by the bonds between these atoms. Similarly to gaseous materials, held together by weak van der

Waals forces, metallic clusters are much more strongly held together by delocalised nondirectional bonds. Metallic clusters with a complete, regular outer shell of atoms are assigned full-shell or "magic number" clusters [119], depicted in Figure 1.4.

| "Magic Number" Clusters | | | | | |
|---|---|---|---|---|---|
| **No. of Shells** | 1 | 2 | 3 | 4 | 5 |
| **No. of Atoms** | $M_{13}$ | $M_{55}$ | $M_{147}$ | $M_{309}$ | $M_{561}$ |
| **% Surface Atoms** | 92% | 76% | 63% | 52% | 45% |

Figure 1.4. *Idealised representation of hexagonal close packed full-shell 'magic number' clusters [119].*

The shells are constructed in a succession of packed layers or shells of atoms around a single atom. The full-shell cluster contains $M = 10n^2 + 2$ metal atoms, per *n*th shell, where *n* is an integer ($n > 0$) [120]. The full-shell imparts stability and provides the maximum possible number of metal-metal bonds [35].

## 1.4. APPLICATIONS OF NANOPARTICLES

A comprehensive plethora of applications have surfaced for nanosized materials. Major strides have gone towards the development of systems based on nanoparticles, with device prototypes already in testing phases for many areas. The promise brought by nanotechnology has seen this area of research become one of the priority funding areas for many governments, with applications to simplify and add improve life. A select group of applications is presented in the next few sub-sections.

### 1.4.1. Biological Applications

Numerous numbers of applications of nanoparticles have appeared in molecular biology and medicine in recent years. The governing factors for the applicability of the nanoparticles include, particle sizes, particle surface functionalities and zeta potential, biocompatibility, solubility in target media, cytotoxicity and fate and ability to protect the

cargo and controlled release in case of delivery applications. Mirkin *et al.* developed a "simple and quick" yet powerful colorimetric nanoparticle-DNA conjugates-based detection device for nucleotides, proteins and metal ions; with high specificity that allowed specific genetic sequences to be isolated in solution [121]. Gold colloids have also been applied in biomolecular detection of single-strand DNA as fluorescent quenchers [122].

Colloidal gold nanoparticles have been used for targeting cancerous cells in human body motivated by its non-toxicity biocompatibility and insusceptibility to photobleaching as compared to conventional diagnostic dyes [123]. The growth of tumours by the formation of new blood vessels can be countered by the use of the antiangiogenic properties of gold nanoparticles [124]. Non-invasive radiofrequency thermal destruction of tumour cells has been demonstrated using gold nanoparticles [124b]. Fluorescent quantum dots have been used as powerful optical contrast agents for monitoring cellular events and imaging tumors *in vivo* [125]. Strategies for tumor-targeted drug delivery of *in vivo* and *in vitro* reagents, employing gold nanoparticles coupled with specific targeting vectors have been reported [126].

Superparamagnetic iron oxide nanoparticles (SPION), in conjunction with high resolution magnetic resonant imaging (MRI) have been used to locate small lymph-node metastases in prostate cancer patients [127]. Targeted delivery and imaging techniques have been exploited using different nanoparticle systems, from colloidal gold to polymeric micelles [128]. Many different strategies and the benefits of materials for biological applications are reviewed elsewhere [129-131].

### 1.4.2. Chemical and Materials Applications

The large surface area of nanoparticles make them attractive heterogeneous catalysts, with atoms in vertexes and edges (in addition to facial atoms), imparting properties similar to those of supported catalysts. This availability of atoms is essential for the chemisorption of species in heterogeneous catalysis [132]. Nanosized $Rh_{55}$ particles have been reported in the hydroformylation of ethane, with high yields in solusion [133]. The reduction of carbon dioxide by colloidal gold at room temperature has been exploited in the removal of carbon monoxide from hydrogen feeds in fuel cells [134]. Supported gold

nanoparticles can efficiently oxidise CO at temperatures as low as 0 °C [135]. Grisel *et al.* investigated the effect of gold nanoparticle sizes and oxidic additives and the selectivity of oxidation of CO in the presence of hydrogen. Particles of sizes smaller than 5 nm had the highest activities [136].

Metal nanoparticles play an important role in photonics as non-linear optical materials, a favourable choice over inorganic crystals such as $LiNbO_3$ [137]. Boron- and posphorus-doped silicon nanowires have been fabricated for applications as building blocks for nanoscale electronics [138]. In the quest for nanocomputing and miniaturisation of biological sensor arrays, crossed semiconductor nanowire field-effect transistor (cNW-FET) arrays, have been modified at nano-/molecular levels [139]. Single-electron transistors (SET) and non-electronic digital circuits have been fabricated using gold nanoparticles supported on a $MoS_2$ substrate [140].

## 1.5. PROPERTIES OF METAL NANOPARTICLES

### 1.5.1. Optical Properties

The d-orbital electrons of gold are free to travel through the nanoparticle. The average free path for gold is approximately 50 nm meaning no scattering is expected for particles smaller than this size with all the interactions occurring at the surface [141]. The electrical field of an incoming light wave causes polarisation of the free conduction electrons with respect to the heavier ionic core of a spherical nanoparticle [141b] (Figure 1.5).

Due to the movement of electrons under the external field, there is a general displacement of negative charge (electrons) from the positive one, resulting in a net charge difference at the nanoparticle boundary [141, 143]. A dipolar oscillation of all the electrons with the same phase is created in a process called surface plasmon oscillation [141, 142]. When the incoming electromagnetic field becomes resonant with the coherent electron motion, a strong absorption is observed in the spectrum [143]. The frequency and the surface plasmon absorption have been found to depend on the shape, size, dielectric constants of the metal nanoparticle and the solvent and also the state of aggregation [143-145].

For non-spherical particles, such as nanorods and nanowires, the orientation of the electromagnetic field determines the resonant wavelength, resulting in two distinct

oscillations, transverse and longitudinal [142]. Changes in shape and size bring changes in the oscillation frequency of electrons, generating different cross-sections for absorption and scattering properties [142-145]. The vivid colour of gold colloids of different sizes and morphology emanates from this process. It has been shown that plasmons do exist in bulk and at the surface of large chunks of materials but are downplayed by the mismatch between the plasmon dispersion relation and that of a photon, meaning no plasmon excitation can be achieved by ordinary plain-wavelength light [142].

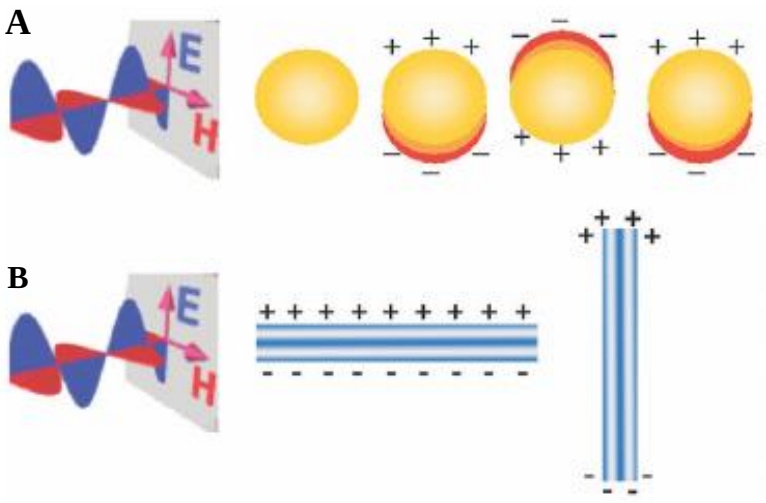


Figure 1.5. *Origin of the surface plasmon resonance caused by the interactions of the nanoparticle electron in the conduction band with electromagnetic radiation. (A) A dipole is induced, oscillating in phase with the electric field of the incoming light. (B) Transverse and longitudinal oscillation of electrons in a metal nanorod [142].*

In contrast, smaller particles do not require momentum conservation and their plasmons can be excited by ordinary light. This observation results in the shift of the plasmon resonance towards the visible region of the electromagnetic spectrum for the noble metal nanoparticles (gold, copper and silver) resulting in fascinating colloid colours [147]. For smaller clusters, the surface and the bulk plasmon are coupled, and the charge density varies everywhere in the nanoparticle [146d,e]. Generally, the majority of the transition metals show a broad and poorly resolved absorption band in the ultraviolet (UV) region

with the strong coupling between the plasmon transition and the interband excitation responsible for such a difference [143]. Furthermore, the conduction-band electrons of the noble metals can be approximated by the Drude free-electron model, which assumes that the conduction-band electrons can be treated independently from the ionic background and can move freely as some sort of an "electron gas".

The "electron gas" allows higher polarisability in the noble metals, which shifts the plasmon resonance to lower frequencies and giving a sharp bandwidth. Accordingly, the conduction electrons in a spherical particle act as an oscillator system, whereas in bulk materials the Drude frequency is not excited by light and the conduction electrons are viewed as a relaxer system. The linear optical properties such as extinction and scattering of small spherical particles accounting for the surface plasmon resonance (SPR) were first described theoretically by Mie in 1908 [148]. This feat was achieved by solving Maxwell's equation for the spherical particle with appropriate boundary conditions; postulating that the optical properties of the particle can be calculated from the optical constants of the bulk metal, having the same macroscopic, frequency-dependant internal dielectric constant. This is despite the particle properties varying markedly from those of the corresponding bulk [149]. Numerous reports have surfaced correlating the spectroscopic behaviour of gold and other noble metal nanoparticles to the Mie theory [150].

## 1.6. FUNCTIONALISATION OF GOLD NANOPARTICLES

### 1.6.1. Monolayer Protected Clusters (MPCs)

Highly stable alkanethiolate-capped gold monolayer protected clusters (MPCs) are generally synthesised using the Brust biphasic protocol [54]. These MPCs however, are insoluble in water and this therefore limits their applications in biology and medicine since they are incompatible with biomolecules. For this purpose, the incorporation of polyethylene glycol imparts water solubility, biocompatibility as well lowering non-specific interactions of these materials with biomolecules [151]. Wuelfing *et al.* reported the synthesis of α-methoxy-ω-mercapto-poly(ethylene glycol) (PEG-SH, $M_w$ = 5 000)-capped gold MPCs, possessing higher thermal stability compared to the alkanethiolate

counterparts and not amenable to ligand place-exchange reactions due to the steric repulsion effects of the PEG polymer [152].

Otsuka and co-workers reported the synthesis of gold MPCs functionalised with α-acetal-ω-mercapto-PEG-SH ($M_w$ = 3 090), a heterobifunctional PEG allowing for immobilisation of further molecules such as galactose and mannose [153]. Short-chain ethylene glycol ligands of formula: $CH_3(OCH_2\text{-}CH_2)_nSH$ (where n = 2, 3 and 4) have been reported as capping agents for gold MPCs, introduced through the ligand place-exchange of the hexanethiol on the surface of the gold [154]. The lack of steric bulkiness allowed these MPCs to undergo further ligand place-exchange reactions. Hong *et al.* reported the synthesis of magnetic FePt nanoparticles with a mixture of two heterobifunctional PEG ligands having dopamine and carboxyl groups at the secondary terminal, named as mixed monolayer protected clusters (MMPCs) [155]. Such materials serve as building blocks for immobilisation of a multitude of biomacromolecules on the same cluster system yielding higher order hybrid inorganic-organic materials [155b]. An account of the PEG ligand is presented next.

### 1.6.2. Poly(ethelene glycol) (PEG)

#### *1.6.2.1 Introduction*

Poly(ethelene glycol) (PEG), also known as poly(ethylene oxide) (PEO) is a tethered, hydrophilic, non-toxic and non-ionic polymer that has established applications both in biochemistry and industry. The benign properties of PEG have allowed applications such as in cosmetics, pharmaceutical products and food additives, PEG is Food and Drug Admimistration (FDA)-approved for internal ingestion [156]. PEG is a common liquid-liquid partitioning reagent for biomolecules and has been widely used as a precipitation reagent for protein crystallisation, a crucial step in protein studies. The use of PEG for model investigations also extends to the study of protein-protein and protein-PEG interactions in water ternary systems [157].

Conventionally, PEG has a linear or branched structure terminated by hydroxyl groups at both ends: $HO\text{-}(CH_2CH_2O)_n\text{-}CH_2CH_2\text{-}OH$. PEGs are generally available with molecular weights ($M_w$) of between 1 000 to 20 000 Da. PEG is well-known for rejection of non-specific adsorption of proteins and other macromolecules on metal surfaces [151].

The incorporation of PEG, commonly referred as PEGylation, in drug materials imparts a stealth character in the blood stream, affording long-circulation times, biocompatibility and reduced antigenicity and immunogenicity [158]. The attachment of the PEG moiety enhances the delivery of parenteral agents. This process alters the pharmacokinetic properties of the therapeutic reagents, subsequently modifying the pharmacodynamics through a mechanism involving the change in binding properties of the native reagents [159].

PEG reduces the renal clearance and thus increases the absorption after subcutaneous administration (such as injections) of agents and thus restricts the distribution, and only maintaining high drug concentrations at or near to the target area for a prolonged period. Eventual removal of the PEG can be controlled by the molecular weight, with only $M_w \leq$ 50 000 Da removable through the kidneys, avoiding any long-term toxic accumulation of the spent PEGylated delivery agents [160]. The qualifying properties of PEG in the design of carriers in the blood system for either drug delivery, imaging systems and other site-specific targeting entities can be summarised as follows [161-163]:

i. It is relatively small in size (< 5 μm).
ii. Biodegradability in the blood system.
iii. Ability to withstand harsh conditions without aggregation and other structural modifications.
iv. High loading efficiency of the delivery agents (> 30%)
v. High entrapment efficiencies (> 80%)

Biomolecules such as albumin and galactose have been shown to have blood clearance duration of less than twenty seconds, diminishing any prospective standalone applications in delivery and imaging, but can be improved though PEGylation [162].

#### *1.6.2.2. Synthesis of PEG*

The synthesis of PEG and its derivatives have been investigated by Huang *et al.* by synthesising a thiol-monofunctionalised PEG (PEG-SH) by a series of polymerisation steps [164]. Methacryloyl-functionalised PEG has been prepared by anionic

photopolymerisation of ethylene oxide with amino functional initiators and termination of the functional ends with methacryloyl chloride [165]. Different functionalities can be incorporated onto the PEG chain resulting in monofunctional (with a nonreactive methoxy group and a reactive group such as amine on one end), homobifunctional (two similar reactive groups on both termini) and heterobifunctional (two different reactive groups on both ends) [166].

Apart from the incorporation of common functional groups such as amine, hydroxyl, carboxyl among others, higher molecular weight groups have been incorporated, such as maleimide, vinylsulfone and many more have been grafted onto the PEG [167]. PEG has extensively found use in the synthesis of copolymers as the hydrophilic block in association with other hydrophobic polymeric blocks [168-170]. PEG has been successfully conjugated to many biological macromolecules such as proteins, polypeptides, lipids, carbohydrates, drugs and other bioactive molecules [171].

### 1.6.3. Monolayer Protected Nanoparticle Reactions

The introduction, replacement and modifications of surface functionalities on monolayer protected clusters can be achieved by the ligand place-exchange or simply organic or inorganic reaction of the ω-terminal ligand. A selection of the most common methods is presented next.

#### *1.6.3.1. Ligand Place-Exchange Reactions*

Nanoparticles with a thiolated monolayer surface coverage can be functionalised into materials with electrochemical and catalytic properties via ligand place-exchange reactions. This is useful in the formation of poly-homo and -hetero-functionalised MPCs [59]. A typical example is given in the equation below for the functionalisation of the MPCs with R'S thiolate group.

$$x(R'SH) + (RS)_mMPC \rightarrow x(RSH) + (R'S)_x(RS)_{m-x}MPC \qquad \text{Equation 1.4}$$

The rate and extent of the ligand-exchange is dependent on the chain-length and steric bulkiness of the original ligand on the MPCs [172]. Subsequent investigations into the

mechanism of this reaction has shown that: (i) a 1:1 stoichiometric replacement, with each incoming ligand replacing only molecule on the surface, liberated as a free thiol, (ii) there is no participation of disulfides or oxidised thiolated species, (iii) the rate is much more pronounced on the vertexes and edges compared to the terraces, (iv) it is thermodynamically and kinetically responsive to positively charged cores and (v) it is an associative mechanism [58a,d, 173, 174]. Many functional groups have been incorporated onto monolayer-protected clusters via the ligand place-exchange, such as anthraquinone [175], galvinol [176] and ferrocene [177].

#### *1.6.3.2. Acid-Amine Coupling Reactions*

Monolayers containing a ω-carboxylic acid group can react with an amine moiety in the presence of coupling reagents. Generally, a combination of N-hydroxysuccinimide (NHS) and 1-ethyl-3-(3-dimethylamino propyl)-carbodiimide (EDC) is employed as the coupling reagents for the covalent linkage of entities on the particle surface. The ω-amino-functionalised nanoparticles have been shown to attach -COOH-derivatised carbon nanotubes [178]. The carbon nanotubes were functionalised through acid washing, which oxidised and created an open end termini of the nanotube stabilised with -COOH. Ferrocene has also been introduced onto the surface of magnetite particles this way [179]. This method is advantageous in that: (i) amide and ester formation is versatile and well-known, (ii) there is limitless variety in the choice of targets for amine and carboxylic acids, (iii) the activating agents are both powerful and readily available [180].

#### *1.6.3.3. Polymerisation Reactions*

Nanoparticles functionalised with polymeric ligands can be used as building blocks for the fabrication of highly functional materials. Crooks *et al.* reported the use of poly(amido-amine) (PAMM), a dendrimer possessing a thiol terminal group, as a stabilising agent for the synthesis of higher order dendritic gold MPCs. Dendritic gold particles containing ferrocene moieties have also been synthesised this way [181]. The dendronised system was shown to possess both the properties of the metallic gold core and dendrimers in sensing for the selective recognition and titration of $H_2PO_4^-$ and $ATP^{2-}$

anions [182]. Other thiolated polymeric stabilisers can be incorporated onto the surface as a means of fusing their properties with those of the metallic particles core.

#### *1.6.3.4. Acid-Base Reactions*

Acid-base reactions of the monolayer protected clusters demonstrate a very simple and efficient application of these entities in molecular and chemical recognition. Boal *et al.* demonstrated the recognition and redox properties of acid-base mono- and multivalent host-guest interactions [183]. Specific recognition by MPCs stabilised with carboxylic acid react with other materials containing a base functionality at their terminus [184]. Layer-by-layer growth of polymers, poly(allyamine hydrochloride) (PAH) and poly(sodium 4-styrene sulfonate) (PSS), has been reported through the acid-base based electrostatic interactions between the ω-functionality and acid-containing organic species [185].

#### *1.6.3.5. Other Reactions of the ω-Functionalities*

The ω-functionalities of the monolayer protected clusters can undergo numerous organic and inorganic reactions as a way of introducing and eliminating specific functionalities and properties. A nucleophillic addition of $C_{60}$ fullerene onto the surface of gold and its subsequent layer-by-layer growth on a planar surface has been reported [186]. Immobilisation of mixed monolayer protected clusters functionalised with carboxylic groups onto the surface of an aminooxy-functionalised gold substrate through the keto group [187].

## 1.7. BIOMOLECULAR FUNCTIONALISATION OF MPCs

Generally, the synthesis of inorganic nanoparticles has been achieved by many different approaches, whereas their subsequent coupling with biomolecules has thus far been limited to a handful of protocols [27-29]. The immobilisation of biomolecules onto the inorganic surfaces has been well documented and achieved in different ways, namely (i) physical or chemical adsorption at a solid surface, (ii) covalent surface binding, and (iii) entrapment within a membrane, polymer or surface matrix and cross-linking between membranes [188]. Each of these approaches has its own advantages and disadvantages,

with the common interest in the preservation of the structural integrity, activity and specificity of the biomolecules.

The general approach in achieving this is to minimise harsh working conditions and also to use the non-essential part of such a protein or enzyme as a binding site. The interactions and effects resulting in the interactions between the nanoparticles and biomolecules have been investigated in detail [189]. Three of the most common methods for immobilisation of macromolecules onto nanosized entities are briefly discussed.

### 1.7.1. Electrostatic (Charge) Attachment

Electrostatic immobilisation of biomolecules on the surface of nanoparticles offers one of the simplest biofunctionalisation methods that can be performed under mild conditions. In the case of nanoparticles stabilised with anionic carboxylic derivative ligands such as lipoic acid, citrate and tartate, positively charged biomolecules can be attached via noncovalent electrostatic interactions [28]. IgG and IgE antibodies have been successfully attached on the citrate-capped Au and Ag nanoparticles. This was achieved by adjusting the pH to above the isoelectric point (pI) of the citrate ligand. A 3D network of nanoparticles was formed through the antibody-antigen cross-links leading to metallic or bimetallic aggregates [190].

The most favourable coupling ratio can be investigated by flocculation assays, through the incremental additions of a strong electrolyte to the solutions of the nanoparticle conjugated with known amounts of the biomolecules [28]. Citrate-capped silver nanoparticles have also been attached with a non-heme iron enzyme through electrostatic adsorption [191]. A Surface-Enhanced Resonance Raman Spectroscopy (SERRS) study indicated that the metalloenzyme retained the biological activity as an adsorbate on the nanoparticles. Cytochrome *c* has also been immobilised onto the citrate-capped Ag nanoparticles, with the surface orientation, activity and the presence of citrate probed with the SERRS. Cytochrome *c* was observed to have two areas of positive charge, upon which the citrate can bind at neutral pH; the lysine rich surface and another surface containing residues of histidine and lysine [192].

Smaller biomolecules such as ascorbic acid have also been electrostatically immobilised on the nanoparticle surface in the study of charge separation properties of

$TiO_2$ nanoparticles [193]. The attachment of BSA onto $Ag_2S$ has also been reported, with the qualitatively reversible protein-nanoparticle assembly and disassembly dependent on the pH, driven by the isomeric conversion of the protein [194]. Other examples of electrostatic immobilisation of biomolecules include the grafting of helical peptides on gold nanoparticles [195], layer-by-layer (LbL) adsorption of charged macromolecules on gold nanoparticles [196], assembly of oligonucleotides on semiconductor quantum dots [197] and temperature-dependent DNA assembly on CdS semiconductor quantum dots [197b].

### 1.7.2. Specific Affinity Immobilisation

Nanoparticles functionalised with ligands that have high specific affinity for certain biomolecules present a facile method for the introduction of biofunctionalities. The streptavidin-biotin system has served as an essential biorecognition tool for protein-ligand interaction with a large affinity of $10^{15}$ $M^{-1}$, the largest noncovalent ligand-protein interaction known [198]. Caswell *et al.* reported an end-to-end assembly of biotin functionalised gold nanorods upon the introduction of streptavidin [199]. Streptavidin has been introduced onto the strongly emitting biotinylated CdS/CdSe core-shell quantum dots, applied in site-specific labelling of F-actin filaments of 3T3 fibroblast cells [200]. Streptavidin has also been introduced into biotin functionalised gold nanoparticles and could be aggregated in a reversible fashion, which confirmed the process to only be specific to the biotin-streptavidin recognition [201].

Nitrilotriacetic acid (NTA), specifically bound to Ni(II) has a high specific affinity for hexahistidine-tagged biomolecules and is commonly used in purification of recombinant His-tagged proteins as a component of immobilised metal-affinity chromatography (IMAC) [202, 203]. From a theoretical perspective, the three NTAs will form three coordination pairs with hexahistideine tag, allowing for a strong NTA-biomolecule complex. Phosphorylated peptides α- and β-casein were successfully immobilised onto Ni-NTA-derivatised $Fe_3O_4$ superparamagnetic nanoparticles, from a complex mixture contained in cow milk, with high specificity [204]. Ancillary studies were also conducted for the immobilisation of protein C192S, showing high trapping performances of the Ni-NTA-functionalised nanoparticles.

Another affinity based biomolecular immobilisation entails an antibody-antigen (lock and key) based attachment [205]. Monoclonal antibodies are generally highly specific in recognition of their target antigens. Sondi *et al.* have demonstrated an antibody-antigen based model for the recognition of dextran-functionalised CdS nanoparticles and antidextran-functionalised CdS quantum dots [206]. Lectin-carbohydrate interactions, in the immobilisation of glycoproteins, have also been exploited in this fashion [207].

### 1.7.3. Covalent Attachment

Another approach for the introduction of biomolecules can be done by the covalent attachment of the target functionalities onto the surface of the nanoparticles. DNA-directed immobilisation of proteins onto 5'-thiol-modified oligonucleotides-functionalised nanoparticles has been demonstrated by Niemeyer *et al.* [208]. Thiolated ssDNA has also been incorporated onto gold nanoparticle surfaces, forming unique particle groupings investigated with agarose gel electrophoresis [209]. Calix[4]arene has also been introduced onto the surface of gold nanoparticles, by the covalent attachment of the thiol group onto the nanoparticle surface [210]. A solid phase reaction using 9-fluorenylmethoxy-carbonyl (Fmoc) as a protecting agent was used in the sequential peptide growth onto the surface of gold nanoparticles [211].

Another oligopeptide, Phe-Ala-Ala-Ala-Ala peptide (FAAAA) was also immobilised via the solid-phase elongation approach on the gold surface, with each residue attachment confirmed by its proton Nuclear Magnetic Resonance ($^1$H-NMR) signal [212]. Cysteine-containing proteins such as serum albumin have also been reported to covalently anchor on the surface of gold nanoparticles via the thiol group of the cysteine residue on the gold surface [213, 214].

## 1.8. INTERFACING NANOPARTICLES WITH CELLS

The size comparability of nanoparticles (1 -100 nm) with those of most biomolecules and subcellular components makes it logical for interfacing of nanotechnology and molecular biology. Nanoparticles have received a lot of attention recently in the development of imaging, targeting, diagnostic and drug delivery and discovery in both *in vivo* and *in vitro*

systems [129-131]. Numerous formulations of these entities have raced into the forefront including, dendrimers, nanocages, micelles, molecular conjugates, liposomes, quantum dots and nanoshells [215]. The design of stealth, multiplexed drug delivery and imaging systems have started to benefit immensely from the unique versatility of nanoparticles in terms of functionalities and impressive optical properties [216]. *In vitro* and *in vivo* labelling using quantum dots have been reported as demonstrated in Figure 1.6 [217, 218].

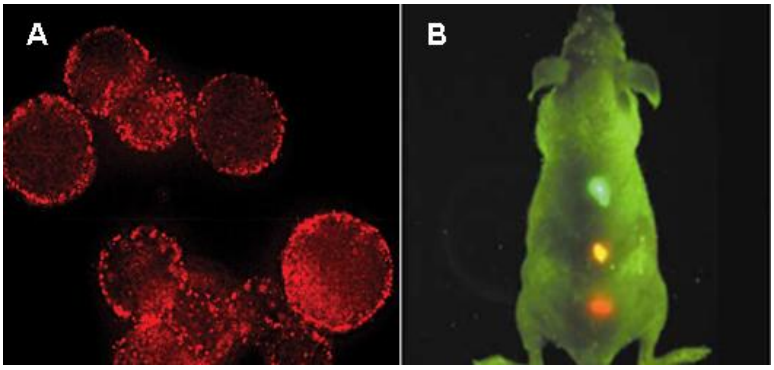


Figure 1.6. *Some examples of nanoparticles in biological applications: (A) in vitro labelling of HEK cells by CdS/ZnS core-shell quantum dots [217] and (B) in vitro imaging using a quantum dot-encoded multicolour bead of a live rat [218].*

Intracellular delivery of cargoes into the nucleus of the cells can be manipulated by conforming the nanoparticle systems to a few guidelines: (i) the nanoparticles must enter the cell via receptor-mediated endocytocytosis (RME), (ii) they must evade the endosomal/lysosomal pathways, (iii) they must possess a nuclear localisation signal (NLS) for successful internalisation and (iv) they must be small enough to cross the nuclear membrane [219]. Attention has also been given to the toxicity effects of these entities inside a living organism. For slightly larger particles ($\geq$ 200 nm), clearance has been reported through opsonisation, with the large size assisting in recognition of the nanoparticles by macrophages [215].

The incorporation of surface functionalities via a PEG polymer renders these nanoparticles highly biocompatible and lowers their cytotoxicity. Noble metal particles, such as gold, are generally non-toxic due to their inert nature; this has also been seen with

their LD50 in toxicity assays, high enough up to 1 mg/mL [220]. The subject of toxicity is still receiving a lot of attention, because of the accumulative effects of nanoparticles are not yet understood.

### 1.8.1. Nanoparticle-Based Targeting Strategies

Poor pharmacokinetics and biopharmaceutical properties of the majority of potential therapeutics have given a need for the development of delivery, biolabeling and diagnostic systems with improved efficacy and efficiency [221]. The non-invasive manner through which preliminary findings have indicated nanoparticles interact with biomolecules on the surface of cells and inside, leaving all biochemical behaviour intact has strengthened the case of a nanoparticle-based therapeutic "tool-box" [222]. A careful understanding of the processes involved in the interactions of nanoparticles with cells leading to their uptake (or rejection) and their subsequent release is of crucial importance.

Nanoparticles offer a rare opportunity to develop multifunctional therapeutics, integrating diagnostics and therapeutic functions in one "tool-box"; simultaneously labelling, monitoring and delivering drug materials, controlling both spatial and temporal release and monitoring [223]. Factors to consider in the use of nanoparticles, especially noble metals, include surface composition, size, shape, structural control and the exciting tunability of the SPR absorption with certain shapes of materials possessing better cross-sectional photon capture abilities compared to conventional dyes, in the optical monitoring of diseases and cell tracking [224].

### 1.8.2. Mechanism of Uptake

Normally the uptake of particulate matter into cells is either by phagocytosis or endocytosis [216]. Phagocytosis is usually involved in the uptake of particles larger than 500 nm, a pathway observed in macrophages, dendritic cells, monosites and basophils [224]. Most inorganic nanoparticles are synthesised to within the 1 – 100 nm range and are thought to be endocytosed into the cell, since the size remains at less than 200 nm regardless of the surface modifications. Endocytosis can either be receptor-mediated or non-receptor-mediated, which either enhances or retards the uptake [225, 226]. The

uptake can be viewed as a result of the contest between the thermodynamic driving force for wrapping, which refers to the amount of free energy needed to drive the nanoparticles into the cell, and the receptor diffusion kinetics, which refers to the kinetics of recruitment of receptors to the binding cell [227].

Targeting of cellular diseases such as cancer in cells by nanoparticle-based systems is subdivided into two pathways: (i) passive and (ii) active targeting. Passive targeting employs pharmacokinetic manipulation and nanoparticle size reduction, whereas active targeting involves specifically targeting areas on a disease cell by surface modifications of the nanoparticles. This targeting seeks to address the current shortfalls such as those observed with conventional drugs that show less than desired accumulations on the target or disease area.

#### *1.8.2.1. Passive Targeting*

This approach occurs via the extravasation of the nanoparticles at the disease site where the fast-growing tumor microvasculature is leaky with defective architecture, which is highly permeable to macromolecules relative to a normal tissue [128]. The dysfunctional lymphatic drainage system of the disease cell allows for the enhanced permeation and retention (EPR) effect [228], as a result of which nanoparticles accumulate at the tumor site. For this mechanism to take place, the size and surface of the nanoparticles should be engineered such that they circumvent uptake by the reticuloendothelial system (RES) [161]. One way of achieving passive targeting is the use of direct local delivery of the agents into the affected cell.

This method is advantageous since it preserves the drug from systemic circulation but is also very invasive since it involves injections and surgical procedures. The size of open interendothelial gap junctions and trans-endothelial channels determines the extent of the nanoparticle extravasation, with a cutoff of between 400-600 nm reported elsewhere [229]. One of the biggest challenges for passive targeting is the inability to accumulate large enough amounts of the nanoparticles on the tumor cells resulting in low therapeutic efficacy and drawing unwanted systemic adverse effects [230]. Extended circulation time is also required for passive targeting to allow the drug loaded nanoparticles to pass the disease site repeatedly to deposit effectively.

#### *1.8.2.2. Active Targeting*

Localised diseases such as cancer and inflammation overexpress some epitopes or receptors which can be used as specific targets [128]. The use of nanoparticles involves the conjugation of the targeting molecules on the surface that recognises and attaches to specific receptors that are unique to a particular disease cell. This targeting approach is based on interactions such as lectin-carbohydrate, ligand-receptor, and antibody-antigen. Active targeting, which is ligand dependant, is particularly invaluable to therapeutics that are not taken up easily by cells. It has also been demonstrated that active targeting improves the distribution of nanomedicines within the tumor interstitium [231]. A factor to be considered when selecting the targeting ligand is its immunogenicity. If, for example, antibodies expose their constant regions on the liposomal surface, they become more susceptible to Fc-receptor-mediated phagocytosis by the mononuclear phagocytic system (MPS) [232].

This method is particularly useful for primary tumors that have not yet metastasised. One of the major issues in chemotherapy is multiple drug resistance (MDR), which often starts from the overexpression of the plasma membrane P-glycoprotein (Pgp) in cancer cells [233]. Pgp acts as an efflux pump to extrude positively charged xenobiotics, which include many anticancer drugs, out of the cells. Glycoproteins are known to be unable to remove polymer-drug conjugates that enter the cell via endocytosis, and this renders the active targeting mechanism to be an alternative route to overcoming MDR [234].

### 1.8.3. Fate of Nanoparticles in the Body

The use of modified nanoparticles for drug delivery systems maximises the localisation of the delivery agents and their subsequent accumulation only to the target site [235]. The EPR effect (for passive targeting) and the surface derivatisation (for active targeting) are important in the specificity of the delivery systems [128, 230]. Nanoparticle-based delivery systems are a good method for the circumvention of adverse effects due to the migration of the nanoparticles to other sensitive parts of the body [236]. The exact mechanism and pathways of how the body rids itself of the nanoparticles is still subject

of intense investigation, with the liver most likely the destination of the spent nanoparticles; with their design such that they pass freely in other organs but can be retained in the liver and spleen [215].

## 1.9. CHARACTERISATION TECHNIQUES

### 1.9.1. UV-vis Spectroscopy

UV-vis spectroscopy deals with electron transitions due to interactions with electromagnetic light photons. Optical properties of semiconductor nanoparticles and those of metal particles whose band gap or surface plasmon resonance absorption are in the visible range have been studied intensively by UV-vis spectroscopy. Optical properties of semiconductor nanoparticles are dependent on their sizes, with blue shifts in band gap energy observed with the decrease in particle sizes, allowing for the determination of particle sizes from UV-vis measurements [26, 237]. The manipulation of optical properties by the movement of electrons and holes in materials is especially important in the development of low dimension optonics and electronics [238]. For the metal nanoparticles, the optical properties can be correlated with the particles size; for larger particle sizes the Mie theory can explain their optical properties [148]. For smaller colloidal metal particles, the shape, size and interparticle distances dictate the optical absorption and hence the state of aggregation in solution [239].

### 1.9.2. Transmission Electron Microscopy (TEM)

The TEM uses a beam of high energy electrons that are focussed and transmitted through a thin sample allowing measurements of parameters including nanoparticle core dimensions such as size, morphology, crystallography, elemental composition, state of aggregation and particle size distribution [39, 54, 240]. With the development of the High Resolution TEM (HRTEM), atomic-resolution lattice images of nanoparticles can be obtained from this technique, with spatial resolution of 1 nm or better. The TEM can be focused on a single nanoparticle, thus allowing for the identification and subsequent quantification of its chemical and electronic structure, which governs its unique physical and chemical properties. The TEM can give both electron microscope images and also the diffraction pattern for a specific region on a sample by adjusting the magnetic lenses that control the electron beam strength passing through the sample [241].

The crystal structure can be obtained when the images are formed due to differences in phase of electron waves scattered through a thin specimen. Due to the wealth of information and simplicity of operation, the TEM and HRTEM to an extent, has become the first stop in the elucidation of the properties of nanosized materials. Semiconductors, metals and many other macro-/nanosized materials have been elucidated using TEM [27, 30, 34, 242].

### 1.9.3. Agarose Gel Electrophoresis

Agarose gel electrophoresis (AGE) is a relatively simple and straightforward technique to perform, yet it possesses enormous resolving power and is routinely employed in molecular biology for the separation of biomolecules such as DNA, RNA and proteins. AGE separates molecules based on charge, size, conformation and shape, as they migrate in an electric field. Electrophoresis is conducted by loading the samples into wells on a thin slab of agarose, a polysaccharide derivative of agar, immersed in a relevant buffer inside the electrophoresis setup. A direct power supply is connected and current is applied. Positively charged molecules migrate towards the cathode and negatively charged molecules migrate to the anode; however nucleic acids possess a negative charge owing to their phosphate backbone and therefore migrate towards the anode, with size and conformation the only variables.

The gel contains sieve-like microscopic pores and smaller molecules migrate faster than larger ones. Gerion *et al.* demonstrated the use of agarose gel electrophoresis for the investigation of pH- and salt-stability of silica-coated CdSe/ZnS quantum dots [209]. Isolation of gold nanoparticle-DNA conjugate probes has been achieved using agarose gel electrophoresis [209b]. Surface events on monolayers of gold nanoparticles possessing biomolecular binding moieties have been monitored using agarose gel electrophoresis technique [243].

### 1.9.4. Flow Cytometry

Flow cytometry is a special tool for the quantification of cells, achieved by either using the physical or chemical properties of the cells or any other biological reagent that is internalised into the cells. Processes such as apoptosis, necrosis and cell division can be

monitored using flow cytometry measurements. Flow cytometry has become an indispensable tool in analyses of haematological malignancies in clinical diagnosis [244]. Recent applications have included disease monitoring and the evaluation of tumor response to therapeutics [245]. This technique can provide immunophenotypic data and cellular morphology information. Cytometry-based detection techniques can provide an analytical sensitivity of one disease cell in $10^4$ to $10^{16}$ healthy normal cells. A Fluorescence-Activated Cell Sorter (FACS) spectrophotometer is a specialised instrumentation based on the flow cytometry principles.

FACS is used for the sorting and quantification of cells based on their fluorescence absorbance from the internalised fluorescence dye; translated according to the granularity and size of the cells. Compromised or cells undergoing apoptosis are known to shrink and can therefore be distinguished from the live cells. Mitochondrial events during apoptosis have been reported using FACS [246]. FACS-based cell proliferation assays have been conducted on cancer cells treated with gold nanoparticles [124b]. Cell selective viability as a response to the treatment by gold nanoparticles has been probed using the FACS technique [247].

## 1.10. THESIS LAYOUT

The thesis is divided into four chapters; of which a brief synopsis is outlined.

### *Chapter 1: Introduction*

As described in the preceding pages, chapter one delivers the introduction of a variety of aspects in nanomaterials and biomaterials and biological implications of these nanomaterials. A brief review on the history, synthesis techniques, properties, conversion to monolayer protected clusters (MPCs), general applications and characterisation strtegies for optical and structural properties.

### *Chapter 2: Synthesis of Colloidal Gold Nanoparticles and MPCs*

In this chapter, aqueous and nonaqueous synthetic protocols are employed to synthesise nanoparticles of average sizes varying from 4-119 nm. Thiolated ligands comprising a multitude of functional groups (-OH, $-NH_2$, -COOH), as handles for further

immobilisation of specific moieties, and molecules of biological significance such as L-cysteine and L-glutathione were used as capping agents. Nanoparticle size variations as a function of gold:ligand ratio and differing alkanethiolate chain lengths was investigated.

***Chapter 3: Synthesis of PEGylated Gold MPCs and Biomolecular Functionalisation***

Heterobifunctional thioalkylated PEG ligands as capping agents for gold MPCs are reported in this chapter. Further immobilisations of biomolecules on the surfaces of the MPCs using standard protocols are presented.

***Chapter 4: Cytotoxicicity Studies of Colloidal Gold Nanoparticles, MPCs and Bioconjugates***

Studies on the cytotoxicicity of colloidal gold nanoparticles, MPCs and bioconjugates will be presented. Effects of surface functionalities, size and dose are described.

***Chapter 5: Conclusions and Future Outlook***

Conclusions and further outlook are presented in this final chapter.

## 1.11. REFERENCES

1. Kauffman G.B., *Gold Bull.*, 1985, **18**, 31.
2. Kauffman G.B., *Gold Bull.*, 1985, **18**, 69.
3. Higby G.J., *Gold Bull*., 1982, **15**, 130.
4. Freestone I., Meeks N., Sax M. and Higgitt C., *Gold Bull*., 2007, **40**, 270.
5. Hauser E.A., *J. Chem. Ed*., 1952, 456.
6. Multhanf R., *ISIS*, 1954, **45**, 364.
7. Corbett J., *Gold Bull*., 1976, **9**(4), 144.
8. Hunt L.B., *Gold Bull*., 1976, **9**(4), 134.
9. Shaw C.F., *Chem. Rev*., 1999, **99**, 2589.
10. Henglein A., *Top. Curr. Chem.*, 1988, **143**, 113.
11. Henglein A., *Chem. Rev.*, 1989, **89**, 1861.
12. Steigerwald M.L. and Brus L.E., *Acc. Chem. Res.*, 1990, **23**, 183.
13. Fendler J.H., *Chem. Rev.*, 1987, **87**, 877.

14. Goldstein A.N., Echer C.M. and A.P. Alivisatos, *Science*, 1992, **256**, 1425.
15. Wang Y., *Acc. Chem. Res.*, 1991, **24**, 133.
16. Kamat P.V., *Chem. Rev.*, 1993, **93**, 267.
17. Thomas J.K., *Chem. Rev.*, 1993, **93**, 301.
18. Henglein A., *J. Phys. Chem.*, 1993, **97**, 5457.
19. Spanhel L., Haase M., Weller H. and Henglein A., *J. Am. Chem. Soc.*, **109**, 5649.
20. Haase M., Weller H. and Henglein A., *J. Phys. Chem.*, 1988, **92**, 4706.
21. Duong D., Borgarello E. and Gratzel M., *J. Am. Chem. Soc.*, 1981, **103**, 4685.
22. Alivisatos A.P., *Science*, 1996, **271**, 933.
23. Colvin V.L., Schlamp M.C. and Alivisatos A.P., *Nature*, 1994, **370**, 354.
24. Brus L.E., *J. Chem. Phys*., 1984, **80**, 4403.
25. Weller H., *Angew. Chem. Int. Ed.*, 1993, **32**, 41.
26. Alivisatos A.P., *J. Phys. Chem*., 1996, **100**, 13226.
27. Daniel C.-M. and Astruc D., *Chem. Rev*., 2004, **104**, 293.
28. Niemeyer C.M., *Angew. Chem. Int. Ed*., 2001, **40**, 4128.
29. Katz E. and Willner I., *Angew. Chem. Int. Ed*., 2004, **43**, 6042.
30. Brust M and Kiely C.J., *Colloids Surf. A*, 2002, **202**, 175.
31. Kumar R., Biebuyck H.A. and Whitesides G.M., *Langmuir*, 1994, **10**, 1498.
32. Xia Y. and Whitesides G.M., *Annu. Rev. Mater. Scie*., 1998, **28**, 153.
33. Kumar A., Abbott N.A., Kin E., Biebuyck H.A. and Whitesides G.M., *Acc. Chem. Res*., 1995, **28**, 219.
34. Cushing B.L., Kolesnichenko V.L. and O'Connor C.J., *Chem. Rev*., 2004, **104**, 3893.
35. Watzky M.A. and Finke R.G., *J. Am. Chem. Soc*., 1997, **119**, 10382.
36. Teranishi T. and Miyake M., *Chem. Mater*., 1998, **10**, 594.
37. Aiken III J.D. and Finke R.G., *J. Mol. Cat. A: Chem*., 1999, **145**, 1.
38. Faraday M., *Philos. Trans. Royal Soc. London*, 1857, **147**, 145.
39. Turkevitch J., Stevenson P.C. and Hillier J., *Discuss. Faraday Soc*., 1951, **11**, 55.
40. Turkevitch J., Gold Bull., 1985, **18**(3), 86.
41. Chow M.K. and Zukoski E.F., *J. Colloid Interface Sci.*, 1994, **165**, 97.
42. Peng B.-K., Elin H.I., Chong J.-X., Ji W., Trout B.L. and Lee J.-Y., *J. Phys. Chem. C*, 2007, **111**, 6281.

43. Murray C.B., Norris D.J. and Bawendi M.G., *J. Am. Chem. Soc*., 1993, **115**, 8706.
44. Frens G., *Nature Phys. Sci.*, 1973, **241**, 20.
45. Liz-Marzan L.M., *Mater. Today*, 2004, **7**(2), 26.
46. Patungwasa W. and Hodak J.H., *Mater. Chem. Phys*., 2008, **108**, 45.
47. Henglein A. and Giersig M., *J. Phys. Chem B*, 1999, **103**, 9533.
48. Lee P.C. and Meisel D., *J. Phys. Chem*., 1982, **86**, 3391.
49. Turkevitch J, Miner R.S. and Babenkova L., *J. Phys. Chem*., 1986, **90**, 4765.
50. Furlong D.N., Launikonis A., Sasse W.H.F. and Sanders J.V., *J. Chem. Soc. Faraday Trans*., 1984, **80**, 571.
51. Turkevitch J. and Kim G., *Science*, 1970, **169**, 873.
52. Kumar S., Gandhi S.K. and Kumar R., *J. Am. Chem. Soc*., 2007, **46**(10), 2007.
53. Giersig M and Mulvaney P., *Langmuir*, 1993, **9**, 3408.
54. Brust M., Walker M., Bethell D., Schiffrin J and Whyman R., *Chem. Commun*., 1994, 801.
55. Pasquato L., Pengo P. and Scrimin P., *J. Mater. Chem*., 2004, **14**, 3481.
56. Brust M., Fink J., Bethell D., Schiffrin J and Kiely C., *Chem. Commun*., 1995, 1655.
57. a) Weisbecker C.S., Merritt M.V and Whitesides G.M., *Langmuir*, 1996, **12**, 3763; b) Potter L.A.J. Ji D., Wescott S.L., Groupe M., Czernuszewicz R.S., Halas N.J. and Lee T.R. *Langmuir*, 1998, **14**, 7378; c) Thomas P.J., Sarawan P., Kulkarni G.U. and Rao C.N.R., *Praman-J. Phys. Chem*., 2002, **58**, 371; d) Green M. and O'Brien P., *Chem. Commun*., 2000, 183; e) Prasad B.L.V., Stoeva S.I., Sorensen C.M. and Klabunde K.J., *Chem. Mater*., 2003, **15**, 935.
58. a) Hostetler M.J., Green S.M., Stokes S.A. and Murray R.W., *J. Am. Chem. Soc*., 1996, **118**, 4212; Wuelfing W.P., Gross S.M., Miles D.T. and Murray R.W., *J. Am. Chem. Soc*., 1998, **120**, 12696; b) Hostetler M.J., Wingate J.E., Zhong C.-J., Harris J.E., Vachet R.W., Clark M.R., Londono J.D., Green S.J., Stokes J.J., Wignall G.D., Glish G.L. Porter M.D., Evans N.D. and Murray R.W., *Langmuir*, 1998, 119, 9175; c) Templeton A.C., Hostetler M.J., Kraft C.T. and Murray R.W., *Langmuir*, 1999, **15**, 3782.
59. Templeton A.C., Wuelfing W.P. and Murray R.W., *Acc. Chem. Res*., 2000, **33**, 27.

60. Yee C., Scotti M., Ulman A., White H., Rafailovich M. and Sokolov J., *Langmuir*, 1999, **15**, 4314.
61. Quiros I., Yamada M., Kubo K., Mizutani J., Kurihara M and Mishihara H., *Langmuir*, 2002, **18**, 1413.
62. Chen S. and Sommers J.M., *J. Phys. Chem*., 2001, **105**, 8816.
63. a) Fievet R., Lagier J.P., Blien B., Boaudoin B. and Figlarz M., *J. Solid State Ionics*, 1989, **32**, 198; b) Ducamp-Sangsuesa C., Herrera-Urbina R. and Figlarz M., J. Solid State Chem., 1992, **100**, 272.
64. Bonet F., Delmas V., Grugeon S., Herrera-Urbina R., Silvert P.-Y. and Tekaia-Elhsissen K., *Nano. Struct. Mater*., 1999, **8**(11), 1277.
65. Silvert P.-Y., Herrera-Urbina R., Duvauchelle N., Vijayakrishna V. and Tekaia-Elhsissen K., *J. Mater. Chem*., 1996, **6**(4), 573.
66. Seshadri R. and Rao C.N.R., *Mater. Res. Bull*., 1994, **29**, 795.
67. Okitsu, K.; Mizukoshi Y., Bandow H., Maeda Y.,Yamamoto T. and Nagata Y., *Ultrason. Sonochem*., 1996, **3**, S249.
68. Fujimoto T., Terauchi S.-Ya, Mehara H., Kojima I. and Henderson W., *Chem. Mater*., 2001, **13**, 1057.
69. Flint E. B. and Suslick K., *Science*, 1991, **253**, 1397.
70. Yeung S. A., Hobson R., Biggs S. and Grieser F., *Chem. Commun*., 1993, 378.
71. Grieser F., Hobson R., Sostaric J. and Mulvaney P., *Ultrasonics*, 1996, **34**, 547.
72. Pol V. G., Srivastava D., N., Palckik, O., Palchik, V., Slifkin M. A., Weiss A. M. and Gedanken A., *Langmuir*, 2002, **18**, 3352.
73. Nagata Y., Watanabe, Y., Fujita S., Dohmaru T. and Taniguchi S., *Chem. Commun*., 1992, 1620,
74. Mastai Y., Polsky R., Koltypin Y., Gedanken A. and Hodes G., *J. Am. Chem. Soc*., 1999, **121**, 10047,
75. Dabbousi B.O., Murray C.B., Rubner M.F. and Bawendi M.G., *Chem. Mater*., 1994, **6**, 216,
76. Fendler J.H., *Chem. Rev.,* 1987, **87**, 877.
77. Ozin G.A., Kaperman A. and Stein A., *Angew. Chem. Int. Ed.*, 1989, **29**, 359.

78. van der Zande B.M.I., Bohmer M.R., Fokkink L.G.J. and Schonenbeger C, *J. Phys. Chem. B*, 1997, **101**, 852.
79. Foss C.A., Hornyak G.L., Tierney M.J. and Martin C.R., *J. Phys. Chem*., 1992, **96**, 9001.
80. Mohamed M.B., Ismael K.Z., Link S. and El-Sayed M.A., 1998, *J. Phys. Chem. B*, 1998, **102**, 9370.
81. Lisiecki J.I., Billoudet F. and Pileni M.P., *J. Phys. Chem*., 1996, **100**, 4160.
82. Taleb A., Petit C., and Pileni M.P., *Chem. Mater*., 1997, **9**, 950.
83. Li F., Li G.-Z, Wang H.-Q. and Xue A.J., *Colloids Surf. A*, 1997, **127**, 89.
84. Chang G.X., Shen F., Yang L.F., Ma L.F., Tang Y., Yao K.J. and Sun P.C., *Mater. Chem. Phys*., 1998, **56**, 97.
85. Lisiecki I. and Pileni M.P., J. Am. Chem. Soc., 1993, **115**, 3887; Petit C., Taleb A. and Pileni M.P., *J. Phys. Chem. B*, 1999, **103**, 1805.
86. Boutonnet M., Kizhing J., Stenius P. and Maire G., *Colloids Surf*., 1982, **5**, 209
87. Chen D.-H. and Wu S.-H., *Chem. Mater*., 2000, **12**, 1354.
88. Chen J.P., Lee K.M., Sorensen C.M., Klabunde K.J. and Hadjipanayis G.C., *J. Appl. Phys.*, 1994, **75**, 5876.
89. Hou X.H. and Choy K.L., *Chem. Vap. Depodition*, 2006, **12**, 583.
90. McCurdy R.J., *Thin Solid Films*, 1999, **351**, 66.
91. Palgrave R.G. and Parkin I.P., *Gold Bull*, 2008, **41**, 66.
92. a) Xie S.S., Li W., Pan Z., Chang B.H., Sun L., *Mater Sci. Eng*., 2000, **A286**, 11; b) Li W.Z., Xie S.S., Qian L.X., Chang B.H., Zou B.S., Zhou W.Y., *Science*, 1996, **274**, 1701.
93. Cansell F., Chevalier B., Demourgues A., Etourneau J., Even C., Garrabos Y., Pessey, V., Petit S., Tressaud A. and Weill F., *J. Mater. Chem.*, 1999, **9**, 67.
94. Gautam U. K., Ghosh M., Rajamathi M. and Seshadri R., *Pure Appl. Chem*., 2002, **74**, 1643.
95. Demazeau G. J., *Mater. Chem*., 1999, **9**, 15.
96. Cheng H., Ma J., Zhao Z. and Qi L., *Chem. Mater*., 1995, **7**, 663.
97. Inoue M., Kimura M. and Inui T., *Chem. Commun*., 1999, 957.

98. Thimmaiah S., Rajamathi M., Singh N., Bera P., Meldrum F., Chandrasekhar N. and Seshadri R., *J. Mater. Chem*., 2001, **11**, 3215.

99. Peng Q., Dong Y., Deng Z., Sun X., Li Y., *Inorg. Chem*., 2001, **40**, 3840.

100. Gautam U. K., Rajamathi M., Meldrum F., Morgan P. and Seshadri R., *Chem. Commun*., 2001, 629.

101. Chen X. and Fan R., *Chem. Mater*., 2001, **13**, 802.

102. a) Newalkar B. L. and Komarneni S., *Chem. Mater*., 2001, **13**, 4573; b) Newalkar B. L., Olanrewaju J. and Komarneni S., *J. Phys. Chem. B*, 2001, **105**, 8356.

103. a) Mukharjee P., Ahmad A., Mandal D., Senapati S., Sainkar S.R., Khan M.I., Parishcha R., Ajaykumar P.V., Alam M., Kumar R and Sastry M., *Nano Lett*., 2001, **1**(10), 515; b) Mukharjee P., Ahmad A., Mandal D., Senapati S., Sainkar S.R., Khan M.I., Ramani R., Parischa R., Ajayakumar P.V., Alam M., Satry M. and Kumar R., *Angew Chem. Intl. Ed.*, 2001, **40**, 3585; c) Ahmad A., Priyabrata M., Mandal D., Senapati S., Khan I., Kumar R. and Sastry M., *J. Am. Chem. Soc*., 2002, **124**, 12108.

104. Lovley D.R., Stolz J.F., Nord G.L. and Phillips E.J.P., *Nature*, 1987, **330**, 252.

105. Oliver S., Kupermann A., Coombs N., Lough A. and Ozin G.A., *Nature*, 1995, **378**, 47.

106. Pum D. and Sleytr U.B., *Trends Biotechnol*., 1999, **17**, 8.

107. Dameron C.T., Reese R.N., Mehra R.K. and Kortan A.R., Carroll P.J., Steigerwald M.L., Brus L.E. and Winge D.R., *Nature*, 1989, **338**, 596.

108. Klause-Joeger T., Joerger R. and Olsson E. C.-G, *Trends Biotechnol*., 2001, **19**, 15.

109. Labrenz M., Druschel G.K., Thomsen-Elbert T., Gilbert B., Welch S.A., Kemmer K.M., Logan G.A., Summons R.E., De Stasio G., Bond P.L., Lai B., Kelly S.D. and Banfield J.F., *Science*, 2000, **290**, 1744.

110. Holmes J.D., Smith P.R., Evans-Gowing R., Richardson D.J., Russell D.A. and Sodeau J.R., *Arch. Microbiol*., 1995, **163**, 143.

111. Nair B. and Pradeep T., *Cryst. Growth Des*., 2002, **2**, 293.

112. LaMer V.K. and Dinegar R.H., *J. Am. Chem. Soc*., 1950, 72, 4847; LaMer V.K., *Ind. Eng. Chem*., 1951, **19**, 482.

113. a) Matijevic E., *Chem. Mater*., 1993, 5, 412; b) Kerker M., Daby E., Cohen G.L., Krahtovil J.P. and Matijevic E., *J. Phys. Chem*., 1963, **67**, 2105.

114. Murray C.B., Norris D.J. and Bawendi M.G., *J. Am. Chem. Soc*., 1993, **115**, 8706.

115. Ahmadi T.S., Wang Z.L., Henglein A. and El-Sayed M.A., *Chem. Mater*., 1996, **8**, 1161.

116. Brown R., Phil. Mag., 1828, 4, 161; Nelson E., *Dynamical Theories of Brownian Motion*, Princeton University Press, Princeton, 2nd Ed, 1967.

117. Bhattarchee S., Elimelech M. and Borkovec M., *Croat. Chem. Acta*, 1998, **71**(4), 883.

118. a) Hasselink F.T., Vrij A. and Overbeek J.T.G, *J. Phys. Chem*., 1971, **75**; b) Meier D.J., *J. Phys. Chem.*, 1967, **71**, 1861.

119. Schmid G., *Endeavour, New Series*, 1990, **14**, 172.

120. Aiken J.D. III, Lin Y. and Finke R.G., *J. Mol. Cat. A: Chem*., 1996, **114**, 29.

121. a) Mirkin C.A., Letsinger R.L., Mucic R.C. and Storhoff J.J., *Nature*, 1996, **382**, 607; b) Rosi N.L. and Mirkin C.A., *Chem.Rev*., 2005, **105**, 1547.

122. Tansil N.C. and Gao Z., *Nanotoday*, 2006, **1**(1), 28.

123. Jain P.K., El-Sayed I.H. and El-Sayed M., *Nanotoday*, 2007, **2**(1), 18.

124. a) Mukherjee P., Bhattacharya R., Wang P., Basu S., Nagy J.A., Atala A., Mukhopadhyay D. and Soker S., *Clin. Cancer Res*., 2005, **11**(9), 3530; b) Gannon C.J., Patra C.J., Bhattacharya R., Mukherjee P. and Curley S.A., *J. Nanobiotech*., 2008, **6**(2), doi:10.1186/1477-3155-6-2..

125. Sengupta S. and Sasisekharan R., *Brit. J. Cancer*, 2007, **96**, 1315

126. Paciotti G.F., Kingston D.G.I. and Tamarkin L., *Drug Del. Res*., 2006, **67**, 47.

127. Harisinghani M.G., Barentsz J., Hahn P.F., Deserno W.M., Tabatabaei S., van de Kaa C.H., de la Rosette J. and Weissleder R., *N. Engl. J. Med.*, 2003, **348**, 2491.

128. Koo O.M., Rubinstein I. and Onyuksel H., *Nanomedicine: Nanotechnology, Biology, and Medicine*, 2005, **1**, 193.

129. Dobrovolskaa M.A. and McNeil S.E., *Nature Nanotechnology*, 2007, **2**, 469.

130. Azzazy H.M.E., Mansour M.M.H. and Kazmierczak S.C., *Clin. Chem*., 2006, **52**(7), 1238.

131. Labhasetwar V., *Curr. Opin. Biotech*., 2005, **16**, 674.

132. Hvolbaek B., Jahnssens T.V.W., Clausen B.S., Falsig H., Christensen C.H. and Norskovi J.K., *Nanotoday*, 2007, **2**(4), 14.

133. Schmid G., *Chem. Rev*., 1992, **92**, 1709.

134. Corti C.W., Holliday R.J. and Thompson D.T., *Gold Bull*., 2002, **35**, 111.

135. Martens P.G.N., Vankelecom I.F.J., Jacobs P.A. and De Vos D.E., *Gold Bull*., 2005, **38**(4), 157.

136. Grisel R., Weststrate K.-J., Gluhoi A. and Nieuwenhuys B.E., *Gold Bull*., 2002, **35**(2), 39.

137. Haglund R.F. Jr, *Mater. Sci. Eng. A*, 1998, **253**, 275.

138. Cui Y. and Lieber C.M., *Science*, 2001, **291**, 851.

139. Zhong Z., Wang D., Cui Y., Bockrath M.W. and Lieber C.M., *Science*, 2003, **302**, 1377.

140. Andres R.P., Bein T., Dorogi M., Feng S., Henderson J.I., Kubiak C.P., Mahoney W., Osifchin R.G. and Reifenberger R., *Science*, 1996, **272**, 1323.

141. a) Eustis S and M. El-Sayed M., *Chem. Soc. Rev.*, 2006, **35**, 209; b) Link S. and el-Sayed M., *Annu. Rev. Phys. Chem.*, 2003, **54**, 331.

142. Liz-Marzan L.M., Langmuir, 2006, **22**, 32.

143. Papavassiliou G.C., *Prog. Solid State Chem.*, 1979, **12**, 185.

144. Mulvaney P., *Langmuir*, 1996, **12**, 788.

145. Nie S. and Emory S.R., *Science*, 1997, **275**, 1102.

146. a) Adams A., Rendell R.W., West W.P., Broida H.P., Hansma P.K. and Metiu H., *Phys. Rev.* B, 1980, **21**, 5565; b) Adams A., Rendell W.R., Garnett R.W., Hansma P.K. and Metiu H., *Opt. Commun.*, 1980, **34**, 417; c) Adams A., Moreland J. and Hansma P.K., *Surf. Sci.*, 1981, **111**, 351; d) Metiu H. and Das P., *Annu. Rev. Phys. Chem.*, 1984, **35**, 507; e) Metiu H., *Progr. Surf. Sci.*, 1984, **17**, 153.

147. Creighton J.A. and Eadon D.G., *J. Chem. Soc. Faraday Trans.*, 1991, **87**, 3881.

148. Mishchenko M.I., Travis L.D. and Lacis A.A., *Scattering, Absorption and Emission of Light by Small Particles*, Cambridge University Press, Cambridge, 2002.

149. Aden A.L. and Kerker M., *J. Appl. Phys*., 1951, **22**, 1242.

150. a) Alvarez M.M., Khoury J.T., Schaaff T.G., Shafigullin M.N., Vezmar I. and Whetten R.L., *J. Phys. Chem. B*, 1997, **101**, 3706; b) Logunov S.L., Ahmdi T.S., El-Sayed M.A., Khoury J.T. and Whetten R.L., *J. Phys. Chem. B*, 1997, **101**, 3713

151. a) Prime K.L. and Whitesides G.M., *J. Am. Chem. Soc*., 1993, **115**, 10714; b) Roberts C., Chen S., Mirksch M., Martichonok V., Ingber D.E. and Whitesides G.M., *J. Am. Chem. Soc*., 1998, **120**, 6548.

152. Wuelfing W.P., Gross S.M., Miles D.T. and Murray R.W., *J. Am. Chem. Soc*., 1998, **120**, 12696.

153. Otsuka H., Akiyama Y., Nagasaki Y. and Kataoka K., *J. Am. Chem. Soc*., 2001, **123**, 8226.

154. Foos E.E., Snow A.W., Twigg M.E. and Ancona M.G., *Chem. Mater*., 2002, **14**, 2401.

155. a) Hong R., Fischer N.O., Emrick T. and Rotello V.M., *Chem. Mater*., 2005, **17**, 4617; b) Shenhar R. and Rotello V.M, *Acc. Chem. Res*., 2003, **36**, 549

156. Qiu, B., Stefanos S., Ma. J., Lalloo A., Perry B.A., Lebowitz M.J., Sinko P.J. and Stein S., *Biomaterials*, 2003, **24**, 11.

157. Annunziata O., Asherie N., Lomakin A., Pande J., Ogun O. and Benedek G.B., *Proc. Natl. Acad. Sci. U.S.A*., 2002, **99**, 14165.

158. Kinstler O., Molineux G., Treuheit M., Ladd D. and Gegg C., *Adv. Drug Deliv. Rev*., 2002, **54**, 477.

159. Harris J.M., Martin N.E. and Modi M., Clin. *Pharmacokinet*., 2001, **40**, 539.

160. Yamaoka T., Tabata Y. and Ikada Y., J. *Pharm. Sci*., 1994, **83**, 601.

161. Gref R., Minamitake Y., Peracchia M.T., Trubetskoy V., Torchilin V. and Langer R., *Science*, 1994, **263**, 1600.

162. Lasic D.D., Martin F.J., Gabizon A. and Huang S.A., *Biochim. Phys. Acta*, 1991, **187**, 1070.

163. Muller R.H., Wallis K.H., Troster S.D. and Kreuter J., *J. Control. Release*, 1992, **20**, 237.

164. Zheng M., Davidson F. and Xuang X., *J. Am. Chem. Soc*., 2003, **125**, 7790.

165. Yamamoto Y., Nakao W., Atago Y., Ito K. and Yagci Y., *Eur. Polym. J*., 2003, **39**, 545.

166. Haselgrubler T., Amerstorfer A., Schindler H. and Gruber H.J., *Bioconjugate Chem*., 1995, **6**, 242.

167. Roberts M.J., Bentley M.D. and Harris J.J., *Adv. Drug Deliv. Rev*., 2002, **54**, 459.

168. Yuan M. and Deng X., *Eur. Polym. J*., 2001, **37**, 1907.

169. Bonnans-Plaisance C., Jean M. and Lux F., *Eur. Polym. J*., 2003, **39**, 863.

170. Kim S.W. and Sagara K., *J. Control. Rel*., 2002, **79**, 271.

171. Zalupsky S., *Adv. Drug Deliv. Rev*., 1995, **16**, 157.

172. Shon Y.-S. and Choo H., *C.R. Chimie*, 2003, **6**, 1009.

173. Song Y., Huang T. and Murray R.W., *J. Am. Chem. Soc*., 2003, **125**, 11694.

174. Kassam A., Bremner G., Clark B., Ulibarri G. and Lennox R.B., *J. Am. Chem. Soc*., 2006, **128**, 3476.

175. Yamada M., Tadera T., Kubo H. and Nishihara H., *Langmuir*, 2001, 2363.

176. Brousseau L.C. III, Zhao Q., Schultz D.A. and Feldheim D.L., *J. Am. Chem. Soc*., 1998, **120**, 7645.

177. Labande A., Ruiz J. and Astruc D., *J. Am. Chem. Soc*., 2002, 1782.

178. Banerjee S. and Wong S.S., *Nano Lett*., 2002, **2**(3), 195.

179. Hirsch R., Katz E. and Willner I., *J. Am. Chem. Soc*., 2000, **122**, 12053.

180. Templeton A.C., Hostetler M.J., Warmoth E.K., Chen S., Hartshorn C.M., Krishnamurthy V.M., Forbes M.D.E. and Murray R.W., *J. Am. Chem. Soc*., 1998, **120**, 4845.

181. Chechik V. and Crooks R.M., *Langmuir*, 1999, **15**, 6364.

182. Daniel M.-C., Ruiz J., Nlate S., Blais J.-C. and Asruc D., *J. Am. Chem. Soc*., 2003, **125**, 2617.

183. Boal A.K. and Rotello V.M., *J. Am. Chem. Soc*., 2002, **124**, 5019.

184. Fullam S., Rao S.N. and Fitzmaurice D., *J. Phys. Chem. B*, 2000, **104**, 6164.

185. Hicks J.F., Seok-Shon Y. and Murray R.W., *Langmuir*, 2002, **18**, 2288.

186. Shon Y.-S. and Choo H., *Chem. Commun*., 2002, 2560.

187. Chan E.W.L. and Yu L., *Langmuir*, 2002, **18**, 311.

188. Collings A.F. and Caruso F., *Rep. Prog. Phys*., 1997, **60**, 1397.

189. a) You C.-C., Chomposor A. and Rotello V.M., *Nanotoday*, 2007, **2**(3), 34; b) You C.-C., De M. and Rotello V.M., *Curr. Opin. Chem. Biol*., 2005, **9**, 639.

190. Shenton W., Davis S.A. and Mann S., *Adv. Mater*., 1999, **11**(6), 449.

191. Broderick J.B., Natan M.J., O'Halloran and Van Duyne R.P., *Biochemistry*, 1993, **32**, 13771.

192. Macdonald I.D.G. and Smith W.E., *Langmuir*, 1996, **12**, 706.

193. Rajh T., Nedeljovic J.M., Chen L.X., Poliektov O. and Thuanauer M.C., *J. Phys. Chem. B*, 1999, **103**, 3315.

194. Meziani M.J. and Sun Y.-P., *J. Am. Chem. Soc*., 2003, **125**, 8015.

195. Pengo P., Broxterman Q.B., Kaptein B., Pasquato L. and Scrimin P., *Langmuir*, 2003, **19**, 2521.

196. a) Caruso F. and Schuler C., *Langmuir*, 2000, **16**, 9595; b) Caruso F. and Mohwald H., *J. Am. Chem. Soc*., 1999, **121**, 6039.

197. a) Mahtab R., Rogers J.P. and Murphy C.J., *J. Am. Chem. Soc*., 1995, **117**, 9099; b) Mahtab R., Harden H.H. and Murphy C.J., *J. Am. Chem. Soc*., 2000, **122**, 14.

198. Gonzalez M., Argarana C.E. and Fidelio G.D., *Biomol. Eng*., 1999, **16**, 67

199. Caswell K.K., Wilson J.N., Bunz U.H.F. and Murphy C.J., *J. Am. Chem. Soc*., **125**, 13914.

200. Bruchez M. Jr., Morone M., Gin P., Weisss S. and Alivisatos A.P., *Science*, 1998, **281**, 2013.

201. Aslan K., Luhrs C.C. and Perez-Luna V., *J. Phys. Chem. B*, 2004, **108**, 15631.

202. Gaberc-Porekar V. and Menart V., *Chem. Eng. Technol*., 2005, **28**, 1306.

203. Huang Z., Park J.I., Watson D.S., Hwang P. and Szoka F.C. Jr., *Bioconjugate Chem*., 2006, **17**, 1592.

204. Li Y.-C., Lin Y.-S., Tsai P.-J., Chen C.-T., Chen W.-Y. and Chen Y.-C., *Anal. Chem*., 2007, **79**, 7519.

205. Borrebaeck C.A.K., *Immunol. Today*, 2007, **21**(8), 37.

206. Sondi I., Siiman O., Koester S. and Matijevic E., *Langmuir*, 2000, **16**, 3107.

207. Kannagi R., Izawa M., Koike T., Miyazaki K. and Kimura N., *Cancer. Sci*., 2004, **95**(5), 377.

208. Niemeyer C.M. and Bulent Ceyhan, *Angew. Chem. Int. Ed*., 2001, **40**(19), 3865.

209. a) Zanchet D., Micheel C.M., Parak W.J., Gerion D., and Alivisatos A.P., *Nano Lett.*, 2001, **1**(1), 32; b) Zanchet D., Micheel C.M., Parak W.J., Gerion D., Williams S.C. and Alivisatos A.P, *J. Phys. Chem. B.*, 2001, **105**, 8861.

210. Tshikhudo R.T., Demuru D., Wang Z., Brust M., Secchi A., Arduini A. and Pecchini A., *Angew. Chem. Int. Ed*., 2005, **44**, 2

211. Sung K.-M., Mosley D.W., Peelle B.R., Zhang S. and Jacobson J.M., *J. Am. Chem. Soc.*, 2004, **126**, 5064.

212. Fan J., Chen S. and Gao Y., *Colloid. Surface. B*, 2003, **28**, 199.

213. Hong H.-G., Bohn P.W. and Sligar S.G., *Anal. Chem.*, 1993, **65**, 1635.

214. Hong H.-G., Jiang M., Sliger S.G. and Bohn P.W., *Langmuir*, 1994, **10**, 153.

215. Morghimi S.M., Hunter A.C. and Murray C.J., *FASEB J*., 2005, **19**, 311.

216. Pei R., Yang X. and Wang E., *Analyst*, 2001, **126**, 4.

217. Parak W.J., Pellegrino T. and Plank C., *Nanotechnology*, 2005, **16**, R9.

218. Gao X.H., Cui Y.Y., Lenson R.M., Cheung L.W.K. and Nie S.M., *Nature* Biotechnol., 2004, **22**, 969.

219. Tkachenko A.G., Xie H., Coleman D., Glomm W., Ryan J., Anderson M.F., Franzen S. and Feldheim D.L., *J. Am. Chem. Soc*., 2003, **125**, 4700.

220. Xu Z.P., Zeng Q.H., Lu G.Q. and Yu A.B., *Chem. Eng*., 2006, **61**, 1027.

221. Braydon D.J., *Drug Discov. Today*, 2003, **8**, 876.

222. Yang H. and Xia Y., *Adv. Mater.*, 2007, **19**, 3085.

223. Kawasaki E.S. and Player A., *Nanomedicine: Nanotechnology, Biology and Medicine*, 2005, **1**, 101.

224. Loo C., *Technol. Cancer Res.*, 2004, **3**, 33.

225. Derfus A.M., Chan W.C. and Bhatia S.N., *Nano Lett.*, 2004, **4**, 11.

226. Kirchner C., Liedl T., Kudera S., Pellegrino T., Javier A.M., Gaub H.E., Stolzle S., Fertig N. and Parak W.J., *Nano Lett.*, 2005, **5**, 331.

227. Bao G. and Bao X.R., *Proc. Natl. Acad. Sci. U.S.A.*, 2005, **9**, 997.

228. Matsumura Y. and Maeda H., *Cancer Res.*, 1986, **46,** 6387.

229. Yuah F., *Cancer Res.*, 1995, **55**, 3752.

230. Ferrari M., *Nature Rev. Cancer*, 2005, **5**, 161.

231. Drummond D.C., Meyer O., Hong K., Kirpotin D.B. and Papahadjopoulos D., *Pharm. Rev*., 1991, **51**, 691.

232. Metselaar J.M., Mastrobattista E. and Storm G., *Mini Reviews in Medicinal Chemistry*, 2002, **2**, 319.

233. Links M. and Brown R., *Expert Rev. Mol. Med.*, 1999, **1**, 1.

234. Bennis S., Chapey C., Robert J. and Couvreur P, *Eur. J. Cancer*, 1994, **30**(1)**,** 89.

235. Pissuwan D., Valenzuela S.M. and Cortie M.B., *Trends Biotechnol.*, 2006, **24**, 62.

236. Salata O.V., *J. Nanobiotechnology*, 2004, **1**, 1.

237. Brus L., *Appl. Phys. A*, 1991, **53**, 465.

238. Chander H., *Mater. Sci. Eng. R*, 2005, **49**, 113.

239. Mirkin C.A., Letsinger R.L., Mucic R.L. and Storhoff J.J., *Nature*, 1996, **382**, 707.

240. a) Zigmondy R.A., *J. Am. Chem. Soc*., 1909, **31**(8), 951; b) http://nobelprize.org/nobel_prizes/chemistry/laureates/1925/zsigmondy-lecture.pdf, 18 July 2008.

241. Bendersky L.A. and Gayle F.W., *J. Res. NIST*, 2001, **106**, 997

242. Kuchibatla S.V.N.T., Karakoti A.S., Bera D. and Seal S., *Prog. Mater. Sci*., 2007, **52**, 699.

243. Zheng M. and Huang X., *J. Am. Chem. Soc*., 2004, **126**, 12047.

244. Orfao A, Schmitz G., Brando B., Ruiz-Arguelles R., Basso G., Braylan R., Rothe G., Lacombe F., Lanza F., Papa S., Lucio P. and San Miguel J.F., *Clin. Chem.*, 1999, **4**, 1708.

245. Jennings C.D. and Koon K.A., *Blood*, 1997, **90**, 2863.

246. Lakhani S.A., Masud A., Kuida K., Porter Jr. G.A., Booth C.J., Mehal W.Z., Inayat I. and Flavell R.A., *Science*, 2006, **311**, 847.

247. Patrat H.K., Banerjee S., Chaudhuri U., Lahiri P. and Dasgupta A. Kr., *Nanomedicine: Nanotechnology, Biology, and Medicine*, 2007, **3**, 111.

# CHAPTER 2: SYNTHESIS OF COLLOIDAL GOLD NANOPARTICLES AND MONOLAYER PROTECTED CLUSTERS IN AQUEOUS AND NONAQUEOUS MEDIA

## 2.1. INTRODUCTION

Due to the interdisciplinary implications of nanosized materials, their synthesis requires considerable control over their composition, size, shape, stability and dispersion properties owing to applications in various scientific fields. This has led to a plethora of investigations relating to the property exploitation of these entities as biomolecular conjugates, metallics, thin films and semiconductors [1-6]. Many different synthesis protocols have been devised for the synthesis of gold and other noble metal nanoparticles, with the bulk-precipitation-based Turkevitch method [7] and the biphasic Brust [8] method at the forefront of this aproach.

The preparative methods are devised such that there is a capping agent that binds to the surface atoms of the nanoparticle, thus controlling the particle sizes and preventing particle aggregation, which tends to reverse the unique nanoparticle properties back to the bulk. A simplified scheme of the methods is presented in Figure 2.1. As illustrated, three approaches are followed namely, the citrate reduction and capping method, the Brust biphasic method and the direct reduction in the presence of a ligand. The choice of ligand can also introduce a secondary functionality to the nanoparticle surface. Bifunctional ligands are usually equipped with a thiol head-group (-SH) which attaches to the gold surface and a secondary group, either carboxyl (-COOH), amine ($-NH_2$), hydroxyl (-OH) or others depending on the desired purpose of the exercise.

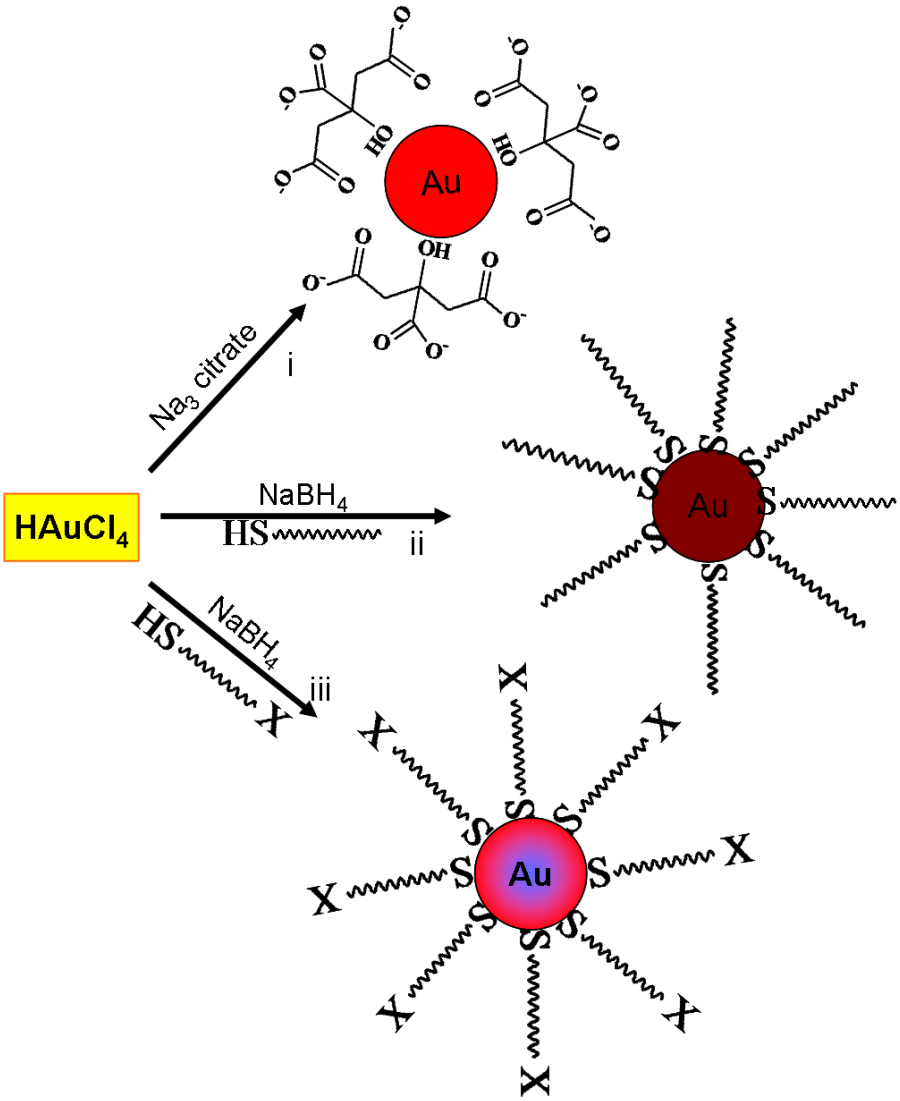


Figure 2.1. *Synthesis of gold nanoparticles by the reduction of the gold(III) salt; by (i) citrate reduction/capping, (ii) the Brust biphasic method and (iii) the direct reduction route in the presence of a bi-/multifunctional capping ligand.*

One of the new areas of interest involves the study of the properties of nanoparticles not only as single entities, but also as superstructures collectively termed as nanotectonics [9,10]. This dictates that the final properties depend on whether nanoparticles are comprised in organized monolayers or multilayer films or in solutions of organized or randomly dispersed entities. The choice of the synthesis protocol controls the design to produce nanoparticles in a tunable fashion both the chemical and physical properties. The

challenge has been the design of simple, low hazard methods using a minimum number of reagents to achieve this purpose. The useful nature of sulphur based ligands as effective capping agents for metal nanoparticles is well known [8,11]. It is therefore relevant to exploit this feature in the design protocols for highly functional nanostructures. The three most common ways for the synthesis of the gold nanoparticles by the chemical reduction of the gold(III) salt are shown in Figure 2.1. Before probing into the fundamentals of this investigation, an introduction to the nature of the attachment of the sulphur head group to the surface of gold is presented next.

## 2.2. THE GOLD-SULPHUR BOND

The formation and structure of self-assembled monolayers (SAMs) on a gold (substrate) is an aspect of materials research which has found many applications ranging from sensing, nanolithography and nanotechnology [12].The formation of the SAMs by the layering of the adsorbate on the surface of the substrate occurs at the reactive interface and therefore there are expected alterations in both the adsorbate and the substrate. In the case of a gold (substrate) and alkylthiolate adsorbate (SAMs), the ambiguous nature and extent of the interactions of the sulphur and gold is of great interest [13]. The interactions and subsequent binding of sulphur on the surface of gold is assumed for a straightforward process, motivated by the resistance of gold to form surface oxides as compared to other related metals such as silver. A schematic representation is given in Figure 2.2 illustrating the various proposed modes of binding of sulphur on gold surfaces.

The gold-sulphur bond has, for the most part, eluded any clear-cut explanations overriding the thriving advancements in the characterisation techniques over the years. X-ray crystallography, as the main characterisation technique of atomic structures, commonly suffers from multiple scattering effects in surface diffraction, and is hindered by the lack of reproducibility in synthesising single crystals of monolayer protected clusters (MPCs) [16].

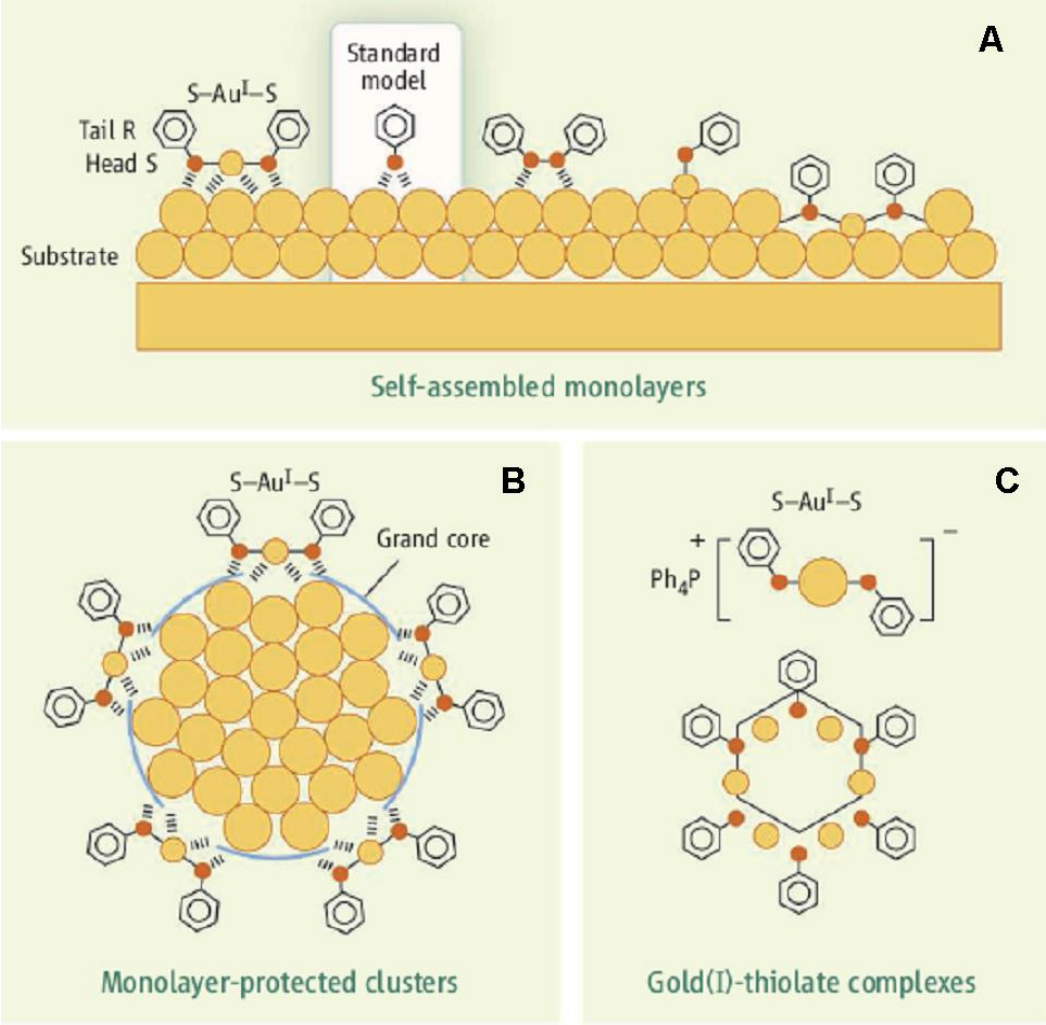


Figure 2.2. *A: Various proposed modes of binding of sulphur on gold surfaces [14], B: gold-sulphur binding modes of a 102 gold-atom cluster system [15] and C: well-characterised gold(I) thiolate complex.*

The composition of the common thiolates employed in forming SAMs on gold surfaces usually contain an organic group (R) linked to the sulphur head group which anchors onto the surface of the gold. The sulphur head group is essentially buried and its structure relative to the substrate can only be deduced through the presumption leading to propositions as depicted in Figure 2.2A [14]. This however has not gone without any challenges because these models do not strictly interrogate the different contributions as a result of the different chain lengths of the R group [17].

Attempting to solve this, large nanoclusters have instead been used as the substrate for the attachment of the alkanethiolates leading to the formation of the SAMs [18]. These large crystals show high stability and their chemical and electrical properties strongly mimic those of the corresponding SAMs. For a long time, no single crystal has been successfully grown and isolated until the pioneering work of Jadzinsky *et al.* [15.]. In their work, a single crystal of $Au_{102}$(p-MBA)$_{44}$ was isolated and its crystal structure analysed. The findings were unprecedented in that it was found that the commonly accepted theory of free thienyl groups attaching to the close-packed gold atoms of the substrate (Figure 2.2A) was not observed. Instead the binding group interacts in a similar manner such that the gold(I) thiolates interact weakly with the surface atoms of the "grand core" (Figure 2.2B), which is a truncated 79-atom cluster having gold-gold bonds resembling those of a bulk metal.

This finding of gold-sulphur bond agrees with the previously reported suggestion that the gold forms a homolytic bond with bond strength in the order of ca. 50 kcal/mol [19]. The one burning question also has been the whereabouts of the hydrogen of the –SH group during this process. Two possibilities have emerged; the reductive loss as dihydrogen ($H_2$) and with the presence of oxygen promoting the hydrogen loss in the form of water [20, 21].

### 2.2.1. Chapter Strategy

The following section details the synthesis of gold nanoparticles of different sizes and functionalities using different protocols. The protocols have been designed and selected to present a simplified method of synthesising "bare" nanoparticles, multifunctionalized, as well as highly stable Alkylthiol-capped gold nanoparticles. Further investigations encompass the effects of ligand amounts, ligand chain lengths and in some instances, the effects of pH and temperatures. For clarity purposes, nanoparticles possessing non-thiolated ligands (citrate and borohydride-capped) will be referred to as colloidal nanoparticles whereas those containing thiolates on the surface (alkylthiolates, amino acids, glutathione or bifunctional ligands) are referred as monolayer protected clusters [1, 22].

## 2.3. EXPERIMENTAL MATERIALS AND METHODS

### 2.3.1. Materials

Trisodium citrate (ACE AR, 99+%), hydrogen tetrachloroaurate trihydrate (Sigma-Aldrich, 99.9%), sodium borohydride (Aldrich, 99%), potassium carbonate (Sigma-Aldrich, ≥99.0%), 3-thiopheneacetic acid (Aldrich, 98%), 4-aminothiophenol (Aldrich, 97%), 2-mercaptoethanol (Sigma, 99.0%), L-cysteine (Aldrich, 97%), L-glutathione (Sigma-Aldrich, ≥99%), methanol (Sigma-Aldrich, 99.9%), ethanol (Sigma-Aldrich, 99.5%), hydrochloric acid (Sigma-Aldrich, 37%), toluene (Sigma-Aldrich, 99.5%), tetraoctylammonium bromide (Aldrich, 98%), octanethiol (Aldrich, ≥98.5%), hexanethiol (Aldrich, 95%) and dodecanethiol (Aldrich, 98+%) were purchased as indicated. High purity double-distilled water was used in the experimentation. Chemicals were either ordered from Sigma-Aldrich (Germany) or ACE (Germany) and were used without further purification.

### 2.3.2. Instrumentation

***UV-vis Optical Spectroscopy*.**

The UV-vis absorption measurements were conducted using a Perkin Elmer Lambda 20 UV-vis spectrophotometer. The spectra were recorded by measuring dilute samples in a quartz cell with a path length of 1 cm.

***Trasmission Electron Microscopy (TEM).***

TEM images were obtained with a Phillips CM120 Biotwin transmission electron microscope equipped with an EDAX detector and Gatan Crystorage. The specimens were prepared by dropping a dilute solution of the sample containing the nanoparticles on a carbon-coated copper grid (400 mesh) and allowing the solvent to dry out at room temperature. The images were captured using the embedded self-imaging system using a Megaview III digital camera.

### 2.3.3. Synthesis of Citrate-Capped Colloidal Nanoparticles (SM1-10)

A 10 mL of an aqueous solution of trisodium citrate (17 mM; 0.17 mmol) was added into 180 mL of boiling aqueous solution of tetrachloroaurate (0.3 mM; 0.05 mmol). The mixture was boiled under reflux for 30 minutes and the resultant solution was allowed to cool to room temperature. The solution was further stirred overnight followed by filtration before use. The same experimental procedure was follwed to influence the nanoparticle sizes by changing the stabilizer/reducing agent-to-gold salt ratio. Table 2.1 shows the list of quantities used to produce nanoparticles of different sizes (SM1-10).

Table 2.1. Reagents and quantities used for the investigation of the citrate-capped gold nanoparticles.

| **Sample Code** | **0.25 mM $HAuCl_4$ Volume** | **1% Trisodium citrate Volume** |
|---|---|---|
| SM2 | 250 mL | 5 mL |
| SM3 | 250 mL | 4 mL |
| SM4 | 250 mL | 3.75 mL |
| SM5 | 250 mL | 3 mL |
| SM6 | 250 mL | 2.5 mL |
| SM7 | 250 mL | 1.5 mL |
| SM8 | 250 mL | 1.08 mL |
| SM9 | 250 mL | 0.8 mL |

### 2.3.4. Synthesis of Borohydride-Capped Colloidal Nanoparticles (SM10)

A 375 μL aqueous tetrachloroaurate solution (0.1 M, 0.04 mmol) was mixed with 500 μL of an aqueous solution of potassium carbonate (0.2 M, 0.1 mmol) and the mixture was added into 100 mL of water. The contents were stirred in an ice bath for 5 minutes, then 5 mL of an aqueous solution of sodium borohydride (13 mM, 0.07 mmol) was added

dropwise. The reaction was allowed to continue for a further 60 minutes. The resultant gold nanoparticles were filtered through the Whatman 40 filter paper before use.

### 2.3.5. Synthesis of 3-Thiopheneacetic Acid-Capped MPCs (SM11)

Typically, 25 mL of an aqueous solution of 5 mM tetrachloroaurate (0.2 mmol) was mixed with a 10 mL aqueous solution of 3-thiopheneacetic acid (60 mM, 0.6 mmol) at room temperature. Following this, 10 mL of a freshly prepared sodium borohydride (0.01 g) solution was added quickly with vigorous stirring. The stirring was continued for 10 minutes and the resulting grape-red gold MPCs solution was centrifuged and washed twice with water.

### 2.3.6. Synthesis of 4-Aminothiophenol-Capped MPCs (SM12)

The 4-aminothiophenol-capped gold nanoparticles were synthesised in a simple one-pot reaction. Into 30 mL of an aqueous solution of tetrachloroaurate (20 mM, 0.6 mmol), 4-aminothiophenol (0.375 g, 3 mmol) was added. This was followed by a dropwise addition of 25 mL of an aqueous sodium borohydride solution (0.2 mM, 5.5 mmol) under vigorous stirring conditions. The stirring was maintained for a further 60 minutes followed by filtration. In a separate procedure, the 4-aminothiophenol-capped gold nanoparticles were synthesised at a regulated pH of 1.5.

### 2.3.7. Synthesis of 2-Mercaptoethanol-Capped MPCs (SM13)

In a typical experiment, 2-mercaptoethanol (1 mmol) was quickly added into 10 mL of an aqueous tetrachloroaurate (20 mM, 0.2 mmol) solution under stirring. This was followed by a drop-wise addition of 5 mL aqueous sodium borohydride (0.3 mM; 1.5 mmol) solution. The stirring was continued for a further 60 minutes and the resultant nanoparticles were analysed.

### 2.3.8. Synthesis of L-Cysteine-Capped MPCs (SM14)

To a 50 mL aqueous solution of tetrachloroaurate (12 mM, 0.6 mmol), 10 mL aqueous solution of L-cysteine (0.1 M, 0.1 mmol) was added. A 20 mL aqueous solution of sodium borohydride was slowly added with vigorous stirring. The mixture was further

stirred for 1 hour and the solution was allowed to stand overnight. This was followed by centrifugation (8000 rpm, 10 minutes) and the resulting pellet was washed twice with water to remove excess unreacted L-cysteine ligands. The resultant brown-red precipitate was redispersed in water.

### 2.3.9. Synthesis of L-Glutathione-Capped MPCs (SM15)

An 80 % methanol solution of L-glutathione (6.5 mM, 0.2 mmol, 25 mL) was added into 20 mL of a 50 % methanol solution of tetrachloroaurate (6 mM, 0.12 mmol) under constant stirring conditions. The stirring was continued for a further 30 minutes and 15 mL of freshly prepared sodium borohydride (0.18 mM, 2.6 mmol) dissolved in 60 % methanol was slowly added. The stirring was continued for a further one hour at room temperature. The resulting solution was evaporated to near dryness and excess methanol was used to wash the precipitate repeatedly. The nanoparticles in water were stored at 4 °C.

### 2.3.10. Synthesis of Alkylthiol-Capped MPCs (SM16-18)

A 30 mL of an aqueous tetrachloroaurate solution (30 mM, 0.9 mmol) was mixed with 80 mL toluene solution of tetraoctylammonium bromide (TOABr) (50 mM, 4 mmol). The mixture was stirred until all the tetrachloroaurate was transferred to the organic layer. An amount of 0.2 g of hexanethiol (1.7 mmol) was added to the organic layer and mixed thoroughly, followed by the slow addition of 25 mL of freshly prepared sodium borohydride (0.2 mM, 5 mmol) under vigorous stirring. The mixture was stirred for a further 4 hours and separated in a dropping funnel. The organic layer was reduced in a rotovapor to 15 mL and excess ethanol (400 mL) was added and the mixture was refrigerated at -18 °C for 12 hours, the precipitate was filtered and washed twice with ethanol. The nanoparticles (SM16) were redissolved in toluene for storage and further use.

Using a longer alkyl-chain ligand, octanethiol, the same experimental procedure for the synthesis of SM16 was followed, using the quantities as follows: tetrachloroaurate (30 mM, 0.9 mmol, 30 mL water), octanethiol (0.2g, 1mmol), sodium borohydride (0.2 mM,

5 mmol, 25 mL water) and tetraoctylammonium bromide (50 mM, 4 mmol, 80 mL toluene) to produce SM17.

Dodecanethiol-capped gold nanoparticles were also synthesised following the experimental procedure discussed for the synthesis of SM16 using tetrachloroaurate (30 mM, 0.9 mmol, 30 mL water), dodecanethiol (0.202 g, 1 mmol), sodium borohydride (0.2 mM, 5 mmol, 25 mL water) and tetraoctylammonium bromide (50 mM, 4 mmol, 80 mL toluene) to produce SM18.

## 2.4. RESULTS AND DISCUSSION

A schematic representation of the reactions and the relevant ligand structures used for the synthesis of colloidal gold nanoparticles and monolayer protected clusters is presented in Figure 2.3 below. As depicted in Figure 2.3 four routes were followed for the synthesis. The direct reduction and capping by the citrate (SM1-SM9) and the borohydride reduction method (SM10) for the synthesis of colloidal nanoparticles was used. Another procedure involved the use of thiolated multifunctional ligands for the synthesis of gold MPCs (SM11-SM15) and lastly the Brust biphasic protocol was followed for the synthesis of alkylthiolate-capped gold nanoparticles of smaller sizes (SM16-SM18). Discussion on the results for each of these reactions is presented next.

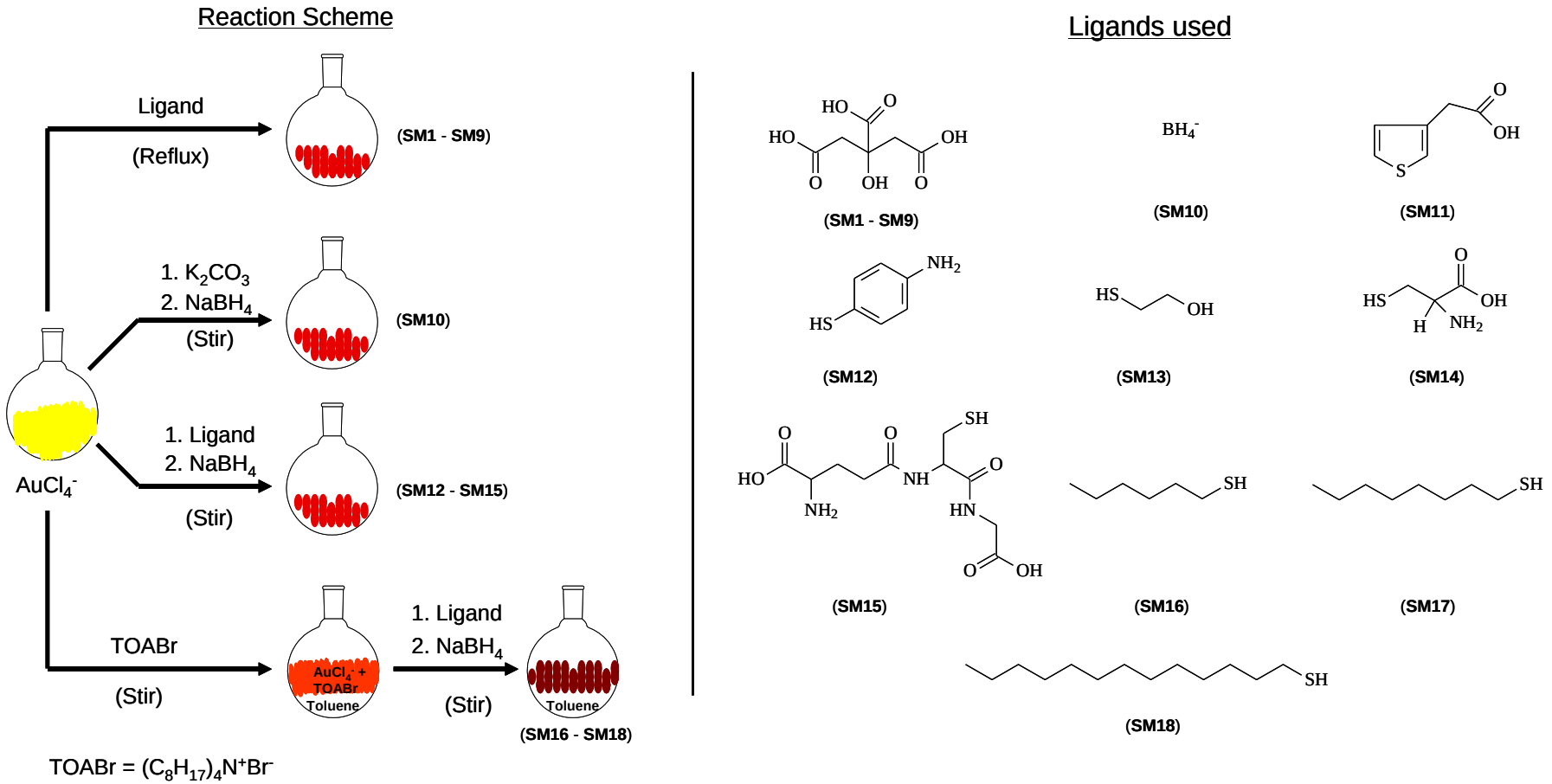


Figure 2.3. *A schematic representation of the various colloidal gold nanoparticles and MPCs synthesised in this work.*

***Citrate capped colloidal nanoparticles*** **[SM1-SM9].**

On addition of the citrate into the boiling tetrachloroaurate solution, the colour changed from pale yellow to colourless to dark blue within the first two minutes, and then ruby-red after three minutes of reaction time. This colour transition confirms the formation of the citrate-capped gold nanoparticles [7]. When the pale yellow colour ($AuCl_4^-$) fades, it signifies the formation of the gold atoms, which nucleate and linearly assemble to form the dark-blue nanowires. The nanowires subsequently destabilise with an increase in size, followed by fragmentation and cleavage to form the citrate-capped gold nanoparticles [23].

The nanoparticle yields were observed to be higher at high citrate:gold ratios and very low at smaller citrate amounts. The time taken for the complete formation of the nanoparticles was dependent on the amount of the citrate added, ranging from 2-4 minutes (SM1) to about 12-15 minutes (SM9) for the larger particles. Unique colour changes of the colloidal gold nanoparticles were observed with changes in the citrate:gold ratios the largest citrate amount yielded deep red coloured nanoparticles and slightly blue colour at smaller volumes. The smaller nanoparticles (14-40 nm) showed no scattering, with the red colour observed using both transmitted and reflected light. The larger nanoparticles (60-120 nm) showed a brownish-blue colour in reflected light and a blue colour in transmitted light. This is due to the 50 nm average free delocalisation path of gold, dictating that all the interactions be at the surface for particle diameters smaller than this [24-27].

Figure 2.4 shows the UV-vis absorption spectra of the citrate-capped colloidal nanoparticles synthesised at different citrate:gold ratios. The SPR absorption of the nanoparticles was observed at 520 nm, in agreement with the expected SPR aborption of the nanosized gold particles at this size range [7]. The nanoparticles at higher citrate amounts showed a relatively narrow absorption peak (SM1-5), evidence of the narrow size distribution of the nanoparticles. The nanoparticles with larger diameters (73-120 nm) (SM7-9) showed broader tailing peaks, due to the polydispersity of the nanoparticles.

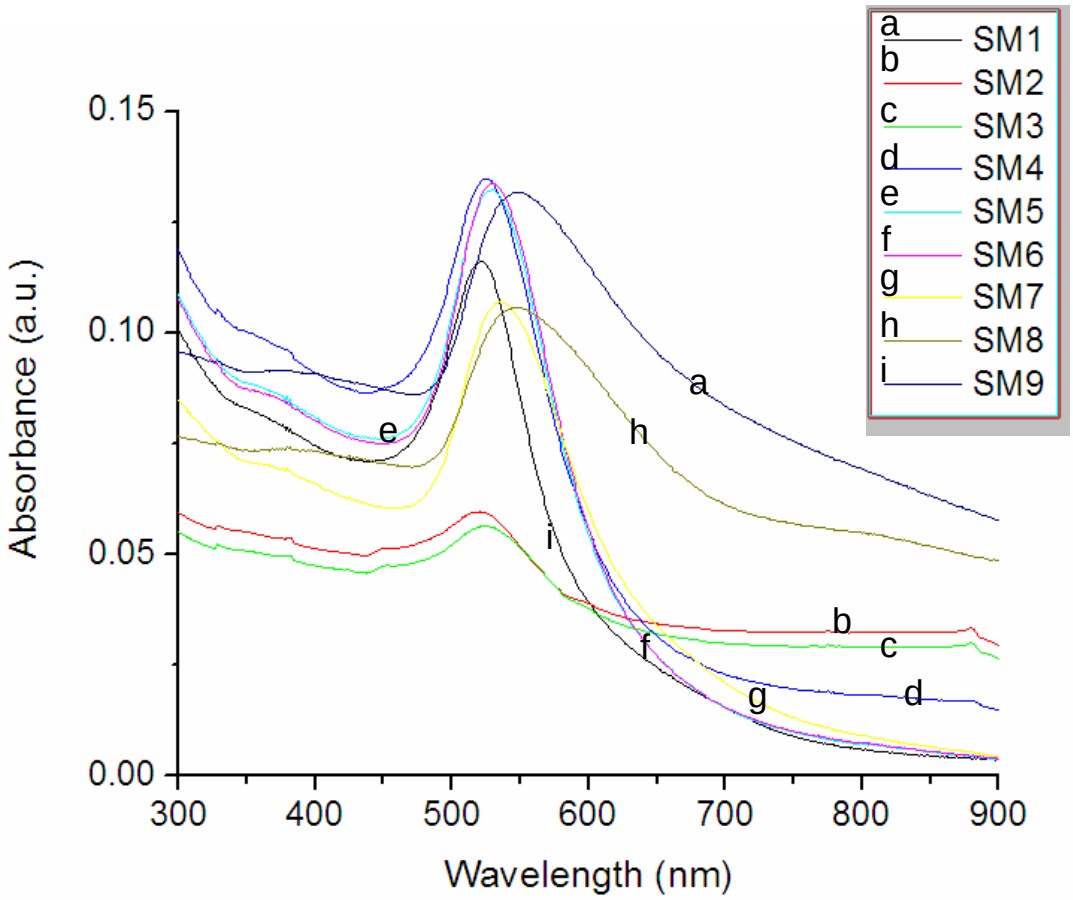


Figure 2.3. *Optical absorption spectra of the citrate-capped colloidal gold nanoparticles synthesised at different citrate-to-gold ratios.*

The TEM micrographs of the citrate-capped colloidal gold nanoparticles are presented in Figures 2.4, 2.5 and 2.6 below. For smaller particles (SM1-SM6), there is a noticeable dominance of the spherical nanoparticles over any other shapes. As the citrate:gold ratio decreases further, there is an onset of non-spherical particles (SM7-SM9); these pod-shaped nanoparticles have very poor size distribution patterns. As shown in Figure 2.6, at the lowest citrate:gold ratio (SM9), only smaller sized nanoparticles have spherical shapes. These nanoparticle systems showed no aggregation signs even after three months of storage. The observations are summarised in Table 2.2.

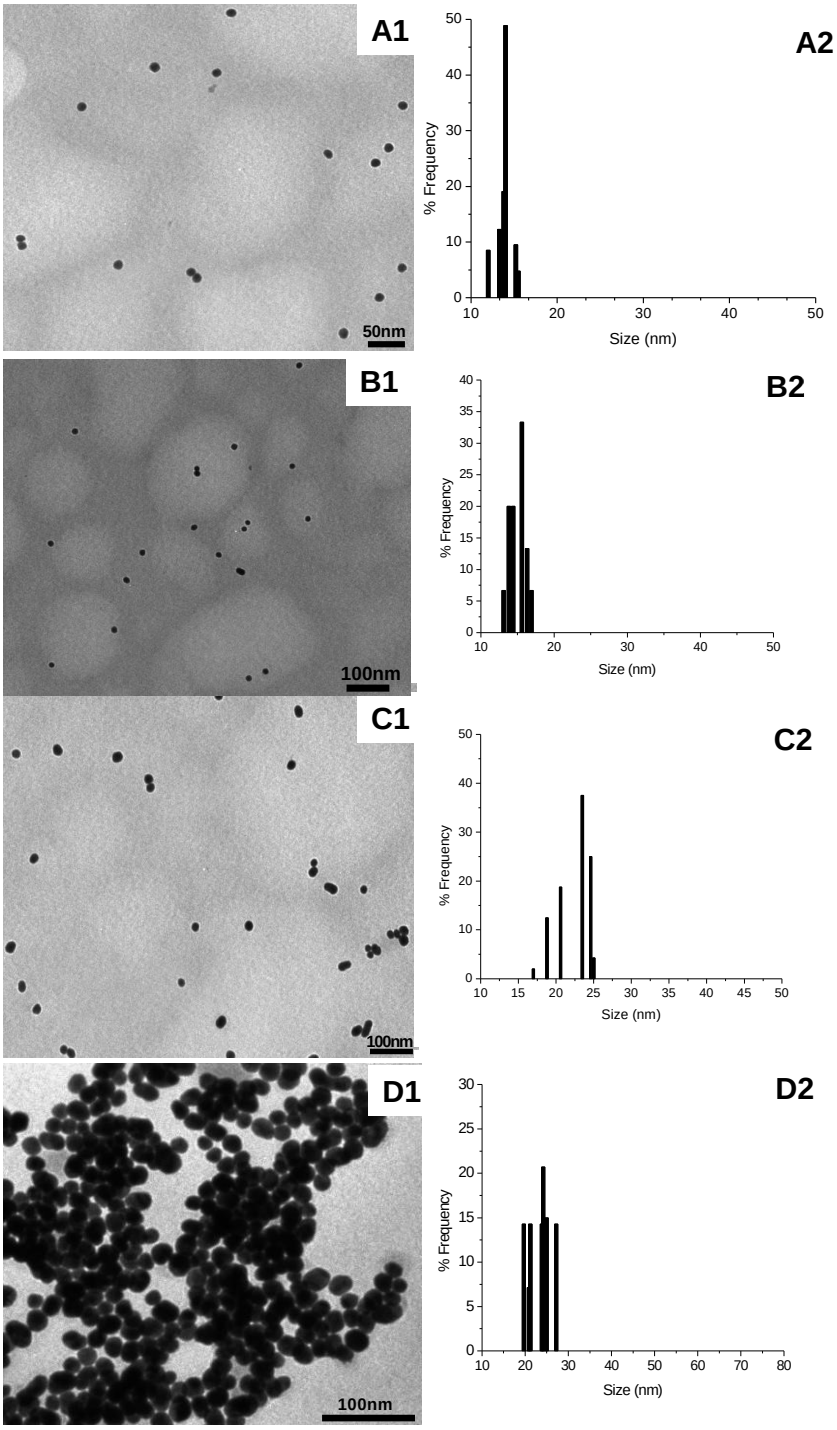


Figure 2.4. *TEM micrographs and the corresponding size distribution analysis of the citrate-capped colloidal nanoparticles: A) SM1, B) SM2, C) SM3 and D) SM4.*

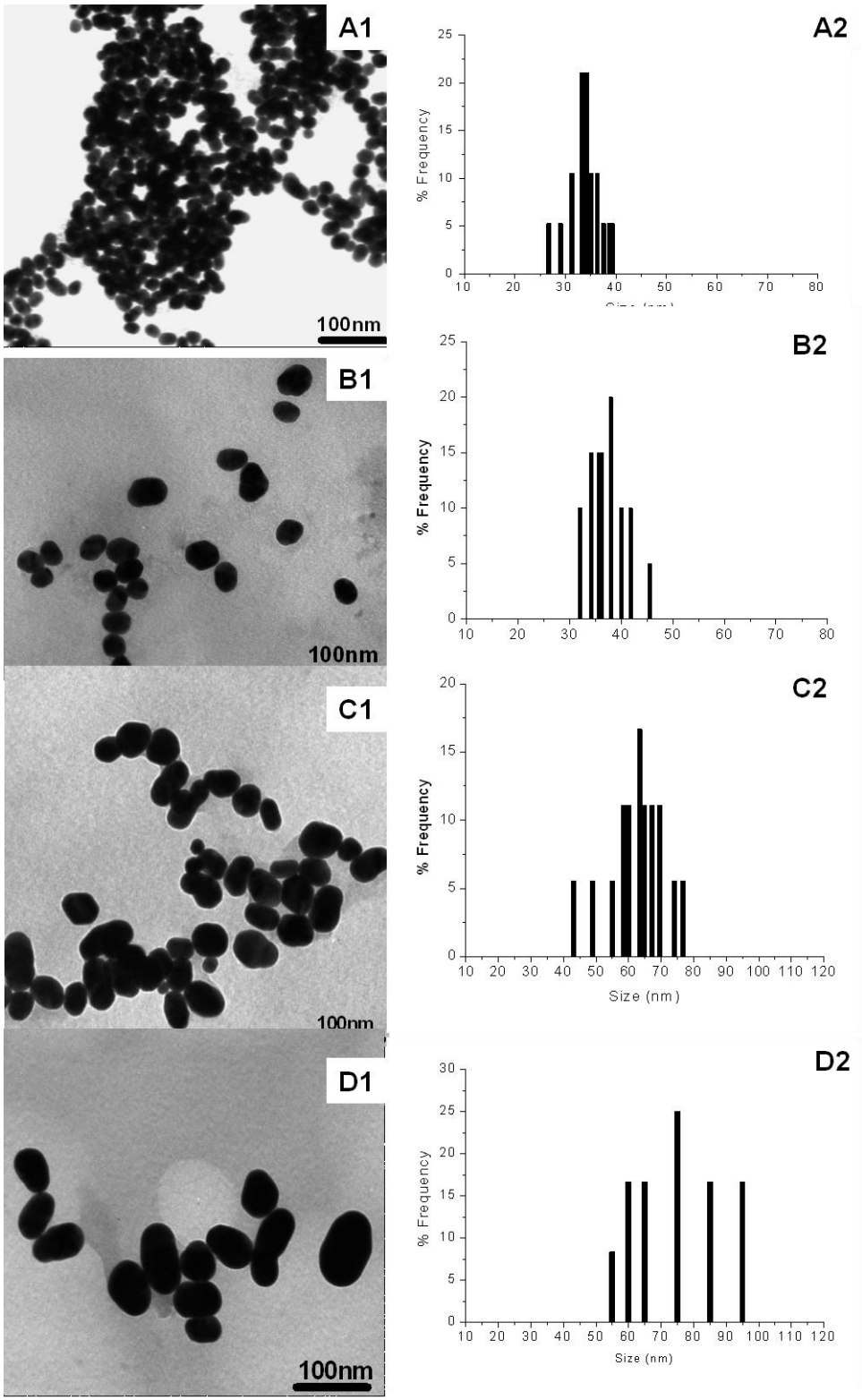


Figure 2.5. *TEM micrographs and the corresponding size distribution analysis of the citrate-capped colloidal nanoparticles: A) SM5, B) SM6, C) SM7 and D) SM8.*

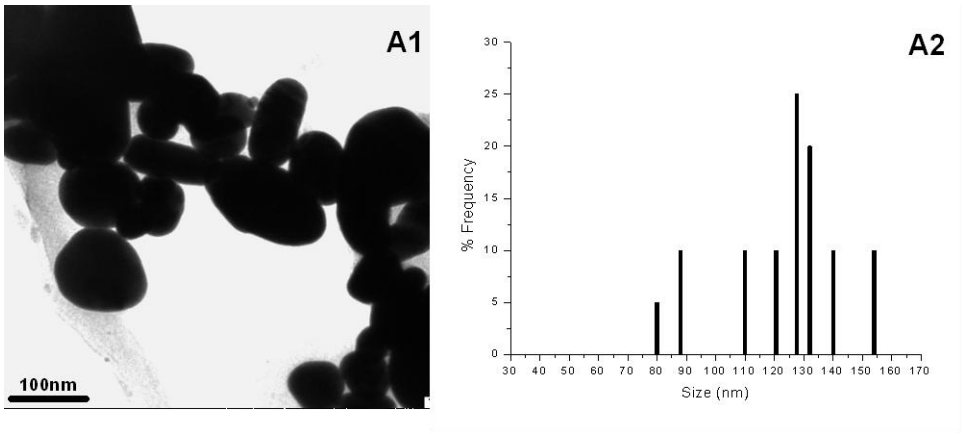


Figure 2.6. *TEM micrograph of the citrate-capped colloidal nanoparticles (SM*9).

Table 2.2. Summary of the results in the citrate-capped gold nanoparticles investigation.

| **Sample Code** | **Citrate : $HAuCl_4$ Mole Ratio** | **SPR Absorption** | **Average Particle Size** |
|---|---|---|---|
| SM1 | 3.15 | 520 nm | 14 ± 1.3 nm |
| SM2 | 2.72 | 522 nm | 15 ± 1.5 nm |
| SM3 | 2.24 | 524 nm | 21 ± 2.7 nm |
| SM4 | 2.05 | 526 nm | 23 ± 3.3 nm |
| SM5 | 1.63 | 530 nm | 34 ± 4.1 nm |
| SM6 | 1.36 | 531 nm | 38 ± 4.4 nm |
| SM7 | 0.82 | 537 nm | 62 ± 10.2 nm |
| SM8 | 0.59 | 545 nm | 73 ± 15.4 nm |
| SM9 | 0.44 | 547 nm | 119 ± 25.3 nm |

Subsequent observations, showed no structural modifications and absorption changes for the smaller nanoparticles (SM1-SM6) after months of room temperature storage. This was not observed for the larger particles (SM8 and SM9), with the colloidal nanoparticles both sticking on the storage bottles and also settling out of solution in less than a week of

storage at room temperature. This process can be attributed to the reduced surface charge of the particles thus permitting irreversible aggregation. These results offer a simple and useful way of manipulating the size and subsequently the properties of the nanoparticles for different applications.

***Borohydride-Capped Colloidal Nanoparticles*** **[SM10].**

An addition of sodium borohydride saw an immediate change in the solution colour from yellow to purple and then pink-red, signifying the formation of small core colloidal gold nanoparticles. The formation of the colloidal gold nanoparticles was investigated using UV-vis absorption, with the nanoparticles showing the plasmon resonance absorption the expected region at 519 nm (Figure 2.7A). This absorption is a typical gold surface plasmon vibration excitation for colloidal gold nanoparticles when they interact with electromagnetic radiation [24-27].

The reasonable narrow absorption peak indicated that the particles were not aggregated and the capping was effective. This was further revealed by the TEM images shown in Figure 2.7B, which showed dispersed particles. The particle sizes were obtained from the TEM micrograph showed an average particle size of 5.5 ± 1.6 nm (Figure 2.7C).

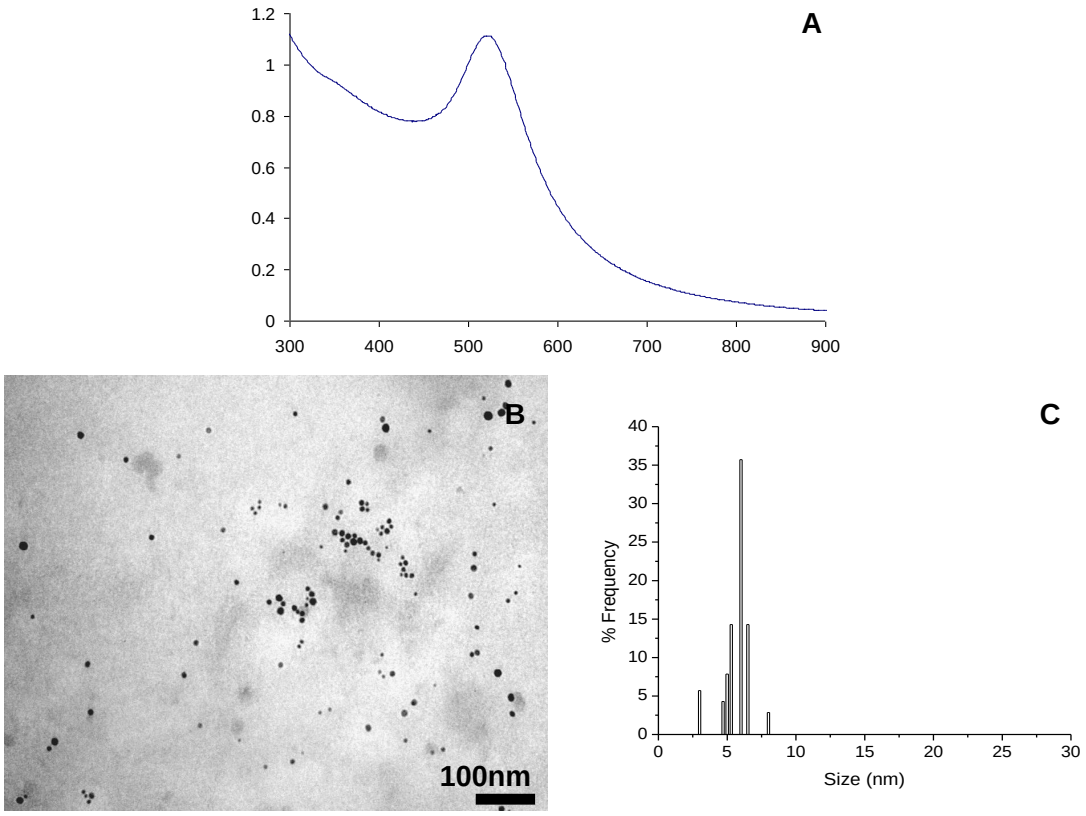


Figure 2.7. *A) Optical absorption spectrum, B) a TEM micrograph and C) the size distribution analysis of the borohydride-capped colloidal nanoparticles.*

The "bare" nature of these nanoparticles offers a possibility of introducing further functionalities on the surface through ligand place-exchange reactions. The nature of the borohydride capping on the surface of the gold only allowed for a limited stability with time. No broadening or shifts were observed in absorption and structural properties of these nanoparticles after a week of storage at room temperature. On long term storage, for three months, minor precipitates were formed, requiring particle filtration before use.

***3-Thiopheneacetic Acid-Capped MPCs* (SM11).**

A facile one-step, room temperature synthesis of the 3-thiopheneacetic acid-capped gold MPCs was achieved by the action of the strong reducing agent, sodium borohydride, on the gold (III) salt in the presence of acid. The 3-thiopheneacetic acid (3-TA) is a useful heterocyclic compound which can be polymerised to form poly(3-thiopheneacetic acid) [28], which has interesting bioelectrochemical and photochemical properties in

homogeneous competitive immunoassays [29]. The use of 3-TA as a capping and reducing agent for the preparation of gold nanoparticles has been reported in the literature [30], citing reaction temperatures as high as 80 °C.

Here, the synthesis was conducted at room temperature by employing a strong reducing agent. The synthesis and formation of the 3-TA-capped gold MPCs was confirmed by the immediate colour change from yellow to red on addition of the reducing agent. The formation of the MPCs was probed using UV-vis spectroscopy with the optical absorption peak observed at 530 nm, concurring with the expected surface plasmon resonance region for gold nanoparticles (Figure 2.8A) [24-27].

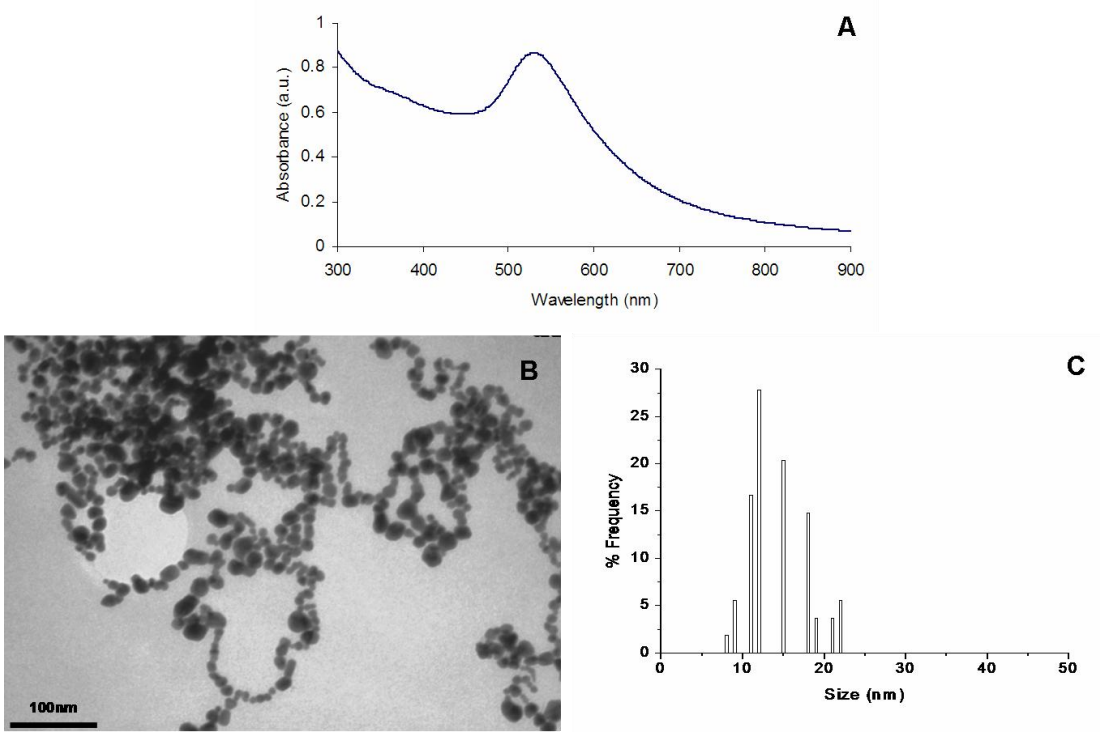


Figure 2.8. *An A) absorption spectrum, B) TEM micrograph and C) the particle size distribution graph of the 3-TA-capped gold MPCs.*

The absorption peak was fairly broad owing to the polydipersity of the nanoparticles. The TEM measurementes of the 3-TA-capped gold MPCs showed predominantly spherical particles (Figure 2.8B). The MPCs showed partial linkages (semi-linear superstructures) that can be attributed to the secondary acid functional group (-COOH), which can anchor onto the gold surface. An evidence of some disordered

structures showed that the assembly of these patterns is relatively poor which might be due to the short chain of the 3-TA capping agent. The particle sizes range between 9-22 nm, with an average particle size of 15 ± 5.2 nm. Similar linkage patterns have been reported for gold MPCs by the usage of controlled conditions and multi-capping agents [31]. The MPCs tended to settle into precipitates after three months of storage due to aggregation.

***4-Aminothiophenol-Capped Nanoparticles* (SM12).**

A structural analogue of phenol, 4-aminothiphenol contains both an amine ($-NH_2$) and hydroxyl (-OH) functional groups, with the thiol group anchoring preferably on the gold particles. The loss of the hydrogen of the 4-aminothiophenol produces thiophenolate anions, which can also be embedded on the surface of the nanoparticle. The ability of the amine group to attach to the gold nanoparticle surface enhances the possibility of forming networks of particles in one, two and three dimensions of the nanoparticles leading to the formation of superstructures. There are also numerous sites for hydrogen bonding which further enhances the possibility of superstructure formation.

Here, the addition of the 4-aminothiophenol changed the colour of the tetrachloroaurate solution from yellow to white. This significant change in colour can be attributed to the reduction of gold(III) to gold(I) by the thiol. Following this, the addition of $NaBH_4$ solution changed the colour from white to violet and then red, signifying the formation of the gold MPCs.

The optical absorption spectrum of the resultant nanoparticles is presented in Figure 2.9A, the absorption wavelength maximum was observed at 590 nm. This value was in agreement with the expected plasmon absorbance of the gold nanoparticles. The broadness and red-shift of the absorption peak indicate a severe degree of aggregation of the MPCs. This was confirmed by the TEM measurements (Figure 2.9B) with the nanoparticles showing major aggregation. This phenomenon is also enhanced by the likelihood of the ligands forming hydrogen bonds in solution. These MPCs however, were redispersible in acidic media (Figure 2.9C), with sizes ranging from 1 to 10 nm.

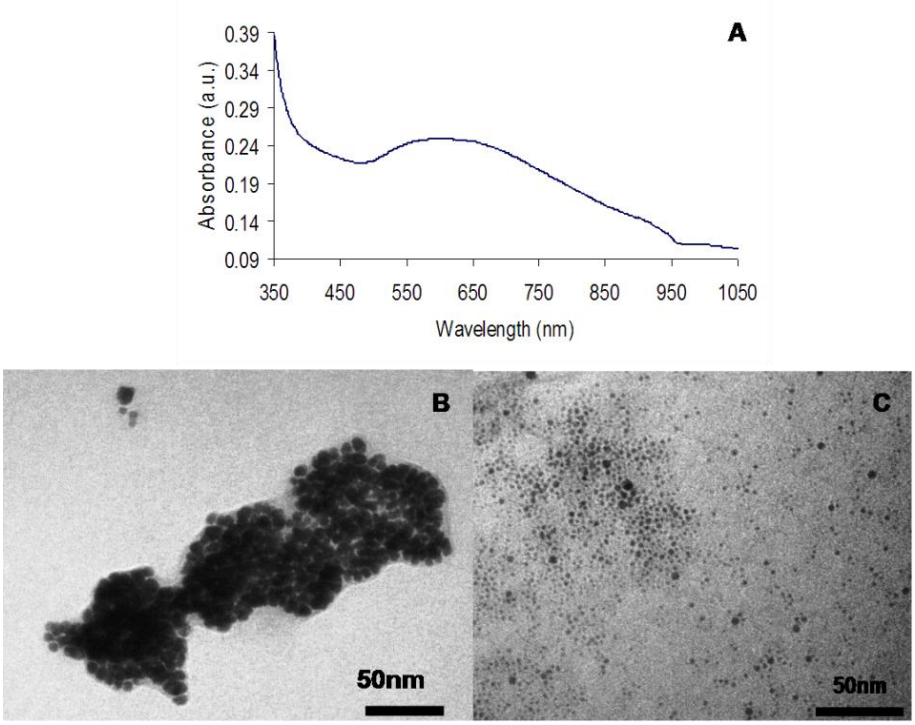


Figure 2.9. *The A) optical absorption spectrum, B) TEM micrograph of the as-prepared gold MPCs and C) a TEM micrograph of the MPCs dispersed in water at pH 2.0.*

Guided by the possibility of dispersing these nanoparticles in acidic media, synthesis at lower pH (2.0) was investigated. The optical absorption is presented in Figure 2.10A, the plasmon absorption was observed typically at 536 nm. The shoulder on the peak showed a possible indication of MPCs with small average sizes.

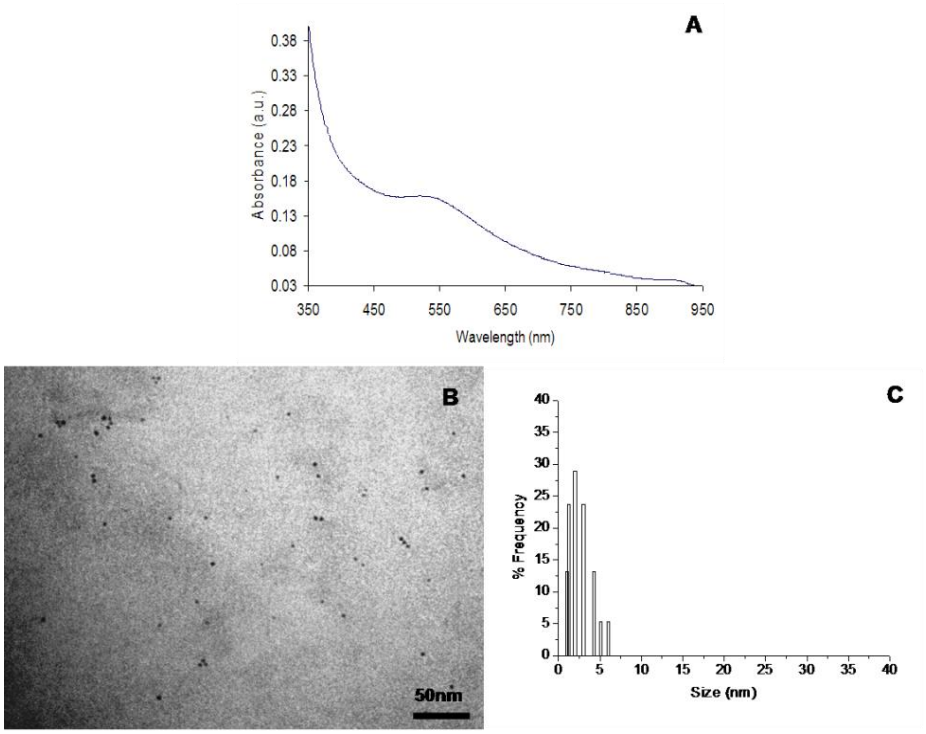


Figure 2.10. *Optical absorption spectrum (A), B) TEM micrograph and C) size distribution analysis of the 4-aminothiophenol-capped gold MPCs synthesised at pH 1.5.*

The particle sizes acquired from the TEM measurements are presented in Figure 2.10B along with the corresponding size distribution analysis (Figure 2.10C). Very small monodispersed MPCs were obtained, with an average size of 3.2 ± 1.9 nm.

***2-Mercaptoethanol-Capped Gold MPCs* (SM13).**

The ability of 2-mercaptoethanol to reduce and disrupt the intra- and intermolecular disulfide (S-S) bonds in proteins is a well known phenomenon [32]. This is possible in both tertiary and quaternary protein structures of; and 2-mercaptoethanol has thus been applied in many protein studies. When 2-mercaptoethanol was added into the yellow tetrachloroaurate solution, the colour changed to milky-white, signifying the reduction of $Au^{3+}$ to $Au^{+}$. On addition of the strong reducing agent (sodium borohydride), the colour changed to violet-red, confirming the formation of the gold MPCs. To substantiate this, optical absorption properties were measured and the spectra are presented in Figure 2.11A.

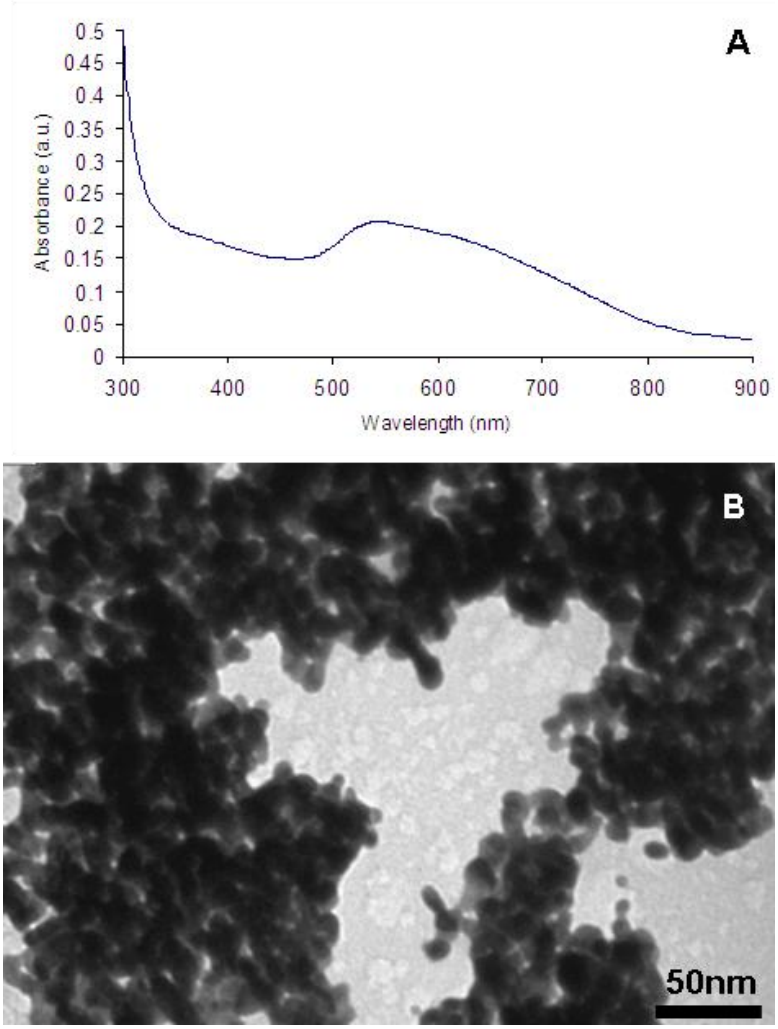


Figure 2.11. *Optical absorption (A) and B) TEM micrograph of 2-mercaptoethanol-capped gold MPCs.*

The absorption peak was red-shifted from the typical plasmon absorbance, and observed at 620 nm. The peak was very broad, typical to the aggregation of the particles and formation of other superstructures. This was further proved from the TEM measurements, which shows severely aggregated MPCs (Figure 2.11B). The MPCs showed low stabilities, settling out of solution after a months of storage.

***The L-Cysteine-Capped MPCs* (SM14).**

L-Cysteine is an acidic amino acid abundantly employed in biochemical and electrochemical studies [34]. An in depth study of the behaviour of this amino acid on solid surfaces has been reported elsewhere [35,36]. The synthesis of the L-cysteine-capped gold MPCs relies on the attachment of the sulfhydryl end of the amino acid to the nanoparticle surface. L-Cysteine is one of the common component residues of most proteins, and therefore it plays an important role in many protein studies. It also imparts water-solubility and stability to the MPCs. The formation of the gold MPCs was observed by the immediate appearance of a red colour on addition of the reducing agent with the final colour being brown-red. The optical and structural analysis of the L-cysteine-capped MPCs is presented in Figure 2.12.

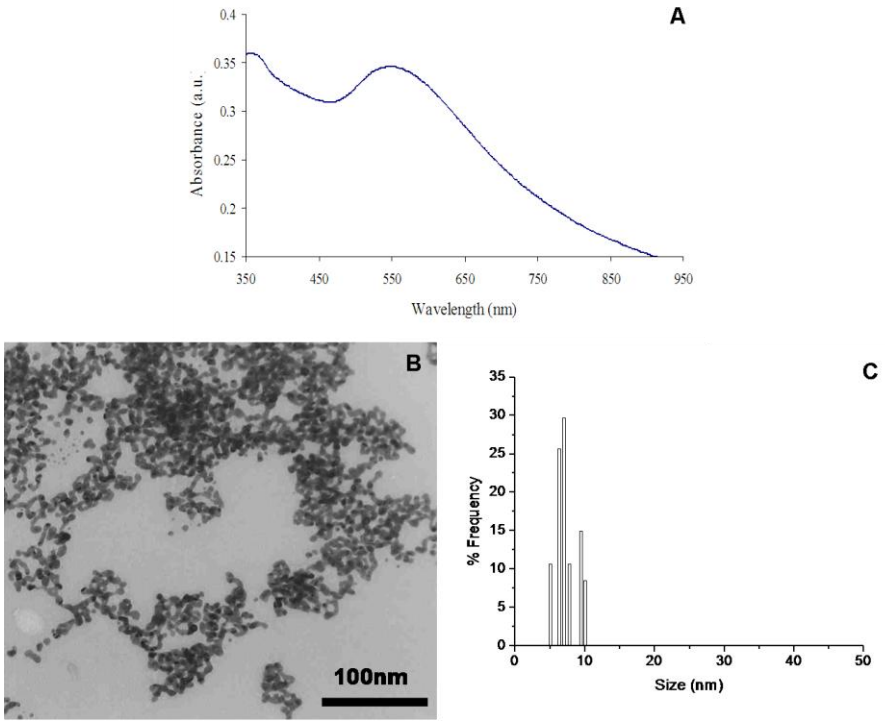


Figure 2.12. *Optical absorption spectrum A), B) TEM micrograph and C) the particle size distribution graph of L-cysteine-capped gold MPCs.*

The formation of the MPCs was probed using UV-vis absorption measurements (Figure 2.12A). A broad absorption peak centred at 550 nm was observed, signifying relative

aggregation of the nanoparticles. This can be attributed to the attachment of a considerable number of gold nanoparticles onto the amine and carboxyl groups of the amino acid and the relative small size of the capping ligand (L-cysteine). This observation was in agreement with the absorption peak at 560 nm observed in previous studies of capping gold MPCs with L-tryptophan amino acid [35]. The TEM was used to study the particle size and distribution as presented in Figures 2.12B and C. In agreement with the broad absorption patterns, the L-cysteine-capped gold nanoparticles showed a considerable degree of aggregation.

Semi-linear linkage arrangements were observed, which were attributed to the secondary functional groups of the amino acid enabling cross-linking between neighbouring MPCs. The MPCs had an average size of 7.6 ± 1.9 nm. The MPCs showed high levels of water solubility even at the noticeable aggregation levels. They also showed good stability after three months of storage at room temperature, further strengthening the case for L-cysteine as an effective capping agent.

***The L-Glutathione-Capped* MPCs (SM15).**

Glutathione (GSH) is a short tripeptide *N*-γ-glutamyl-cystenyl-glycine (γ-Glu-Cys-Gly), highly water soluble and is an essential component of the glutathione transferase which is a well known detoxification enzyme and also functions in prostaglandin, steroid hormone synthesis and fusion protein synthesis [37]. GSH has been seen to share similar stability and robustness as its hydrophobic *n*-alkyl analogues but is also conveniently water soluble [39]. The Au:SG (SG refers to the bound glutathione layer) clusters provide enhanced catalytic and electrolytic activities of the metal cores. The enhanced optical properties also form the basis of their applications in areas such as colorimetric probes and sensors.

The redox reaction that occurs between the GSH and gold in the presence of the capping agent is a stoichiometric process that can be summarised in the following reaction [39]:

$$3GSH + Au^{3+} \leftrightarrow Au^{0} + \tfrac{3}{2} GSSG + 3H^{+}$$

Au(0) is the metallic centre covered by a layer of GS (reduced GSH) or GSSG (oxidised GSH) adsorbate groups. On addition of the GSH to the gold salt, the solution colour changed from light brown to milky white on continued stirring. The milky colour

signified the formation of the polymeric Au(I)SG. The addition of sodium borohydride caused the immediate decomposition of this polymer and the subsequent formation of the Au(0) cores. The use of mixed solvents was necessary to prevent any uncontrolled reduction of the polymer by the strong reducing agent. Figure 2.13A shows the absorption spectrum of the Au:SG clusters.

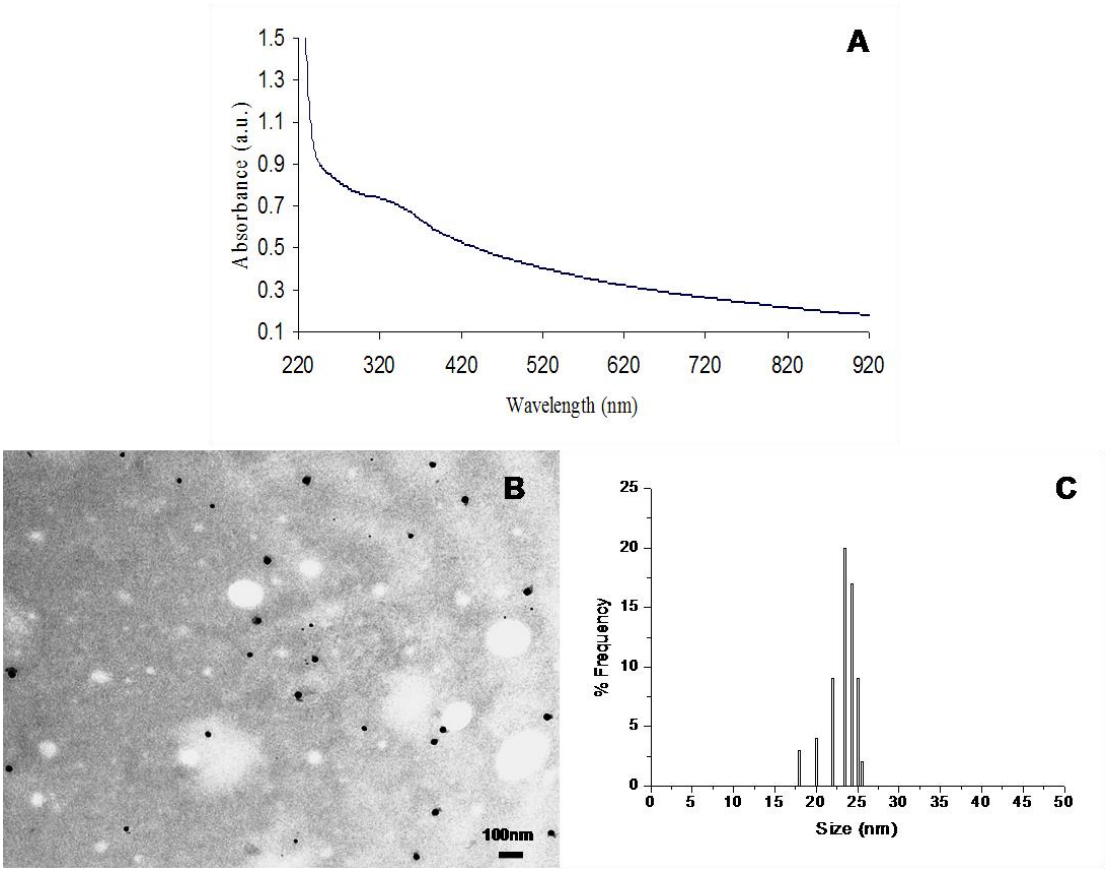


Figure 2.13. *Optical absorption spectrum(A), B) TEM micrograph and C) size distribution analysis graph of the GSH capped MPCs.*

The strong absorption at lower wavelengths is as a result of the fully reduced metallic Au(0) compound and a many electron system [38]. The TEM micrograph (Figure 2.13B) of the Au:SG clusters showed spherical particles with an average particle size of 22.6 ± 1.9 nm. This observation showed that the steric bulkiness of the tripeptide successfully limited any uncontrolled growth and kept the particle size range fairly low. The particles were observed to be completely soluble in water, which is necessary in the

biological applications for these materials. These nanoparticles showed no signs of aggregation on long term storage at 4°C and under room temperature conditions. The L-glutathione was heated at 80 °C for an hour and both absorption and structural measurements were conducted, as presented in Figure 2.14. On visual inspection, no major changes were observed during this process.

The absorption spectra (Figure 2.14A) showed a plasmon absorption peak at 570 nm. The peak was broad, signifying a non-uniform pattern of the nanoparticles. The nanoparticles showed severe aggregation patterns on the TEM analysis (Figure 2.14B).

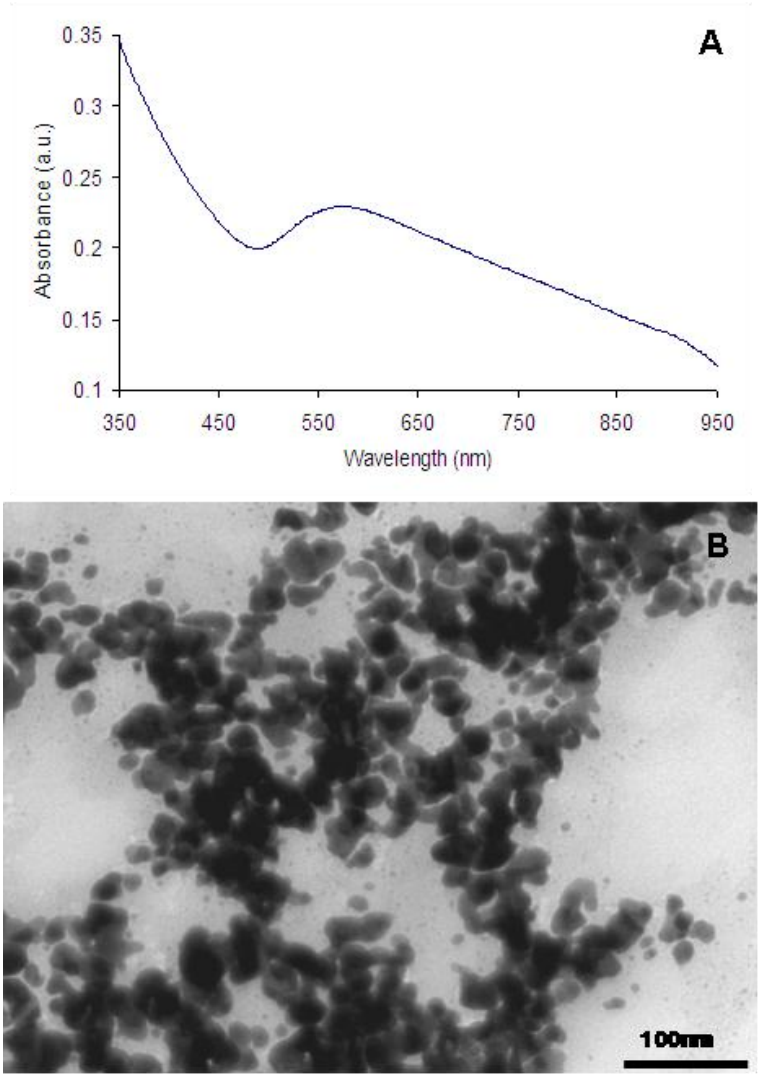


Figure 2.14. *Optical absorption (A) and (B) TEM micrograph of the GSH capped MPCs after heating at 80 °C.*

These observations are unprecedented and can be credited to the complete decomposition of the Au:SG clusters at elevated reaction temperature conditions indicating that this type of cluster lacks thermal stability.

***Alkylthiol-Capped MPCs*** **(SM16, SM17 and SM18).**

The synthesis of alkylthiolated gold MPCs represents one of the most dependable and reproducible ways of making small clusters of gold. This method was pioneered by Brust *et al*. in the synthesis of dodecanethiol-capped gold MPCs [8]. The general synthetic protocol involved a two-phase water/toluene system, whereupon the tetrachloroaurate ions were transferred from the aqueous phase to the organic phase by the action of the TOABr surfactant, and the subsequent reduction by a strong reducing agent in the presence of the capping agent. Here, a similar protocol was followed with three alkanethiolate ligands of different chain lengths, hexanethiol ($C_6SH$), octanethiol ($C_8SH$) and dodecanethiol ($C_{12}SH$).

The process through which the $AuCl_4^-$ is transferred into the organic phase is mediated by the surfactant TOABr, turning the colour of the gold salt from yellow to deep orange. This colour is due to the gold-TOABr complex $N(C_8H_{17})_4^+AuCl_4^-(C_6H_5Me)$ [8]. On addition of the relevant thiol ligand, the colour quickly faded into dark milky white, signifying the reduction of gold(III) to gold(I) by the thiol. On addition of sodium borohydride, the colour changed within the first few seconds from deep orange to deep brown, indicating the formation of gold MPCs. The optical absorption spectra of the alkylthiol-capped gold nanoparticles are presented in Figure 2.15. All the absorption wavelengths of the nanoparticles were in the region of the expected gold SPR absorption.

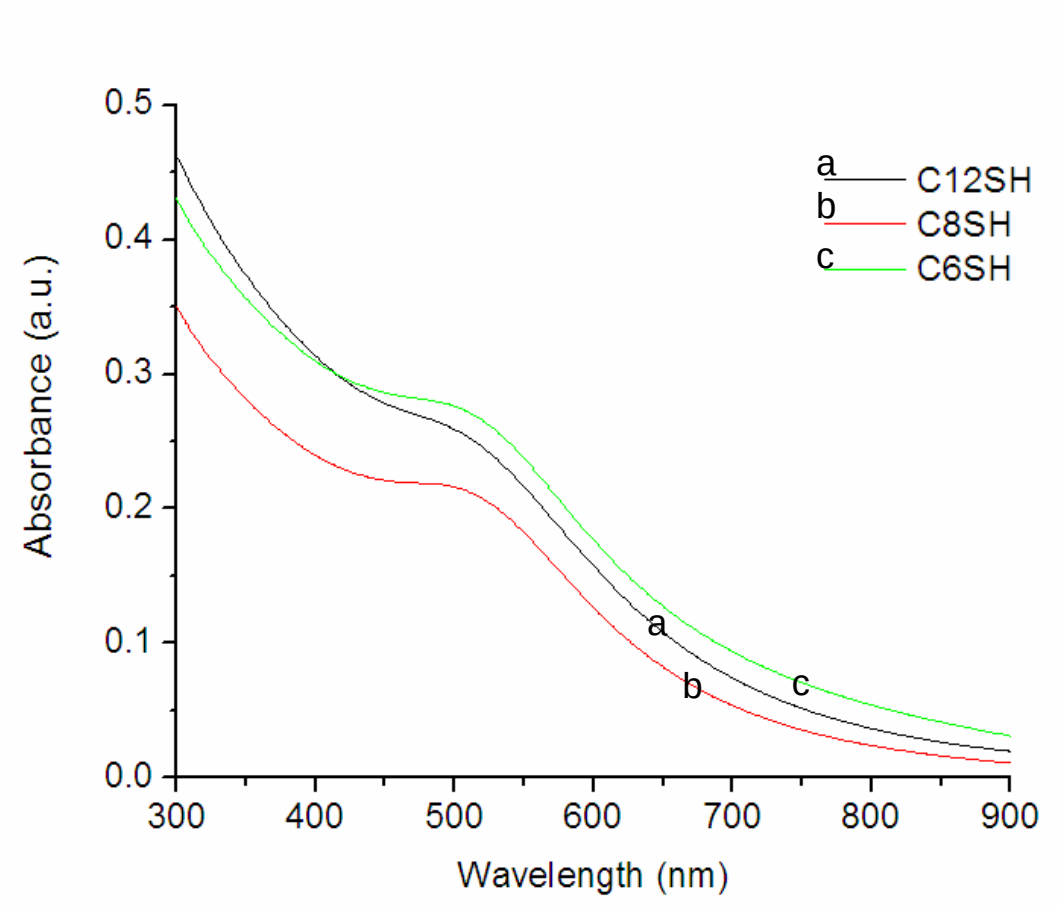


Figure 2.15. *Optical absorption spectra of the alkylthiol-capped gold MPCs.*

The nanoparticles showed absorptions with diminished peak intensities, suggested a decrease in the cluster sizes [39]. The surrounding optical solvent dielectric interactions also contribute somewhat to this unique observation in small nanoparticles [40]. The dodecanethiol-capped ($C_{12}SH$) nanoparticles show a plasmon band (510 nm) that is almost undetectable, which is an indication of the total loss of the bulk character [41]. Both the octanethiol- ($C_8SH$, 518 nm) and hexanethiol-capped ($C_6SH$, 520 nm) gold MPCs showed weak peaks, but slightly more pronounced for the short-thiol, compared with the longer counterparts.

The TEM micrographs of the alkylthiol-capped gold MPCs are presented in Figure 2.16A1, B1 and C1. Particle size analysis from the TEM yielded generally small diameters; with the hexanethiol-capped MPCs showing an average particle size of 5.6 ± 2.4 nm, this was comparable with the octanethiol-capped MPCs with an average

size of 5.2 ± 1.8 nm. As for the dodecanethiol-capped gold MPCs, the average particle diameter was 4.3 ± 1.1 nm. These findings are in line with the observed absorption patterns.

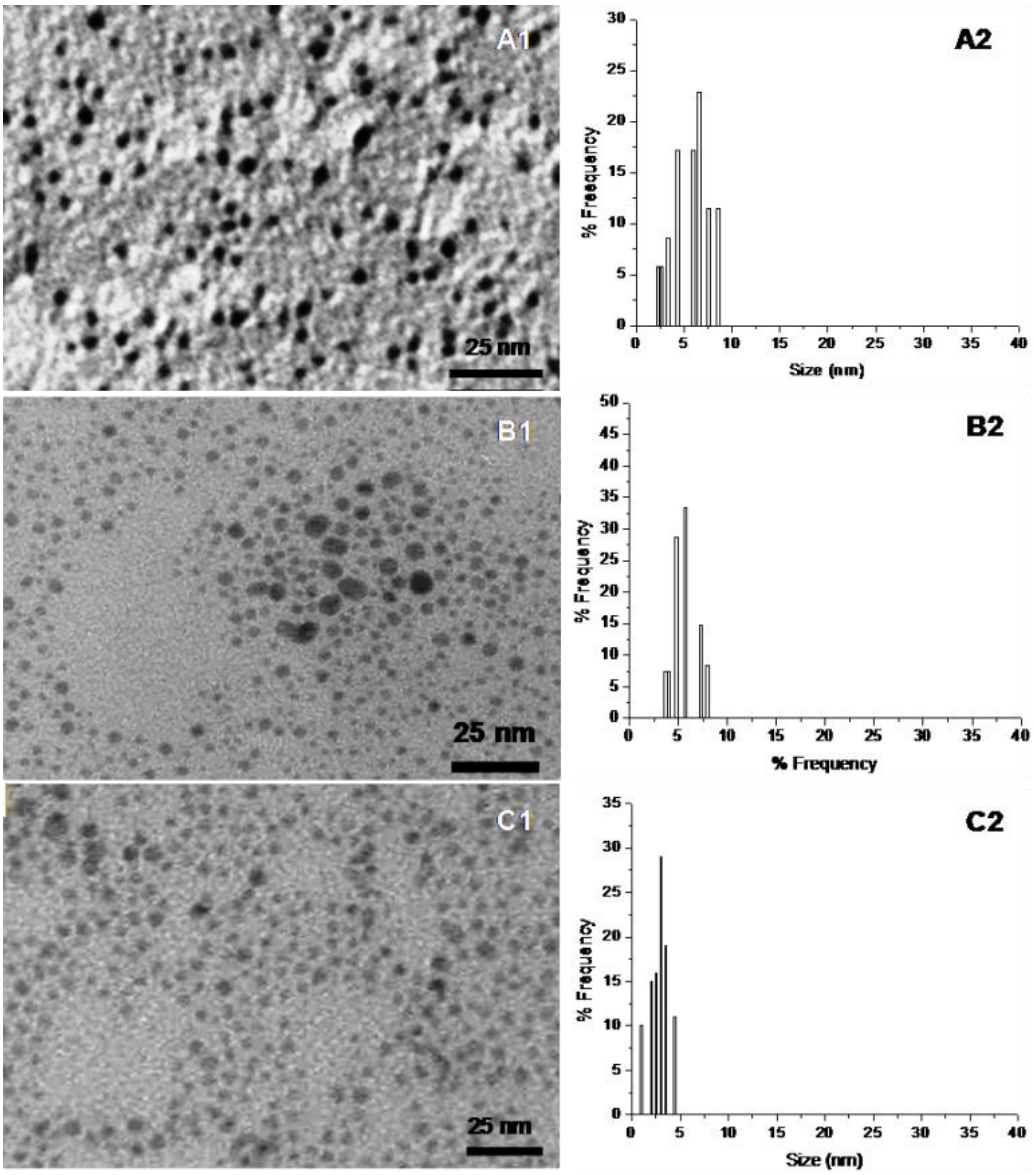


Figure 2.16. *TEM micrographs of the alkylthiol-capped gold MPCs, hexanethiol (A1), octanethiol (B1) and dodecanethiol; and the corresponding size distribution quantifications, for hexanethiol- (A2), octanethiol- (B2) and dodecanethiol-capped gold MPCs.*

A general comparison among these nanoparticles showed that the longer chain alkythiol ligand yielded smaller MPCs that were also more monodispersed. Such an observation can be attributed to the steric bulkiness of the dodecanethiol, which allowed limited or no immediate interactions among the growing particle nuclei. These MPCs have remarkable stability, lasting for periods of months without any obvious signs of decomposition or irreversible aggregation [42]. Moreover they could be dried into powders and can thus be handled as simple chemicals with the ability of being redissolved in nonpolar solvents such as toluene.

## 2.5. SUMMARY AND CONCLUSIONS

In this chapter, the aqueous and non-aqueous synthesis of colloidal gold nanoparticles and MPCs using different synthetic protocols and capping agents was investigated. The particle dispersity, sizes, morphologies and growth patterns were explored by the use of different functionalised ligands. In the Turkevitch protocol, the average particle sizes were shown to be affected by the ratio of the gold salt-to-citrate ratio in solution. To a lesser extent, the shapes of the particles were also controllable in the same manner, with relatively monodisperse spheres dominating at higher citrate amounts and low aspect ratio rod-like particles with poor dispersity found at low citrate amounts.

It can be seen that the size of the particle surface charge, a function of the citrate ions on the nanoparticle surface, controls the electrostatic energy barrier between the particles and therefore modulates the likelihood that the nanoparticles will interact. The introduction of secondary functionalities was achieved by the use of bifunctional ligands, providing simple handles to attach further biomolecular moieties or for creation of self-assembled structures on the surfaces of the MPCs. The introduction of a carboxylic functional group was achieved using the 3-thiopheneacetic acid; this caused the particles to interact resulting in an atypical semi-linear growth pattern.

Simultaneous introduction of a double functionality ($-NH_2$ and -OH) was evaluated in the use of 4-aminothiophenol though this showed a high propensity for aggregation, the MPCs were dispersible in acidic solutions. Uncontrolled aggregation was observed in the use of 2-mercaptoethanol, which can also be attributed to the short alkyl spacer that cannot impose the necessary barrier among interacting MPCs. The direct

attachment of biologically important molecules, L-cysteine and L-glutathione represents a facile means of introducing bioactive molecules onto the MPCs. Not only can these particle-embedded biomolecules be useful for their functions, but other biomolecules can be anchored on them using standard protocols.

The synthesis in non-polar solvents was achieved by following the Brust two-phase protocol. For the three alkylthiols employed as capping agents, hexanethiol, octanethiol and dodecanethiol, it was observed that the resultant particle sizes and their dispersion were governed by the ligand chain lengths. The longer chain (dodecanethiol) gave in smaller more monodispersed MPCs. This can be correlated to the steric bulkiness of the ligand that forms an effective shell around the MPCs.

## 2.6. REFERENCES


1. Daniel C.-M. and Astruc D., *Chem. Rev*., 2004, **104**, 293.
2. Green M., *Angew. Chemie Int. Ed*., 2004, **43**, 4129.
3. Niemeyer C.M., *Angew. Chem. Int. Ed*., 2001, **40**, 4128.
4. Katz E. and Willner I., *Angew. Chem. Int. Ed*., 2004, **43**, 6042.
5. Tshikhudo T.R., Wang Z. and Brust M., *Mater. Sci. and Technol*., 2004, **20**, 980.
6. (a) Sosibo N.M. and Revaprasadu N., *Mater. Sci. Eng. B*, 2008, **150** (2), 111; (b) Mdluli P.S. and Revaprasadu N., *J. Alloys Comp*., 2008, in press; (c) Chili M.M. and Revaprasadu N., *Mater. Lett*., 2008, **62** (23), 3896.
7. Turkevitch J., Stevenson P.C. and Hillie J., *Discuss. Faraday Soc*., 1951, **11**, 55.
8. Brust M., Walker M., Bethell D., Schiffrin J. and Whyman R., *Chem. Commun*., 1994, 801.
9. Mann S.A., Davis S.A., Hall S.R., Li M., Rhodes K.H., Shenton W., Vaucher S. and Zhang B., *J. Chem. Soc., Dalton Trans*., 2000, 3753.
10. Davis S.A., Breulmann M., Rhodes K.H., Zhang B. and Mann S., *Chem. Mater*., 2001, **13**, 3218.
11. Giersig M. and Mulvaney P., *Langmuir* 1993, **9**, 3408.
12. Nuzzo R.G. and Allara D.L., *J. Am. Chem. Soc*., 1983, 105, 4481; Ulman A., *Chem. Rev.*, 1996, **96**, 1533.

13. Love J.C., Estroff L.A., Kriebel J.K., Nuzzo R.G. and Whitesides G.M., *Chem. Rev*., 2005, **105**, 1103.
14. Whetten R.L. and Price R.C., *Science*, 2007, **318**, 407.
15. Jadzinsky P.D., Calero G., Ackerman C.J., Bushnell D.A. and Kornberg R.D., *Science*, 2007, **318**, 430.
16. Billinge S.J.L. and Levin I., *Science*, 2007, **316**, 561.
17. Badia A., Demers L., Dickinson L., Morin F.G., Lennox R.B. and Raven L., *J. Am. Chem. Soc*., 1997, **119**, 11104.
18. Templeton A.C., Wuelfing W.P. and Murray R.W., *Acc. Chem. Res*., 2000, **33**, 27.
19. Nuzzo R.G., Zegarski B.R. and Dubois L.H., *J. Am. Chem. Soc*., 1987, **109**, 733.
20. Lee J.-G., Lee J. and Yates J.T. Jr, *J. Am. Chem. Soc*., 2004, **126**, 440.
21. Hassan M., Bethell D. and Brust M.; *J. Am. Chem. Soc*., 2002, **124** (7), 1132.
22. Han G., Chari N.S., Verma A., Hong R., Martin C.T. and Rotello V.M., *Bioconjugate Chem.*, 2005, **16**, 1356.
23. Peng B.-K., elin H.I., Chong J.-X., Ji W., Trout B.L. and Lee J.-Y., *J. Phys. Chem. C*, 2007, **111**, 6281.
24. Liz-Marzan L.M., *Langmuir*, 2006, **22** (1), 32.
25. Papavassiliou G.C., *Prog. Solid State Chem*., 1979, **12**, 185.
26. Mulvaney P., Langmuir, 1996, **12**, 788.
27. Eustis S and M. El-Sayed M., *Chem. Soc. Rev*., 2006, **35**, 209.
28. Englebienne P., Weiland M., *Chem. Commun*., 1996, 1651.
29. Huang H. and Yanga X., Colloids *and Surfaces A: Physicochem. Eng. Aspects*, 2005, **255**, 11.
30. Huang, X. Sun, X. Jiang, S. Dong an E. Wang, *Macromol. Rapid Commun*., 2003, **24**, 1024.
31. Hu X., Cheng W., Wang T.and S. Dong, *Nanotechnology*, 2005, **16**, 2164.
32. Thomas M. and Klibanov A.M., *Proc. Natl. Acad*. Sci. U.S.A., 2003, **100**(16), 9138.
33. Fei S.F., Chen J., Yao S., Deng G., He D. and Kuang Y., *Anal. Biochem*., 2005, **339** (1), 29.
34. Tengvall P., Lestelius M., Liedberg B. and Lundstroem I., *Langmuir*, 1992, **8**(5), 236.

35. Willner I., Katz E., Willner B., Blonder R., Hele-Shabtai V. and Buckmann A.F., *Biosens. Bioelectron.*, 1997, **12**, 337.
36. Salvakannan PR., Mandal S., Phadtare S., Gole A., Pasricha R., Adyamathaya S.D. and Sastry M., *J. Colloids Interf. Sci*., 2004, **269**, 97.
37. Oakley A.J., *Curr. Opin. Struc. Biol.*, 2005, **15**, 716.
38. Schaaff T.G., Knight G., Shafigullin M.N., Borkman R.F. and Whetten R.L., *J. Phys. Chem. B*, 1999, **102**, 10643.
39. Vezmar I., Alvarez M.M., Khoury J.T., Salisbury B.E., Shafigullin M.N. and Whetten R.L., *Z Phys. D Atom Mol. Cl*., 1997, 40, 147.
40. Underwood S. and Mulvaney P., *Langmuir*, 1994, **10**, 3427.
41. Hostetler M.J., Wingate J.E., Zhong C.-J., Harris J.E., Vachet R.W., Clark M.R., Londono J.D., Green S.J., Stokes J.J., Wignall G.D., Glish G.L., Porter M.D., Evans N.D. and Murray R.W., *Langmuir*, 1998, **14**, 17.
42. Bethell D., Brust M. and Kiely C., *J. Electroanal. Chem*., 1996, **409**, 137.

# CHAPTER 3: SYNTHESIS OF GOLD MONOLAYER PROTECTED CLUSTERS AND THEIR BIOMOLECULAR FUNCTIONALISATION

## 3.1. INTRODUCTION

Protocols for the preparation of both hydrophobic and hydrophilic gold and other noble metal monolayer protected clusters (MPCs) have been developed over the years [1-6]. The sensitivity of the surface plasmon resonance (SPR) of these materials to their environment changes, renders them responsive optical detection tools for monitoring and identifying bio-recognition events [7]. The size similarity of MPCs and biological molecules such as proteins, nucleic acids and other intracellular components has led to a vast number of their applications in biology, including bio-diagnostics and targeted drug delivery [8]. Robust multifunctional MPCs containing specific targeting ligands are essential tools needed to address various biological applications.

The synthesis of highly stable alkanethiolate-passivated gold MPCs by Brust and co-workers presented a simplified reproducible route for the production of small core gold clusters [1]. These MPCs displayed air stability, were isolable and could be dried and handled as simple powdered chemicals; they could be re-dissolved in nonpolar solvents without any irreversible aggregation or decomposition. The incorporation of the PEG-SH by Wuelfing *et al.* via the ligand place-exchange reaction endowed the MPCs with stability, water solubility and thus expanded potential applications in life sciences [9]. A development to this method allowing for further immobilisation of biomolecules was the incorporation of multivalent functionality to the MPCs by the use of hetero-bifunctional PEG-SH ligands by Foos *et al.* [10]. The use of mixed PEG-SH functionalities (MMPCs) on the same gold core facilitates the immobilisation of different possible biomolecules [11].

### 3.1.1. Chapter Strategy

A series of PEGylated ligands were employed in the fabrication of the gold monolayer protected clusters as graphically illustrated in Figure 3.1 and charted in Table 3.1. The

approach used for the synthesis and biofunctionalisation techniques are briefly introduced in the next four sub-sections.

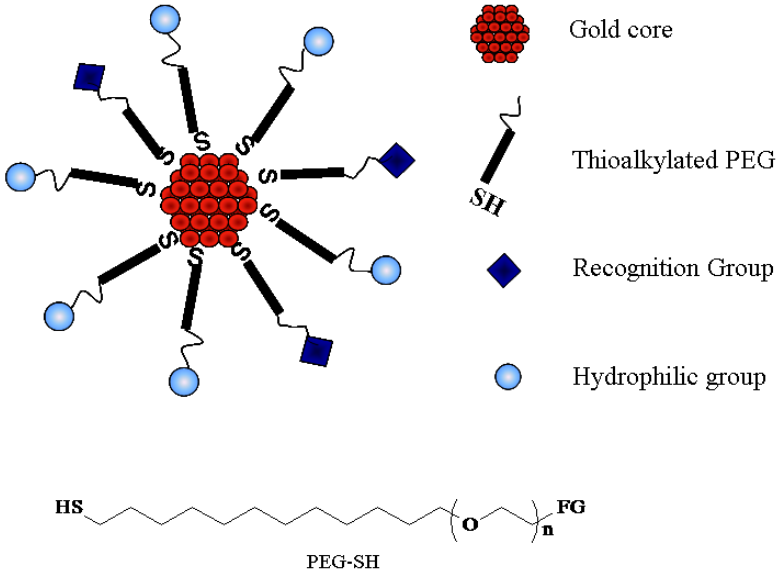


Figure 3.1. *A generic design of functional PEGylated AuMPCs.*

Table 3.1. PEGylated ligands for the synthesis of gold monolayer protected clusters.

| | FG | Abbreviation | *n* |
|---|---|---|---|
| **1** | OH | PEG-OH | 4 |
| **2** | $OCH_2$-COOH | PEG-COOH | 6 |
| **3** | Biotin | PEG-biotin | 3 |
| **4** | $N(COOH)_3$ | PEG-NTA | 3 |

### *3.1.1.1. Surface PEGylation: MPC Synthesis*

Strategies for the incorporation of various PEGylated ligands offering stabilisation of gold nanoparticles are presented. These MPCs serve as molecular handles for the attachment of various biomolecules onto the MPC surface using different protocols. The incorporation of monofunctional ω-functionalised PEG-SH (OH and COOH) on the surface of the nanoparticles has been achieved by the ligand place-exchange reaction or direct reduction synthesis, resulting in the covalent attachment of the PEG-SH ligand on the gold core surface [12-14]. The ligand place-exchange strategy will be presented here.

#### *3.1.1.2. Carbodiimide Coupling Strategy*

This process involves the activation of the carboxylic end group by the N-(3-dimethylaminopropyl)-N´-ethylcarbodiimide hydrochloride (EDC) in the presence of *N*-hydroxysuccinimide (NHS). The NHS functions to improve the carbodiimide-mediated amide-forming reaction by producing hydrolysis-resistant active ester reaction intermediates [15]. The NHS can therefore be regarded as a catalyst required for an effective biomolecular conjugation through the amide bond formation by the carbodiimide through the activation of the carboxyl group [16].

#### *3.1.1.3. Biofunctionalisation via the biotin-avidin-biotin (BAB) Protocol*

The streptavidin-biotin interaction is a well-known phenomenon and has been applied in many areas, from competitive binding assays to commercial diagnostics [17] Streptavidin, a crystalline protein isolated from culture broth of *Streptomyces avidinii*, is a tryptophan-rich protein possessing no carbohydrates and having a pI value of 5-6 [18]. The low pI value of streptavidin can be credited with the low nonspecific binding of streptavidin at common working pH ranges. The four binding sites for biotin have been suggested to occur at specific groups in the protein that show some structural relationship to the cyclic ureido group of biotin, giving optimal van der Waals contacts [18]. Crystallographic analyses suggests that this binding site, in addition to structural complementarity to biotin, has a network of hydrogen bonds that form a rigid lattice when the biotin molecule docks into the site [19].

#### *3.1.1.4. Hexahistidine-tagged Protein Immobilisation*

The affinity of specifically-tagged biomolecules for metal chelated solid resins has long been exploited in metal ion-affinity chromatography (IMAC) [20]. The improvement in the selection of chelating agents and the ability to engineer specific tags has given a boost in the development of such protocols for protein purification in areas such as proteomics [21]. Among these protocols is the chelating moiety nitrilotriacetic acid (NTA) chelated with a bivalent cationic $Ni^{2+}$ ion (Ni-NTA-conjugate) for the specific attachment of hexahistidine-tagged (6xHis) recombinant proteins [22]. The chelation of the

quadridentate NTA with the $Ni^{2+}$ possessing a coordination number of six, allowing two vacant attachment positions on the $Ni^{2+}$ for the incoming 6xHis-tagged biomolecule [23]. The Ni-NTA resins have been shown to have an affinity as high as $K_D \approx 10^{-13}$ for the 6xHis-tagged proteins, allowing for simple purification by washing with either highly salty (≤1 M), organic (ethanol or glycerol ≤30%), non-ionic detergents (Tween 20 ≤1%) or reducing agents (β-mercaptoethanol ≤1 mM) without reversing the process when immobilisation experiments are conducted [24].

## 3.2. EXPERIMENTAL MATERIALS AND METHODS

### 3.2.1. Materials

Phosphate buffered saline (Sigma-Aldrich), N-(3-dimethylaminopropyl)-N´-ethylcarbodiimide hydrochloride (Sigma-Aldrich), TRIS borate-EDTA buffer dry blend (Fluka), N-hydroxysuccinimide, 98% (Sigma-Aldrich), Agarose SFR™, AMRESCO (Sigma-Aldrich), Biotin-TAT (AnaSpec Inc.), FAM-TAT (AnaSpec), Caliber™ glycerol (Sigma-Aldrich), Sephadex G-25, bead diam. 20-50 μm (Sigma-Aldrich), Sephacryl 100-HR (Sigma-Aldrich) and high purity double-distilled water were used in the experiments. All chemicals were ordered from Sigma-Aldrich (Germany) and were used without further purification.

### 3.2.2 Instrumentation

#### *Agarose Gel Electrophoresis*

Agarose gel electrophoresis experiments were conducted using the Centipede™ Wide Gel Electrophoresis System. Typically, the MPCs were supplemented with 1% glycerol (10% v/v of the total MPC volume) and loaded at 10 μL per well of 1% agarose gel. The experiments were run in 1X TBE (0.89M Tris, 0.89M Boric Acid, 0.002M EDTA) at 60V constant voltage for 0.5-2 hours.

#### *Centrifugation*

Samples were centrifuged using the Hettich MIKRO 22R cooling centrifuge. The samples were generally centrifuged in 1.5 mL Eppendorf tubes.

### 3.2.3. Synthesis of Gold Nanoparticles

The syntheses of gold nanoparticles was conducted following the literature protocols and the resultant citrate-capped gold nanoparticles of average size 14 ± 1.3 nm [25] (referred to as 14 nm, SM1) and borohydride-capped gold nanoparticle of average size 5.5 ± 1.6 nm [26] (referred to as 5.5 nm, SM10) were used for various preparations presented next.

### 3.2.4. PEG-OH Gold MPCs

Into the filtered solution of the citrate-capped gold nanoparticles [14 nm] (2 nM, 20 mL), a methanolic solution of PEG-OH (2 mg) was added at room temperature under stirring conditions. The reaction was allowed to proceed for a further three hours and the resultant PEG-OH gold MPCs were centrifuged (22 000 rpm, 20 minutes, 22°C) and washed three times with double distilled water. The MPCs were further purified by running the size-exclusion chromatography column using Sephadex® G-25 as a stationery phase and water as the eluent to produce PEG-OH gold MPCs [ME1]. The functionalisation of smaller particles [5.5 nm] was conducted similarly; starting with the borohydride-capped nanoparticles (30 nM, 20 mL). The purification was conducted through centrifugation (18 000 rpm, 30 minutes, 22 ºC) and the size-selective column was run similar to the procedure used for larger particles to produce smaller PEG-OH gold MPCs [ME2].

### 3.2.5. PEG-COOH Gold MPCs

#### *3.3.5.1. Part I: Synthesis*

Different percentages of PEG-COOH gold MPCs were synthesised co-stabilised with PEG-OH. For 1 % PEG-COOH, two methanolic solutions of PEG-COOH (0.02 mg) and PEG-OH (1.98 mg) were thoroughly mixed by inverting the mixture vigorously several times. The mixture was added into 20 mL of the citrate–capped gold nanoparticles [14 nm] (2 nM) and the mixture was stirred continuously for three hours. The resultant gold MPCs were washed and purified as laid out in section 3.3.4 above to produce ME3A MPCs. Similarly, 10 % (0.2 mg PEG-COOH and 1.80 mg PEG-OH) [ME3B], 50 % (1 mg PEG-COOH and 1 mg PEG-OH) [ME3C] and 100 % PEG-COOH (2 mg) [ME3D] were synthesised and purified following the same experimental procedures. Following a

similar experimental procedure in section 3.3.4 smaller MPCs [5.5 nm] were synthesised and purified, employing 100 % PEG-COOH (2 mg) [ME4] using the borohydride-capped colloidal nanoparticles (30 nM, 20 mL).

#### *3.2.5.2. Part II: Biofunctionalisation with Streptavidin*

Following the synthesis of the different percentages of PEG-COOH-functionalised MPCs; 1 % [M3A, 14 nm] and 10 % [M3B, 14 nm], the carbodiimide coupling of the biotin-binding streptavidin protein was conducted. Aqueous solutions of EDC (0.6 M, 0.3 mmol) and NHS (0.2 M, 0.09 mmol) were mixed into 0.5 mL methanol. The reaction was thoroughly mixed by inverting gently several times, and the solution added into the 1 % PEG-COOH gold MPCs [M3A] (2 nM, 20 mL). The reaction mixture was gently swirled at room temperature for 30 minutes followed by the addition of an aqueous solution of streptavidin (1 μg). The reaction mixture was swirled gently for 5 – 10 minutes. The reaction was allowed to proceed undisturbed for 16 hours at 4 °C [ME5A]. A similar experimental procedure was conducted employing the 10% PEG-COOH MPCs M3B **[**14 nm], using EDC (0.6 M, 0.3 mmol), NHS (0.2 M, 0.09 mmol) and introducing 120 μg of streptavidin. The resultant streptavidin conjugates were washed twice with water through centrifugation (12 000 rpm, 20 minutes, 22 ºC). Further purification was conducted by running the size-exclusion chromatography column using Sephacryl® as the stationery phase and PBS buffer (0.01 M phosphate buffer, 0.0027 M KCl and 0.137 M NaCl) as the eluent [ME5B].

### 3.2.6. PEG-biotin MPCs

#### *3.2.6.1. Part I: Synthesis*

PEG-biotin gold MPCs were synthesised in varied amounts (1 % and 10 %), and the co-stabilised with PEG-OH. Into 20 mL of citrate-capped nanoparticles [14 nm, 2 nM], methanolic solutions of PEG-biotin (0.02 mg) and PEG-OH (1.98 mg) were mixed and added simultaneously. The reaction was stirred for a further 3 hours and the resultant 1 % PEG-biotin MPCs were centrifuged (12 000 rpm, 20 minutes, 22 ºC) and washed three times with water [ME6A]. A similar experimental procedure for the synthesis of ME6A was followed as used for the synthesis of 10 % PEG-biotin gold MPCs [ME6B, 14 nm],

1% PEG-biotin [ME7A**,** 5.5 nm] and 10 % PEG-biotin [ME7B, 5.5 nm]. MPCs with smaller sizes were washed three times with water (18 000 rpm, 30 minutes, 22ºC) and purified similarly as done for ME6A.

#### *3.2.6.2. Part II: Biofunctionalisation with Streptavidin*

Following the successful synthesis of PEG-biotin-functionalised gold MPCs [ME6A and ME7A], streptavidin was introduced via the BAB interaction. An aqueous solution of streptavidin (179 μg) was introduced into the concentrated PEG-biotin gold MPCs (800 μL, 16 nM). The volume was made up to 2 mL by adding PBS buffer (0.01 M phosphate buffer, 0.0027 M KCl and 0.137 M NaCl). The reaction mixture was mixed thoroughly by swirling following refrigeration at 4 ºC for 48 hours. Similar washing and purification as used for ME6A was conducted on the resultant conjugates [ME8, 14 nm] and [ME9, 5.5 nm].

#### *3.2.6.3. Part III: Biomolecular Immobilisation with Biotin-TAT*

The immobilisation of the biotinylated cell-penetrating peptide (CPP), TAT was conducted on the streptavidin conjugates, ME8 and ME9. Into the streptavidin conjugate, ME8 (850 μg, 1.5 nM, 14 nm), a PBS (0.01 M phosphate buffer, 0.0027 M KCl and 0.137 M NaCl) solution of biotin-TAT (3.57 μg, 560 nM) was added. The mixture was gently swirled to mix and refrigerated at 4 ºC for 48 hours. The resultant TAT bioconjugates were washed with water through centrifugation (12 000 rpm, 20 minutes, 22 ºC) [ME10, 14 nm]. A similar treatment was conducted on the streptavidin conjugate ME8 [5.5 nm] (30 nM) yielding the smaller TAT bioconjugates ME11 [5.5 nm] that were washed correspondingly (18 000 rpm, 20 minutes, 22 ºC). Both the TAT conjugates were purified following similar procedures as ME6A.

#### *3.2.6.4. Part IV: Biomolecular Immobilisation with FAM-TAT*

The introduction of the fluorescent-marked TAT peptide was conducted on the streptavidin conjugates ME8 [14 nm] (1.5 nM) and ME9 [5.5 nm] (30 nM) using similar carbodiimide coupling experimental procedures as used for ME5A to synthesise and purify the FAM-TAT conjugates, ME12 [14 nm] and ME13 [5.5 nm]. The reactant

quantities used were EDC (0.6 M, 0.3 mmol), NHS (0.2 M, 0.09 mmol), and aqueous solution of FAM-TAT (4 μg) peptide.

### 3.2.7. PEG-NTA Gold MPCs

#### *3.2.7.1. Part I: Synthesis*

A 20 mL solution of citrate-capped colloidal gold nanoparticles (2 nM) was used to conduct a similar experimental procedure as used for ME3A for different percentages of PEG-NTA MPCs co-stabilised with PEG-OH. For ME14A (14 nm), PEG-NTA (0.02 g) and PEG-OH (1.98 g) were used. Similarly 10% PEG-NTA (0.2 PEG-NTA and 1.8 mg PEG-OH) [ME14B] (14 nm) and 50% PEG-NTA (1 mg PEG-NTA and 1 mg PEG-OH) [ME14C] (14 nm) were synthesised. This method was further extended to PEG-COOH co-stabilised PEG-NTA gold MPCs, using reactant quantities of 0.02 mg PEG-NTA and 1.98 mg PEG-COOH for ME15A (1%, 14 nm), 0.2 mg PEG-NTA and 1.8 mg PEG-COOH for ME15B (10%, 14 nm) and 1 mg PEG-NTA and 1 mg PEG-COOH for ME15C (50%, 14 nm). Smaller gold core PEG-NTA MPCs, 1% [M16A, 5.5 nm] and 50% [M16B, 5.5 nm] PEG-NTA MPCs co-stabilised with PEG-OH using the borohydride-capped colloidal nanoparticles (30 nM, 20 mL) were synthesised following the same experimental procedure.

#### *3.2.7.2. Part II: Synthesis of PEG-NTA-Ni Conjugates*

Following the successful synthesis and purification of 1% PEG-NTA gold MPCs [ME14A] (16 nM, 1 mL), PEG-NTA-Ni gold conjugates were synthesised by reacting 1 mL of the 1% PEG-NTA gold MPCs with an excess of $NiCl_2.6H_2O$ (65 μmol). After the addition of the nickel salt, the solution was swirled and allowed to react for a further three hour at room temeperature. The resultant conjugate was washed with water through centrifugation three times (10 000 rpm, 10 minutes, 22°C), made up to 1 mL with water and stored at room temperature until further use [ME17, 14 nm].

#### *3.2.7.3. Part III: Immobilisation of Hexahistidine-Tagged MAP kinase*

The N-terminal histidine-tagged MAP kinase was introduced onto the surface of the PEG-NTA-Ni conjugates ME17 (14 nm) by exploiting the high affinity binding of the

histidine-tag onto the $Ni^{2+}$ chelate. An experimental procedure similar to that used for ME10 was conducted using 200 nmol of MAP kinase protein and PEG-NTA-Ni (ME17) conjugate (1.2 nM, 1 mL) both dissolved in PBS (0.01 M phosphate buffer, 0.0027 M KCl and 0.137 M NaCl) followed by washing with water and purification.

### 3.3. RESULTS AND DISCUSSION

For reference, the sample codes are presented in Table 3.2 along with their functionalities.

Table 3.2. Sample codes and their short descriptions.

| SAMPLE CODE | Au CORE SIZE | SURFACE FUNCTIONALITIES | STARTING MATERIAL |
|---|---|---|---|
| ME1 | 14 nm | 100% PEG-OH | Citrate NPs |
| ME2 | 5.5 nm | 100% PEG-OH | Borohydride NPs |
| ME3A, B and C | 14 nm | 1, 10, 50% PEG-COOH (PEG-OH costabilised) | Citrate NPs |
| ME4 | 5.5 nm | 100% PEG-COOH | Borohydride NPs |
| ME5A and B | 14 nm | Streptavidin immobilised via EDC/NHS protocol | ME3A and ME3B |
| ME6A and B | 14 nm | 1, 10% PEG-biotin (PEG-OH costabilised) | Citrate NPs |
| ME7A and B | 5.5 nm | 1, 10% PEG-biotin (PEG-OH costabilised) | Citrate NPs |
| ME8 | 14 nm | Streptavidin immobilised via biotin interactions | ME6A |
| ME9 | 5.5 nm | Streptavidin immobilised via biotin interactions | ME7A |
| ME10 | 14 nm | Biotin-TAT immobilised via biotin-(strept)avidin (BAB) route | ME6A |

| | | | |
|---|---|---|---|
| ME11 | 5.5 nm | Biotin-TAT immobilised via the BAB route | ME7A |
| ME12 | 14 nm | FAM-TAT immobilised via the EDC/NHS protocol | ME6A |
| ME13 | 5.5 nm | FAM-TAT immobilised via the EDC/NHS protocol | ME7A |
| ME14A, B and C | 14 nm | 1, 10, 50% PEG-NTA (PEG-OH costabilised) | Citrate NPs |
| ME15A, B and C | 14 nm | 1, 10, 50% PEG-NTA (PEG-COOH costabilised) | Citrate NPs |
| ME16A and B | 5.5 nm | 1, 50% PEG-NTA (PEG-OH costabilised) | Borohydride NPs |
| ME17 | 14 nm | PEG-NTA-Ni Conjugates | ME14A |
| ME8 | 14 nm | PEG-NTA-Ni-MAP Kinase bioconjugate | ME17 |

### 3.3.1. PEG-OH Gold MPCs: Synthesis and Characterisation

The synthesis of PEG-OH gold MPCs occurred via the ligand place-exchange reaction of the labile citrate ligand [14 nm] and the loosely bound borohydride anions of the smaller sized nanoparticles [5.5 nm]. On addition of the PEG-OH into the nanoparticles, the colour changed from red to purple-red signifying the attachment of the sulphur headgroup on the surface of the nanoparticles. Such a process occurred immediately on addition, signifying the effectiveness of the capping by PEG-OH ligand. The optical absorption peaks for ME1 [14 nm] and ME2 [5.5 nm] are shown in Figure 3.2A1 and B1. The sharp peaks indicated that the MPCs remained dispersed in solution. From the structural analysis of the MPCs showed no signs of aggregation and were completely soluble in water.

The long chain ($C_{11}$) hydrophobic alkyl imparts stability to the cluster by promoting the S-Au interactions. This effect is expected to decrease with a decrease in spacer length. The MPCs are known to withstand aggregation under extreme pH

conditions, high ionic strength conditions [12-14]. The agarose gel electrophoresis of the PEG-OH functionalised gold MPCs is presented in Figure 3.3.

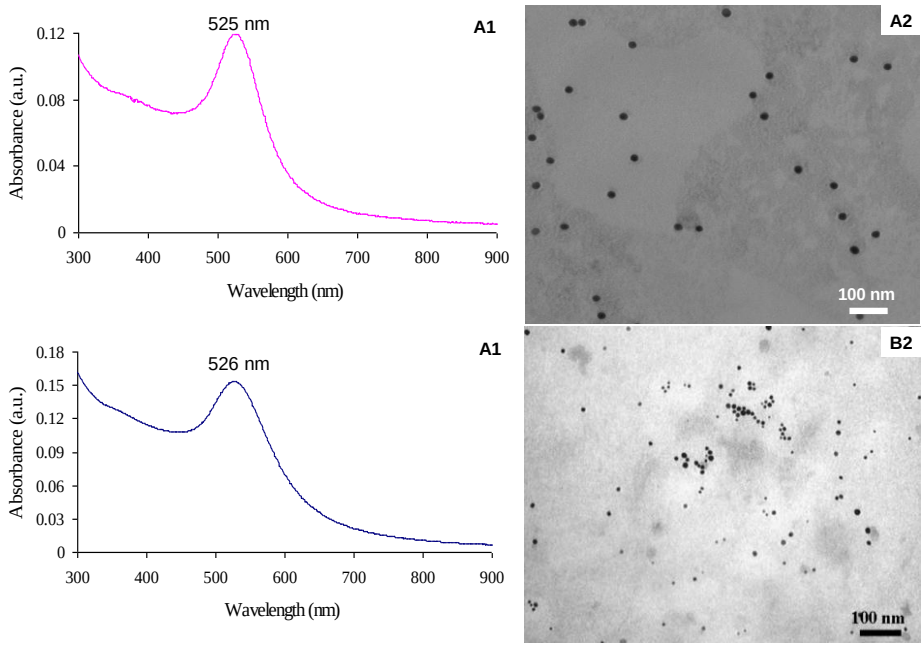


Figure 3.2. *Absorption and structural analysis of the PEG-OH functionalised gold MPCs. UV-Vis absorption spectra (A1) [ME1, 14 nm], (A2) [ME2, 5.5 nm] and TEM micrographs, (B1) [ME1, 14 nm] and (B2) [ME2, 5.5 nm].*

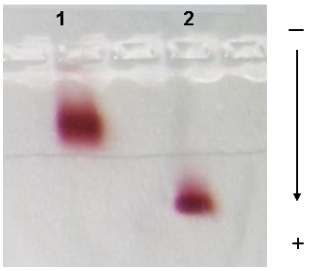


Figure 3.3. *Agarose gel electrophoresis of PEG-OH functionalised AuMPCs; lane 1: ME1 [14 nm] and lane 2: ME2 [5.5 nm].*

The two MPC systems possess similar surface ligands, and thus the change in mobility can be attributed to the gold core size. Clearly, the smaller sized core (ME2**,** lane 2) showed faster mobility towards the anode due to the larger MPCs under the current compared to the bigger counterparts (ME1**,** lane 1). These gold MPCs showed remarkable

stability, showing no signs of aggregation on long term storage. They could also be completely re-dispersed in water after centrifugation during the purification stages.

### 3.3.2. PEG-COOH Gold MPCs: Synthesis and Functionalisation.

***Part I: Synthesis.***

The strategy for the simultaneous introduction of multiple functionalities, -OH and -COOH, on the surface of the gold nanoparticle is illustrated schematically in Figure 3.4. The indication of the attachment of the PEG-SH ligand on the surface of gold was observed in terms of colour changes on the introduction of the ligand.

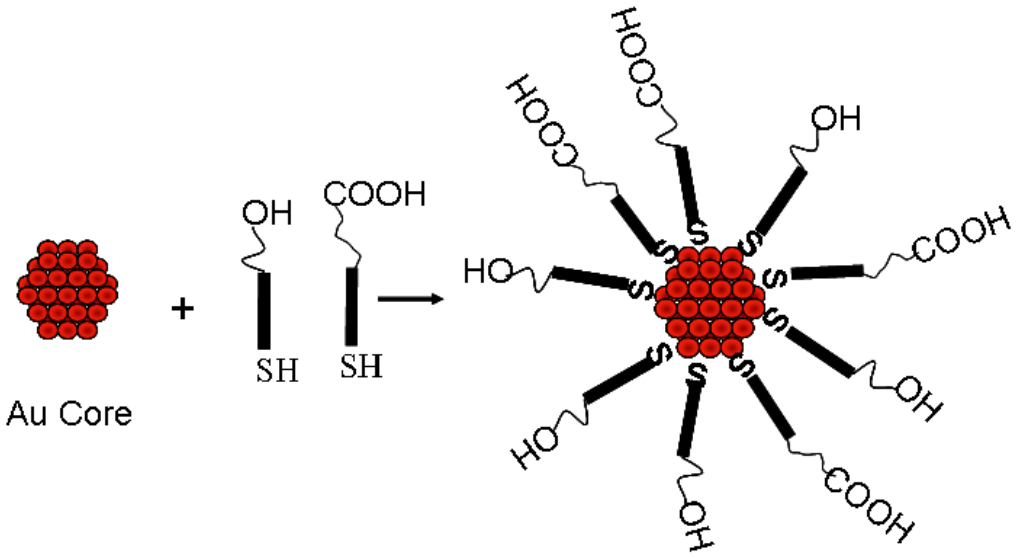


Figure 3.4. *A schematic representation of the simultaneous incorporation of multiple functionalities on the surface of the gold core.*

The resultant multiple functional MPCs represent a unique prospect for the immobilisation of multiple targets on the surface of the gold MPCs. The carboxyl content on the surface of the MPCs could be regulated by variations in the ratios of the ligand mixture. The optical and structural analysis for the synthesis of 1, 10 and 50% PEG-COOH, PEG-OH co-stabilised MPCs is presented in Figure 3.5.

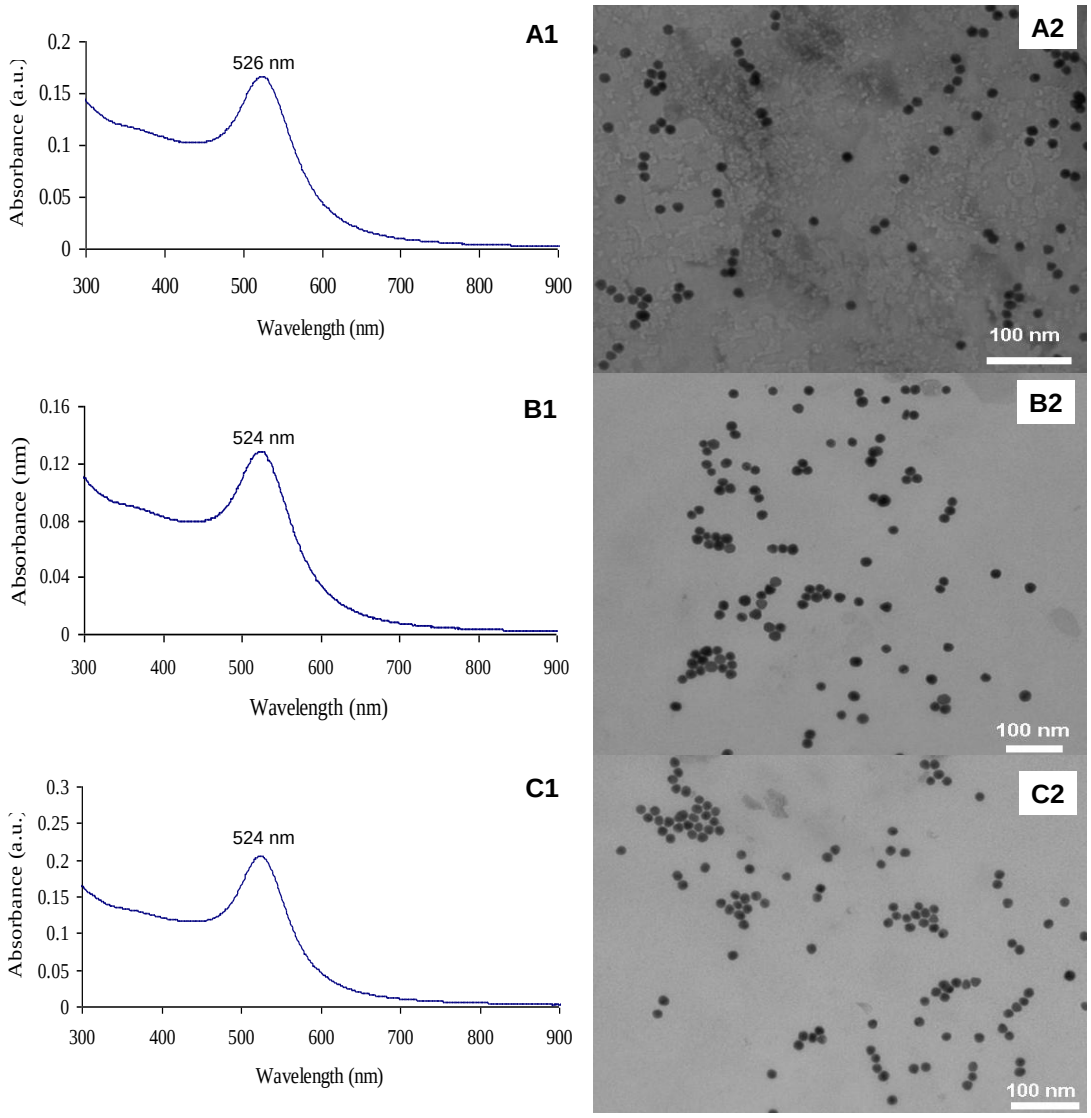


Figure 3.5. *Optical and structural analysis of PEG-COOH and PEG-OH mixed monolayer functionalised gold MPCs; A1) and A2) 1% PEG-COOH [ME3A, 14 nm], B1) and B2) 10% PEG-COOH [ME3B, 14 nm] and C1) and C2) 50% PEG-COOH [ME3C, 14 nm] functionalised MPCs.*

The optical absorption of MPCs containing different percentages of PEG-COOH is presented in Figures 3.5A1 (1%, ME3A), B1 (10%, ME3B) and C1 (50%, ME3C). The sharp peaks indicated that the dispersity of the MPCs was maintained after the incorporation of the ligands on the surface. The high concentration of the PEG-OH on the surface also enhances the stability, and thus limits a large increase in the absorption

wavelengths. The TEM micrographs representing the distribution of the MPCs are presented in Figure 3.5A2 (1%, ME3A), B2 (10%, ME3B) and C2 (50%, ME3C). The increase in the PEG-COOH content showed an onset of the formation of clustered patterns of the nanoparticles, increasing with the increase of the ligand. This can be attributed to the high affinity of the carboxyl group for the gold clusters. The presence of the carboxyl terminal group in many ligands enhances the tendency of ligand intermolecular hydrogen bonding, leading to aggregation and broadening of the SPR absorption peak [32]. Such an effect is however only nominally observed since the bulky PEG imposes a steric barrier on the surface of the gold core. The use of PEG-COOH as a solitary capping agent is presented in Figure 3.6, showing a typical absorption and particle distribution.

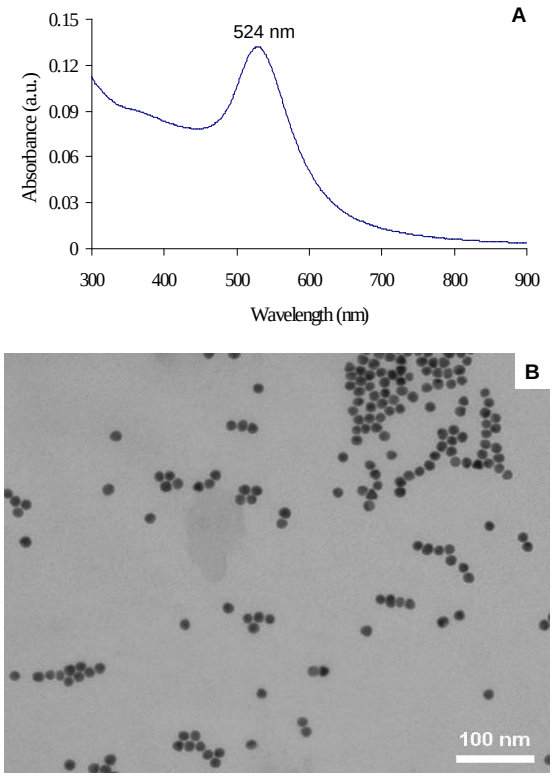


Figure 3.6. *Optical absorption (A) and the EM micrograph (B) of the 100% PEG-COOH functionalised MPCs [ME3D, 14 nm]*.

The assessment of the attachment of the ligand in different proportions was investigated using the horizontal agarose gel electrophoresis presented in Figure 3.7. The differences

in the surface charges relative to the -COOH surface are expected to show different degrees of mobility on the gel.

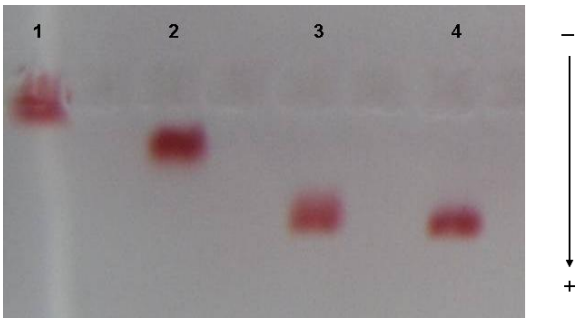


Figure 3.7. *Agarose gel electrophoresis of PEG-COOH functionalised AuMPCs [14 nm] (lanes 1 = 1% (ME3A), 2 = 10% (ME3B), 3= 50% (ME3C) and 4= 100% (ME3D)).*

This trend can be predicted from the differences in dielectric friction of the -OH and -COOH functionalities in solution as the necessary exertion for the orientation of the solvent dipoles in response to the ligand charge under the electromagnetic field. In addition to the dependence of mobility on the charge-to-size ratio, the dissociation constant (pKa), as a measure of the charge distribution, also determines the intrinsic mobility [33]. There was a distinct change in mobility with the increase in the PEG-COOH content on the surface of the MPCs, as shown by the gradual increase in mobilities can be observed from lane 1 (lowest –COOH content, ME3A) through to lane 4 (highest –COOH content, ME3D). These gel electrophoresis results represent a simple yet powerful method for the confirmation of the quantitative and qualitative assaying of the immobilisation of the ligands on the surface of the gold core.

Similarly, PEG-COOH could be used as the only stabilising agent for smaller gold clusters (5.5 nm), as presented in Figure 3.8.

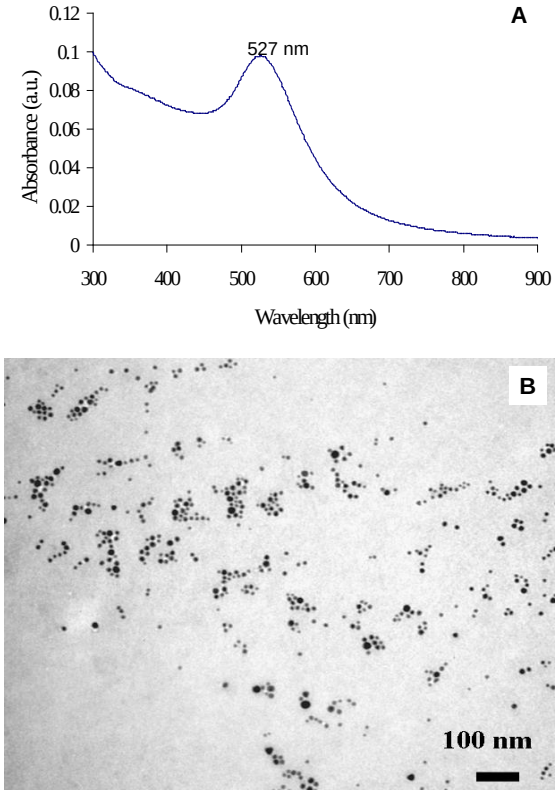


Figure 3.8. *Optical absorption (A) and the TEM micrograph (B) of the 100% PEG-COOH functionalised gold MPCs [ME4, 5.5 nm].*

The successful synthesis of the PEG-COOH MPC systems presented a versatile route for the introduction of further biomolecules using protocols such as carbodiimide coupling.

***Part II: Biofunctionalisation.***

One method for introducing biomolecules onto the surface of MPCs is by the covalent coupling of the carboxylic end of the ligand shell with amine groups of the incoming biomolecule, depicted in Figure 3.9 [34]. The interaction of the -COOH on the surface of the MPCs with the EDC in the presence of NHS yields the ester intermediate. The presence of NHS significantly enhances the coupling efficiency in this reaction. The probability of the hydrolysis of the ester intermediates can be countered by the use of higher molar ratios of the EDC and the immediate conjugation of the protein before the onset of the hydrolysis process. This is then followed by the amine containing biomolecule, which anchors on the MPC through the amide bond.

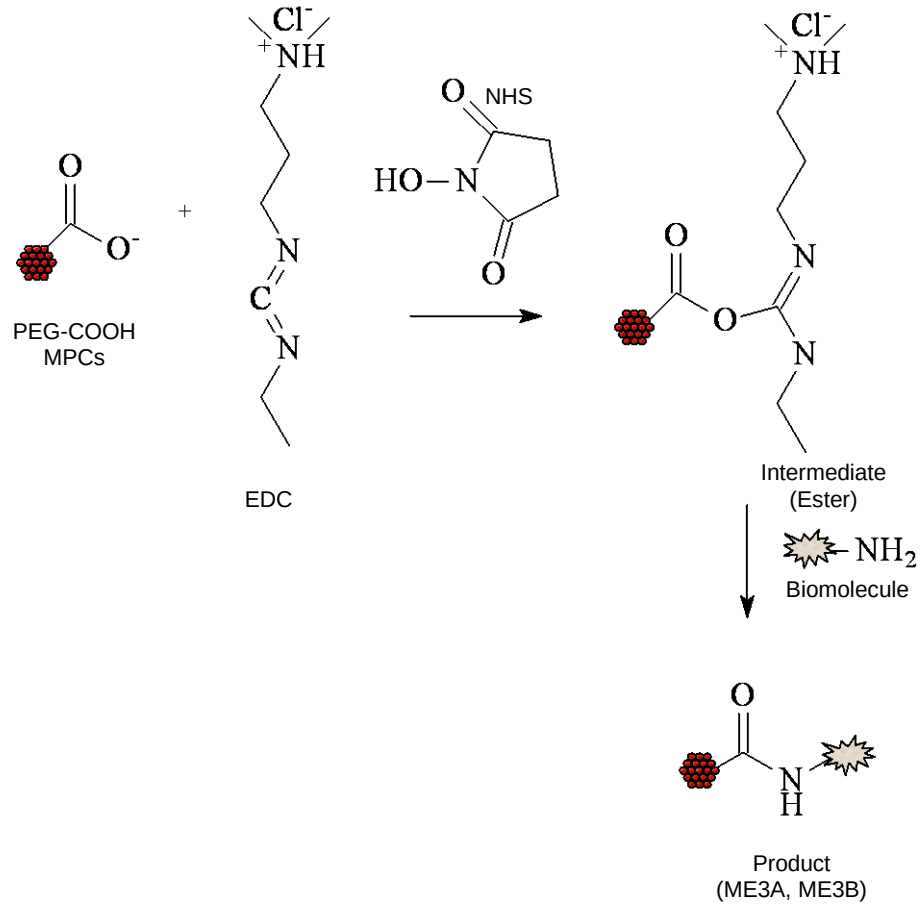


Figure 3.9. *A generic strategy for the introduction of biomolecules by employing the EDC/NHS coupling route.*

Following the addition of the EDC/NHS mixture and reaction with 1% and 10% PEG-COOH gold MPCs [ME3A, 14 nm and MEB, 5.5 nm], the reaction mixture showed a low solubility which was an indication of the formation of the gold MPC-amide ester intermediates. The low solubility demonstrated the resistance of the ester to hydrolysis, limiting any regeneration of the gold PEG-COOH MPCs in solution. The addition of the streptavidin showed a marked improvement in the solubility of the conjugates readily dispersible in solution. The UV-vis measurements and structural analysis is presented in Figure 3.10. The optical absorption of the streptavidin conjugates showed narrow peaks signifying the dispersity of the MPCs. There was no apparent broadening of the spectrum

indicating that there was no aggregation of the MPCs upon the attachment of the streptavidin.

The TEM analysis showed no aggregation of the MPCs on the incorporation of the streptavidin. Coupling of the streptavidin onto the 1% PEG-COOH MPCs showed a lower yields compared to that immobilised on 10% PEG-COOH MPCs signifying the dependence of the attachment on the availability of the –COOH on the MPC surface. More conjugate particles were therefore attained for ME5B, thus the TEM image (Figure 3.10). The attachment of the streptavidin was monitored using agarose gel electrophoresis (Figure 3.11). The migration of the unbound PEG-COOH MPCs was expected to differ from the streptavidin conjugates as a consequence of the presence of the streptavidin on the MPC surface. This was confirmed experimentally, with the streptavidin conjugates, lane 1 (ME5A) showing slower migration speeds compared with the precursor 1% PEG-COOH MPCs (ME3A) in lane 2. This was also observed to be true for the 10% PEG-COOH MPCs (lane 4, ME3B) migrating faster than the corresponding bulky streptavidin conjugates (lane 3, M35B).

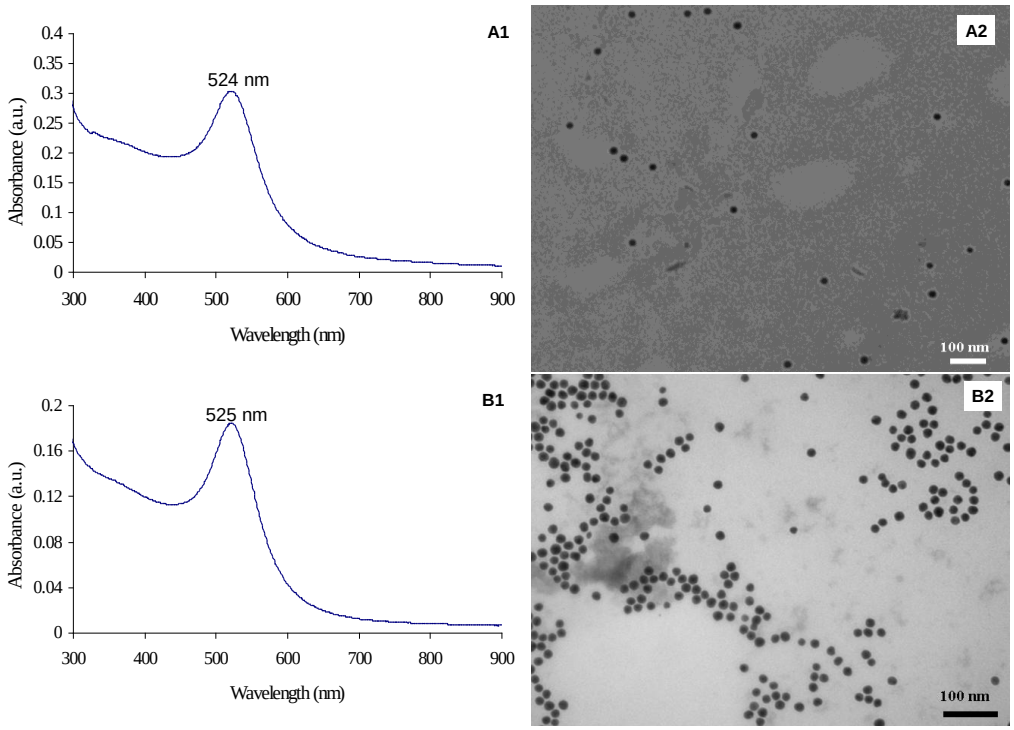


Figure 3.10. *UV-vis optical absorption of the streptavidin conjugates, A1) ME5A, B1) ME5B and the TEM micrographs, A2) ME5A and B2) ME5B.*

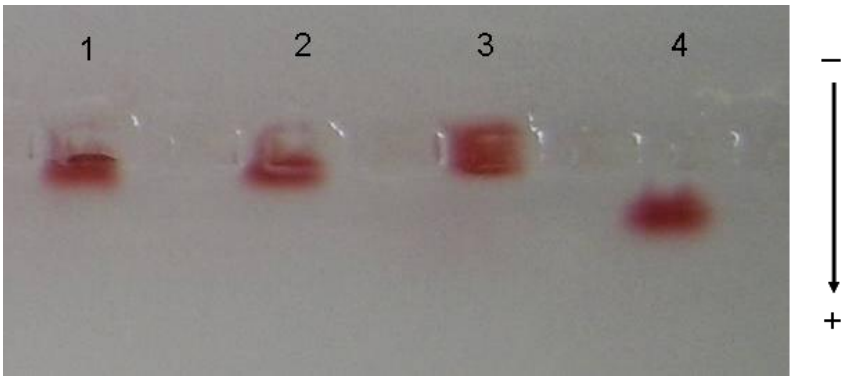


Figure 3.11. *Agarose gel electrophoresis of PEG-COOH functionalised MPCs and the corresponding streptavidin conjugates; lane 1: streptavidin conjugates (ME5A), lane 2: 1% PEG-COOH (ME3A), lane 3: streptavidin conjugates (ME5B) and lane 4: 10% PEG-COOH (ME3B).*

Single migration lines were also observed indicating the homogeneity of the resultant conjugates. The EDC/NHS represents a simple multiple-step introduction of biomolecules to the surface of gold MPCs. The conjugates were stable at 4 °C and dependent on the stability of incorporated protein. Higher storage temperatures are expected to disrupt the function of the biomolecules.

### 3.3.3. PEG-biotin AuMPCs: Synthesis and Biofunctionalisation.

***Part I: Synthesis.***

The introduction of the PEG-biotin on the gold core surface was conducted as depicted in Figure 3.12. This MPC system is amenable to the attachment of streptavidin on the surface. This immobilisation of streptavidin can be achieved through the biotin-streptavidin (BA) interactions on the surface of the gold MPCs.

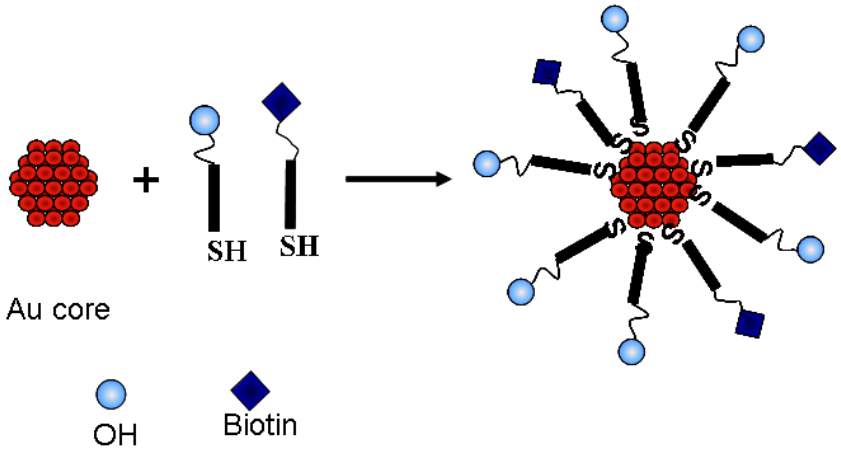


Figure 3.12. *A schematic represnteation of the introduction of PEG-biotin on the gold core.*

Synthesis of 100% PEG-biotin MPCs proved unsuccessful, with particles showing irreversible aggregation and the particles were not redispersible after centrifugation. This can be attributed to the binding of the biotin sulphur group on the MPCs. This was addressed by the use of PEG-OH as the co-stabiliser. This imparted higher hydrophilicity onto the MPCs, this fact emanating from the insolubility of the biotin as a unit.

The optical absorption of both the PEG-biotin MPCs showed plasmon peaks at typical gold absorption ranges, albeit with a slight increase due to the ligand contributions on the surface of the absorbing gold core (Figure 3.13A1 and B1). The absorption peaks were narrow, signifying the retention of dispersity of the MPCs. This was further shown from the TEM measurements depicted in Figure 3.13A2 and B2, with the core size remaining the same as the citrate-capped nanoparticles. The attachment of the PEG-biotin was qualitatively investigated using the agarose gel electrophoresis presented in Figure 3.14. The higher biotin (lane 2, ME6B) loading showed faster migration on the gel.

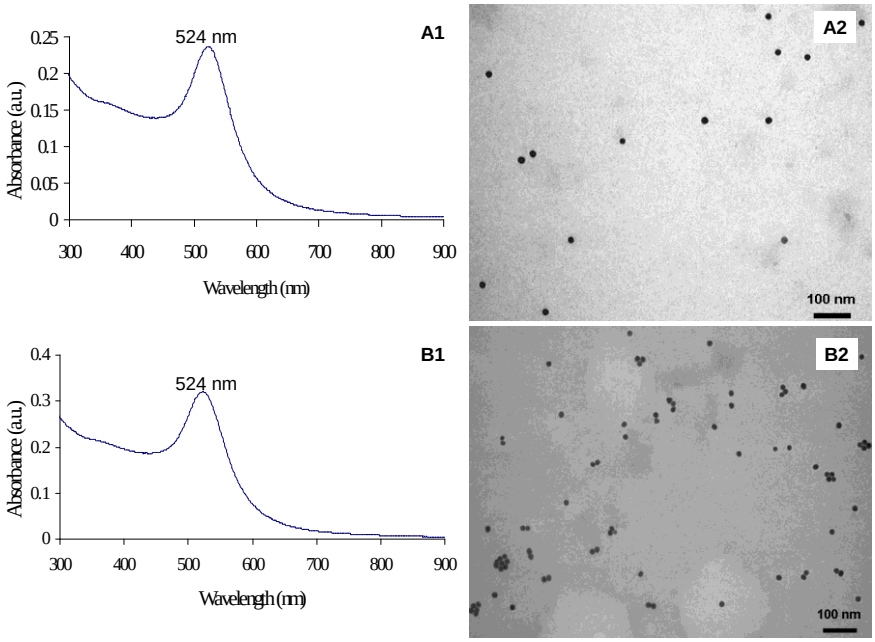


Figure 3.13. *Absorption and structural analysis of PEG-biotin functionalised AuMPCs. A1) and A2) 1% [ME6A,14 nm] and B1) and B2) 10% [ME6B, 14 nm] PEG-biotin MPCs.*

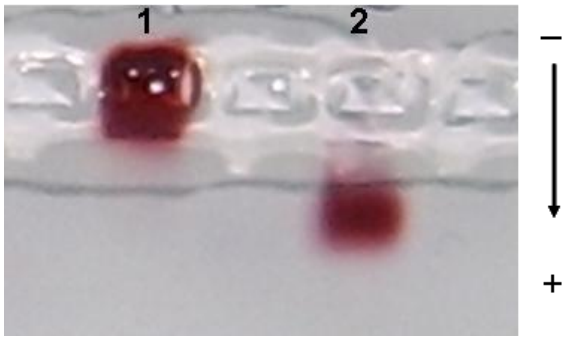


Figure 3.14. *Agarose gel electrophoresis of 14 nm PEG-biotin functionalised AuMPCs; lane 1 = 1% (ME6A) and 2 = 10% (ME6B).*

Similarly, the introduction of PEG-biotin was achieved for the smaller MPCs, depicted in Figure 3.15 and 3.16. Narrow absorption peaks were observed signifying the dispersity of the particles. The agarose gel electrophoresis further proved the attachment of the different PEG-biotin amounts. Lane 1 (1%) showed less mobility compared with the higher PEG-biotin content (lane 2, circled) due to the higher surface negative charge.

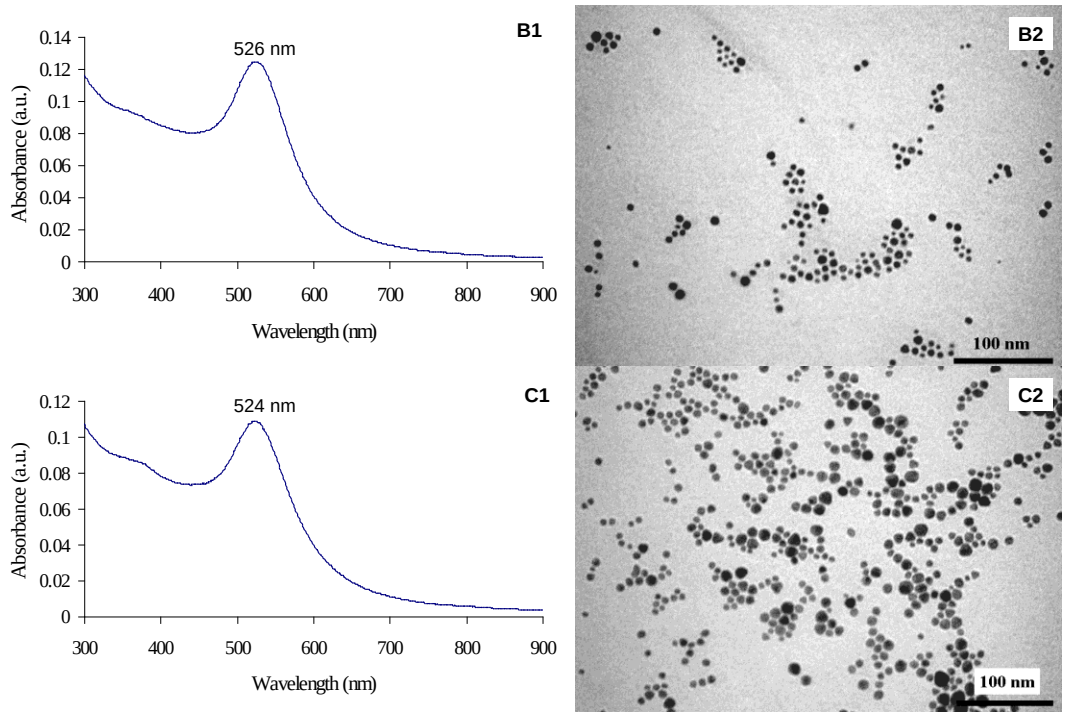


Figure 3.15. *Optical absorption and structural analysis of the 5.5 nm PEG-biotin functionalised AuMPCs. A1) and A2) 1% [ME7A, 5.5 nm] and B1) and B2) 10% [ME7B, 5.5 nm] PEG-biotin MPCs.*

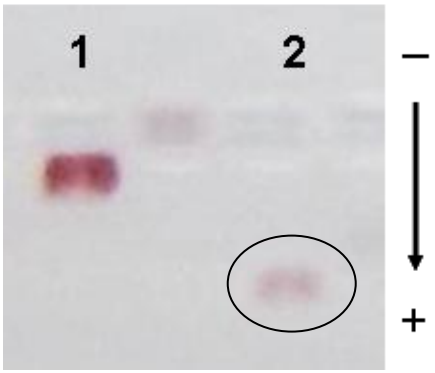


Figure 3.16. *Agarose gel electrophoresis of PEG-biotin gold MPCs; lane 1: 1% (ME7A) and lane 2: 10% PEG-biotin (ME7B).*

These results represent a facile molecular tool for the introduction of streptavidin protein onto the surface of these particles.

***Part II: Biofunctionalisation with Streptavidin.***

Streptavidin binds four moles of biotin per one mole of the protein corresponding to 16.5-18 mg of biotin bound per gram of streptavidin [35] (Figure 3.17). The biotin-binding sites in streptavidin are known to be "buried", as indicated by 1 to 4 in Figure 3.17 and therefore long-chain biotinylation reagents are required for such immobilisation [36]. A one-step facile introduction of streptavidin onto the MPCs is depicted in Figure 3.18.

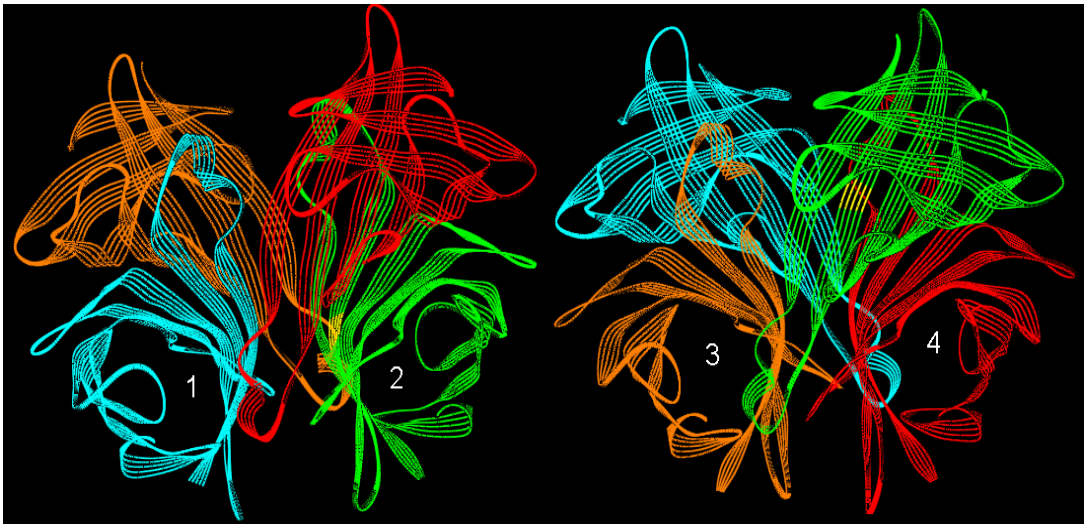


Figure 3.17. *The streptavidin molecule (Protein Data Bank code 1SWE), showing the four biotin-binding sites [37]. The image was generated using the Accelrys® Discovery Studio Visualizer 2.0, Accelrys Software Inc.*

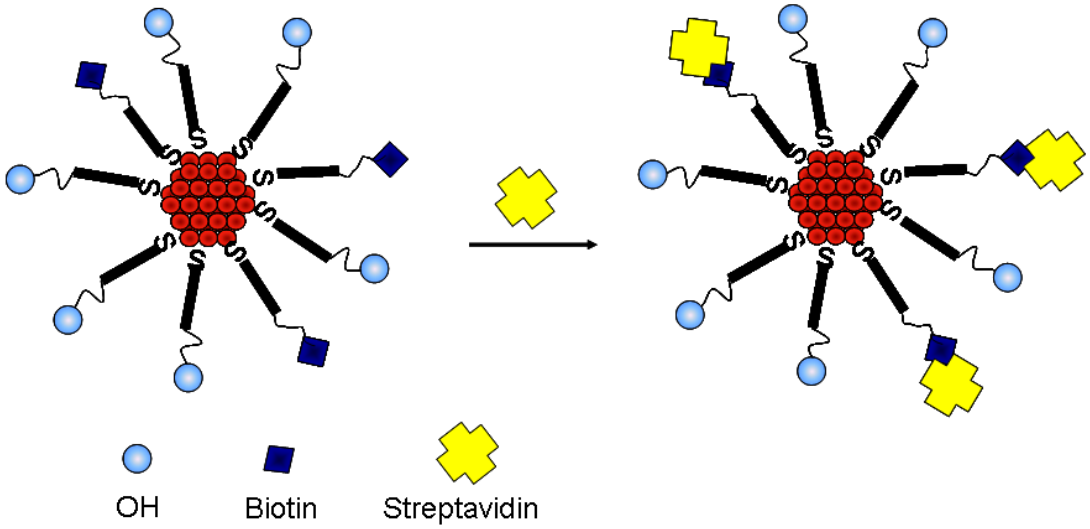


Figure 3.18. *Biomolecular immobilisation of streptavidin onto biotiylated gold MPCs via the biotin-streptavidin interaction.*

Due to the known high affinity of biotin-streptavidin interactions, the effect of collision frequency between the biotinylated gold MPCs and the streptavidin was expected to feature strongly in the final properties of the conjugates. Optical and structural characterisation of the streptavidin conjugates is presented in Figure 3.19.

There was also no broadness of the absorption peak, indicating the preservation of particle dispersity (Figure 3.19A1 and B1). Due to the availability of further biotin-binding sites on the streptavidin, the concentration of the surface biotin on the MPCs as a ratio of the incoming streptavidin proved crucial. An excess of streptavidin was used to saturate all the biotin molecules on the surface of the MPCs and thus minimising the disposition of the conjugates to aggregation. The excess protein was removed during the purification steps to avoid interference during further immobilisation of biomolecules on the streptavidin conjugates.

The particle dispersity was further demonstrated in the TEM measurements (Figure 3.19A2 and B2) of the streptavidin bioconjugates, that showed no aggregation, which would have been as a result of cross-linkages caused by the bioconjugates interacting through the biotin of one MPC and the streptavidin of the second MPC, forming a biotin-avidin-biotin network. A qualitative analysis of the successful

introduction of the streptavidin on the MPCs by 1% agarose gel electrophoresis was conducted (Figure 3.20A (14 nm) and Figure 3.20B (5.5 nm)).

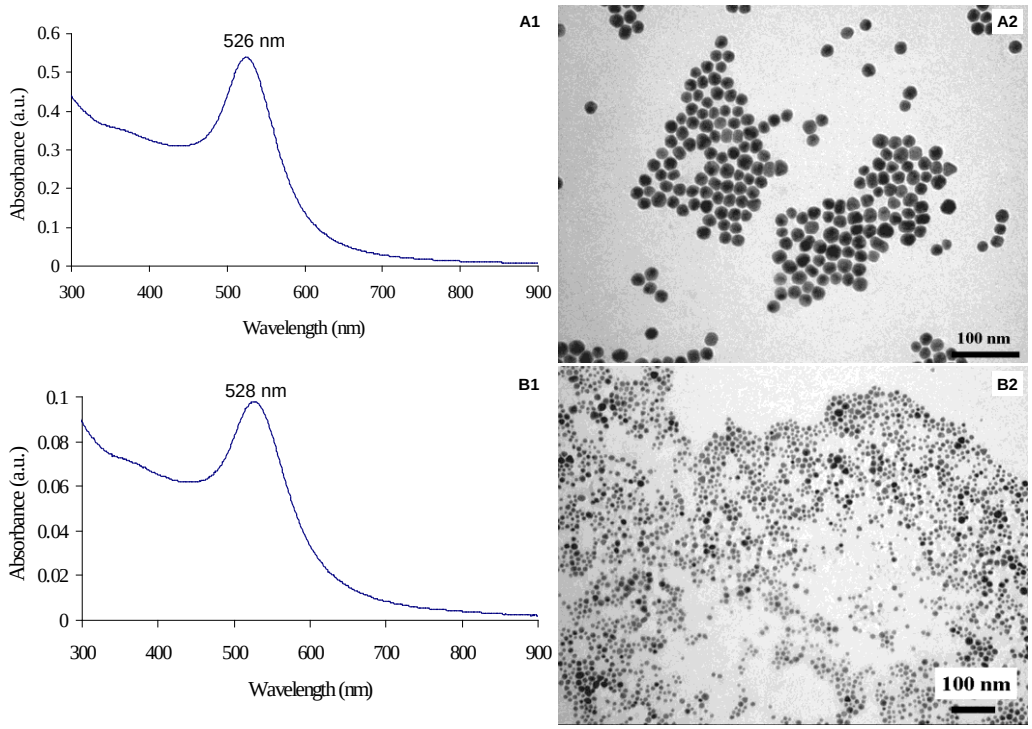


Figure 3.19. *Optical absorption and structural analysis of streptavidin-AuMPC bioconjugates formed through the BA method. A1) and B1) ME8 (14 nm) and B1) and B2) ME9 (5.5 nm).*

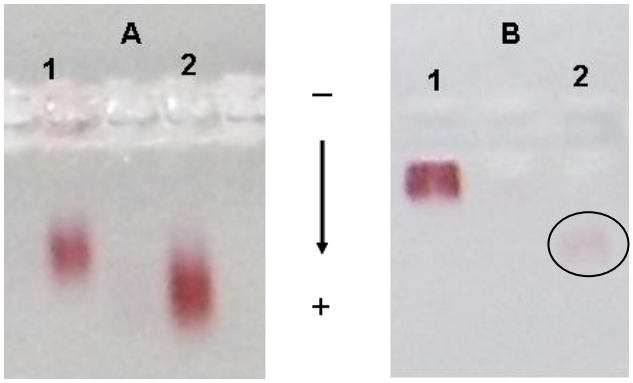


Figure 3.20. *Agarose gel electrophoresis of streptavidin-AuMPC bioconjugates. (A) lane 1: STV bioconjugates (ME8, 5.5 nm)and lane 2: corresponding PEG-biotin MPCs (ME6A, 1%, 14 nm; (B) lane 1: streptavidin bioconjugates (ME9, 5.5 nm) and lane 2: corresponding PEG-biotin MPCs (ME7A, 1%, 5.5 nm).*

The additional bulky tetrameric streptavidin conjugates (lanes 1 (ME8 and ME9)) showed slower mobility compared with the corresponding PEG-biotin MPCs (lanes 2 (ME6A and ME7A). The highly conformational bulky nature (60 kDa) of streptavidin could be responsible for such an observation. This is in contrast to the highly mobile carboxylate derivatised MPCs, although for 1% PEG-COOH, the migration was also observed to be slower.

***Part III. Immobilisation of Biotin-TAT peptide via the biotin-(strept)avidin-biotin protocol (BAB).***

The introduction of the TAT peptide, a small basic cell-penetrating peptide was conducted by the BAB protocol, as depicted in Figure 3.21. TAT peptide is a short arginine-rich protein transduction domain, which has found applications in the delivery of biologically active therapeutic cargoes, namely peptides, proteins and antisense oligonucleotides [38-40].

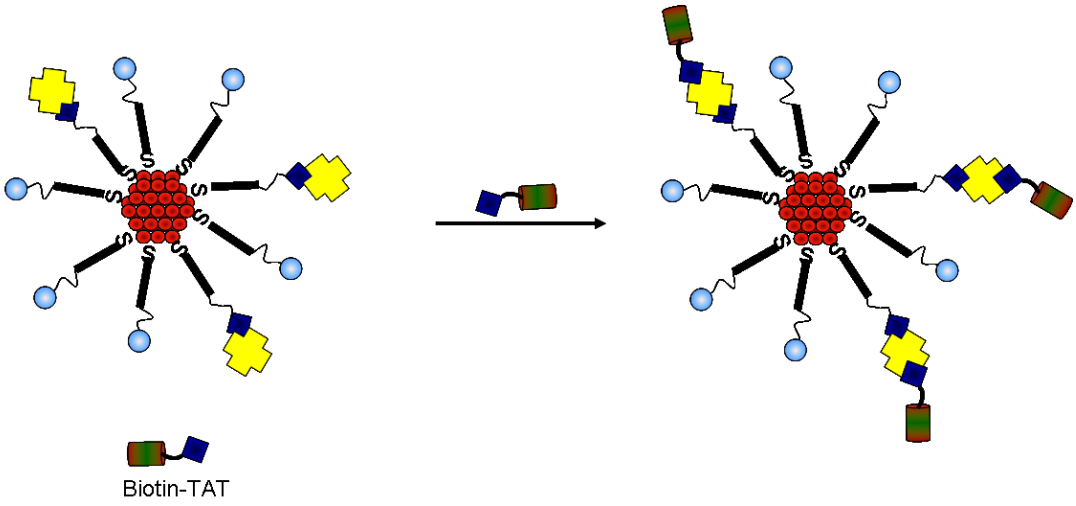


Figure 3.21. *The BAB strategy for the introduction of the TAT CPP onto the surface of streptavidin-MPC conjugates.*

The structural diversity and high variability in their nature makes the mechanism of internalisation of the CPPs to be generally inconclusive. Recent studies have shown that the TAT translocates via the lipid raft-dependent macropinocytosis, although a possible unknown co-mechanism is still feasible [39, 41]. This specialised form of fluid phase

endocytosis is both temperature-dependent and energy-dependent (ATP) [42]. A series of investigations into the factors affecting the TAT CPP-based delivery techniques have been investigated elsewhere, including the influence of the cargo (TAT peptide exposure, hydrophobicity, chemical linkage type of the cargo to the TAT sequence and TAT peptide density) [43-49], cell surface interactions [50-52] and possible mechanisms of uptake [53-54] to name a few. The generic sequence of the TAT peptide is composed of a YGRKKRRQRRR amino sequence although the C- and N- termini have been extended using a wide range of sequences or coupled with other moieties [55].

The conjugation strategy was conducted both on large (ME8, 14 nm) and smaller (ME9, 5.5 nm) nanoparticles. Optical and structural analysis was conducted as presented in Figure 3.22. The immobilisation of the TAT peptide was shown to be a quick process, with an immediate change in the solution colour from blue-tinted red to red. The optical absorption spectra showed the expected SPR with sharp peaks. Particle distribution was observed to be unaffected by the addition of peptide as observed from the narrow peaks and confirmed in the TEM measurements (Figure 3.22A and B).

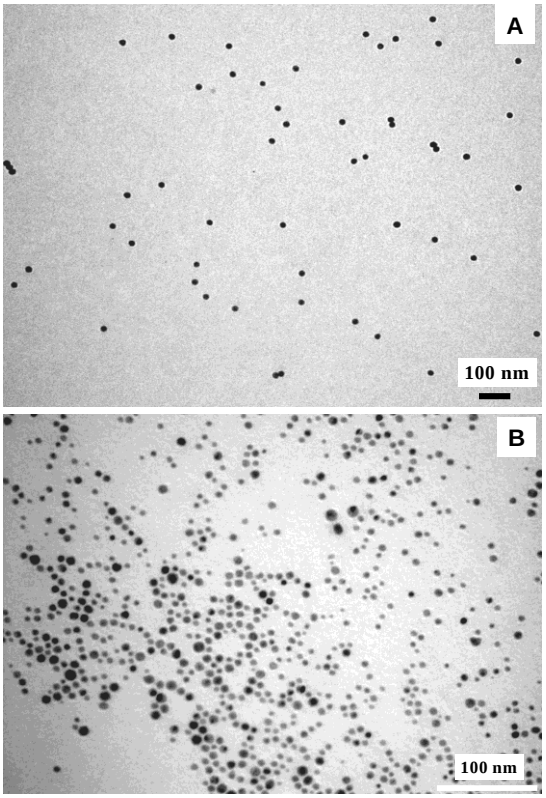


Figure 3.22. S*tructural analysis of the TAT-immobilised bioconjugates. A1 ME10 (14 nm), and B: ME11 (5.5 nm).*

The agarose gel electrophoresis of the TAT bioconjugates was conducted in order to ascertain the attachment events on the streptavidin conjugates. Figure 3.23 shows the comparisons with the corresponding streptavidin conjugates.

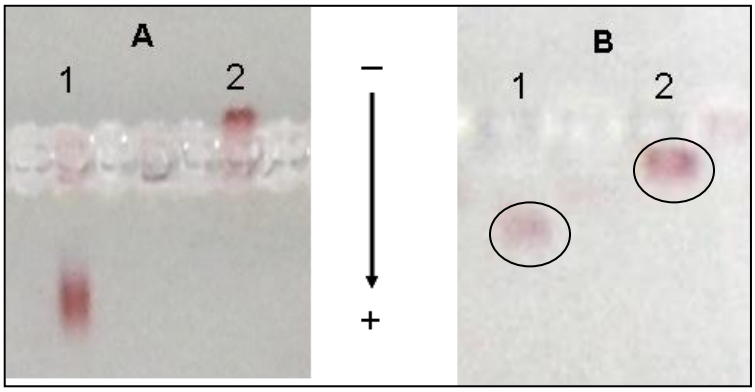


Figure 3.23. *Agarose gel electrophoresis of TAT-immobilised bioconjugates, (A) lane 1: streptavidin conjugates [ME8, 14 nm], lane 2: corresponding TAT bioconjuagates*

*(ME10) and (B) lane 1: streptavidin conjugates [ME9, 5.5 nm] and lane 2: the corresponding TAT bioconjugates (ME11).*

The highly cationic nature of the TAT sequences, owing to the contributions by the preponderant basic residues arginine and lysine, was observed to retard the migration of the conjugates in the gel. This was also coupled with the additional peptide size on the surface of the MPCs. This result presents a facile, yet immensely indispensable route for the introduction of a CPP onto the surface of gold MPCs. This tool kit is specifically designed for applications in the areas of biolabeling and targeted drug delivery whereupon the microscopically visible gold cores will be used for visualization and tracking purposes.

***Part IV. Immobilisation of FAM-TAT peptide via the EDC/NHS coupling route.***

A second strategy for the introduction of the TAT peptide was devised employing the carbodiimide coupling route on the streptavidin conjugates. The availability of the terminal amine rich arginine residue on the TAT sequence was exploited in this technique. The –COOH functionality of the streptavidin was used to form the amide bond with the amine functionality of the TAT peptide. The FAM (6-carboxyfluorescein) fluorescent tag on the TAT peptide was however not exploitable since the gold is well-known for charge-transfer efficiency, which quenches the fluorescence [56]. Furthermore, the FAM absorbs (492 nm) and emits (517 nm) in the gold SPR range and therefore cannot be directly quantified without the interfering contributions from the gold core [57].

The introduction of the FAM-TAT via the carbodiimide coupling reaction was conducted. The UV-vis absorption spectra of the FAM-TAT bioconjugates are presented in Figures 3.24A1 (ME12, 14 nm) and B1 (ME13, 5.5 nm). The expected SPR range absorption is observed as indicated. The sharp peaks also signified the dispersity of the conjugates. The lack of the FAM label absorption peak at 492 nm was further proof of the quenching ability of the gold MPC core. Such observations have been exploited elsewhere for labeling applications [58]. The TEM micrographs (Figure 3.24A2, ME13 and Figure 3.24B2, ME14) confirmed the size dispersity as observed in the absorption

spectra. There were no signs of aggregation with the MPCs remaining monodisperse. The conjugation was investigated using agarose gel electrophoresis (Figure 3.25).

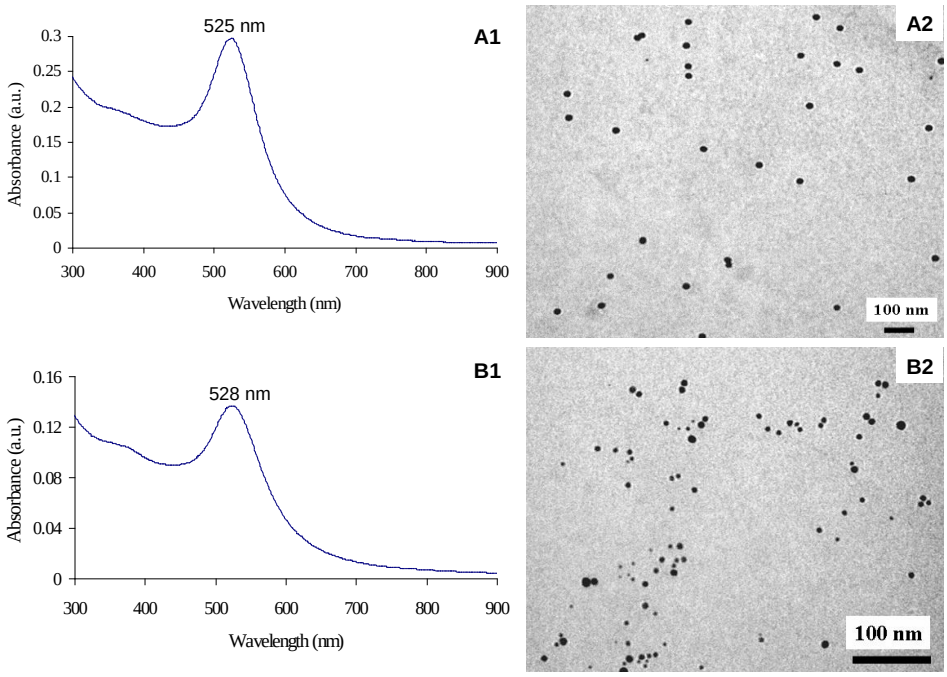


Figure 3.24. *Optical and structural analysis of the FAM-TAT gold bioconjugates; A1) and A2) ME12 (14 nm) and B1) and B2) ME13 (5.5 nm).*

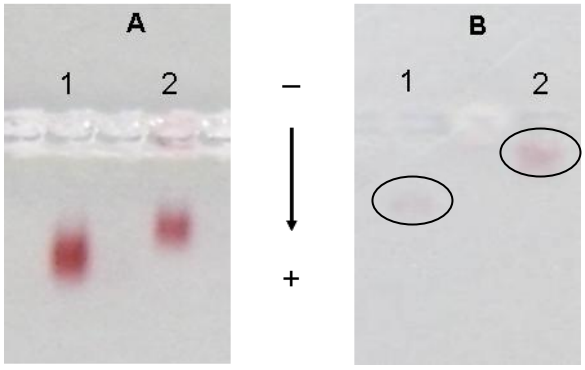


Figure 3.25. *Agarose gel electrophoresis of the FAM-TAT gold bioconjugates; A) lane 1: streptavidin conjugates (ME8, 14 nm), lane 2: corresponding FAM-TAT bioconjugates (ME12); B) lane 1: streptavidin conjugates (ME9, 5.5 nm) and lane 2: corresponding FAM-TAT bioconjugates (ME13).*

The FAM-TAT conjugates (Figure 3.25, ME12 and ME13 – lanes 2**)** were observed to migrate slower than the free streptavidin conjugates (Figure 3.25, ME8 and ME9 -lanes 1), due to the size and cationic contribution of the TAT peptide; increasing the size and importantly lowering the negative charge on the surface of the conjugates. Gold MPCs bearing fluorescent tags have been employed in nucleotide sensing applications, in a mechanism involving the cleavage of the fluorescent tag from the gold core allowing the reestablishment of fluorescence [56].

### 3.3.4. PEG-NTA Gold MPCs: Synthesis and Biofunctionalisation [59]

***Part I: Synthesis*.**

The incorporation of the NTA moiety on nanosized magnetic particles has been reported by Xu *et al.* demonstrating the ability of these nanoparticles to chelate to the bidentate $Ni^{2+}$ cation [60]. Chen *et al* further exploited this technique by incorporating the Ni-NTA onto superparamagnetic particles for the enrichment of 6xHis-tagged proteins and other phosphorylated peptides [61]. In the current approach, the PEG-NTA was introduced onto the nanoparticles via the ligand place-exchange approach of the loosely-bound citrate-capped gold nanoparticles, in a one-step reaction. The first attempt was conducted with PEG-OH as the co-stabiliser for the 14 nm particles.

The lucrative applications of the NTA-based materials in the purification, enrichment and separation of 6xHis-tagged proteins are unparalleled. The ease of the synthesis and control of the surface loading of the NTA governs this possibility. Using the co-stabilisation strategy with PEG-OH, the PEG-NTA was introduced onto the gold surface and the NTA loading was controlled by the variations in stoichiometric amounts of NTA ligand. Optical properties and TEM analysis (Figure 3.26) as well the agarose gel electrophoresis analysis (Figure 3.27) were conducted. Figures 3.25A1, B1 and C1 illustrate the optical absorption of the purified NTA-derivatised gold MPCs. The absorption peaks were narrow owing to the dispersity of the MPCs. The TEM results in Figures 3.25A2, B2 and C2 showed the lack of aggregation of the MPCs.

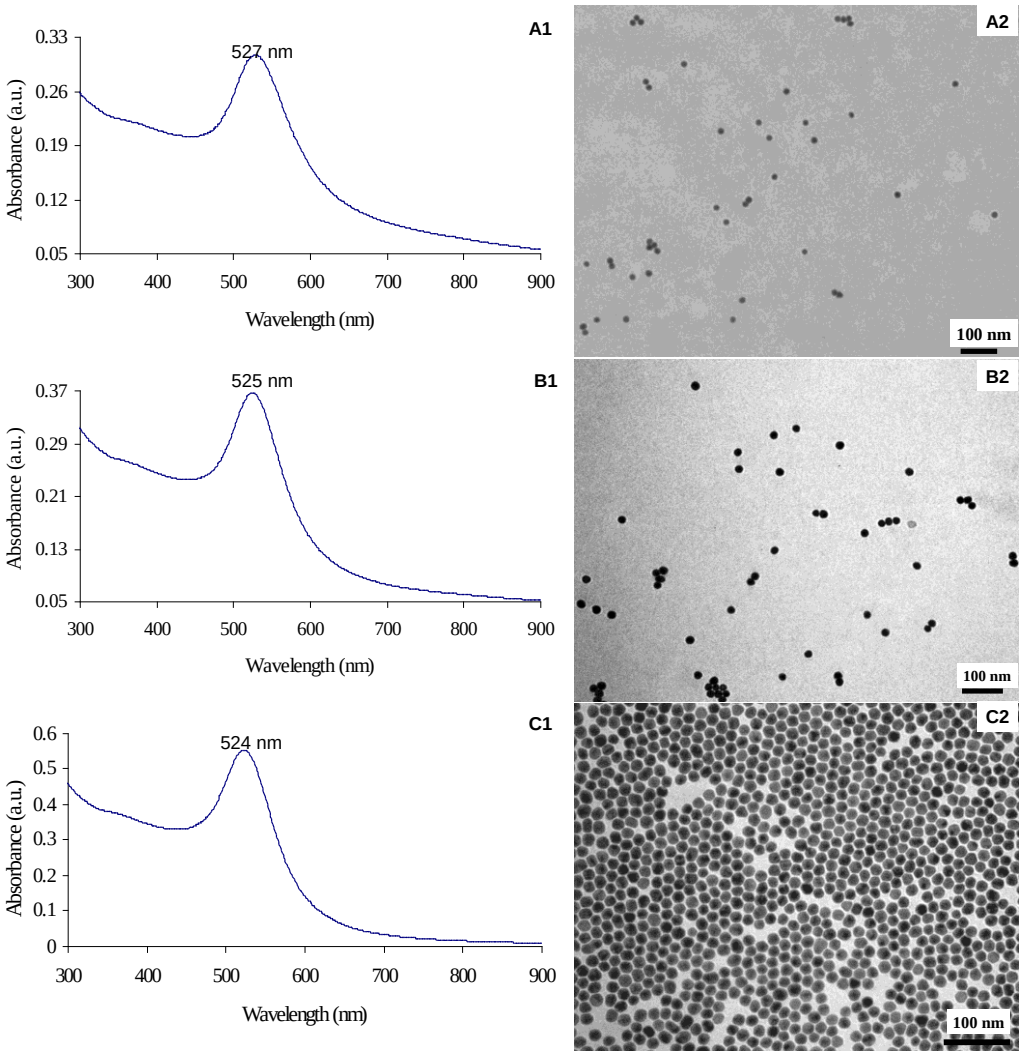


Figure 3.26. *Analysis of PEG-NTA functionalised gold MPCs (14 nm). A1, B1 and C1, optical absorption of 1% [ME14A, 14 nm], 10% [ME14B, 14 nm] and 50% [ME14C, 14 nm] and A2, B2 and C2, corresponding TEM micrographs of 1%, 10% and 50% PEG-NTA gold MPCs.*

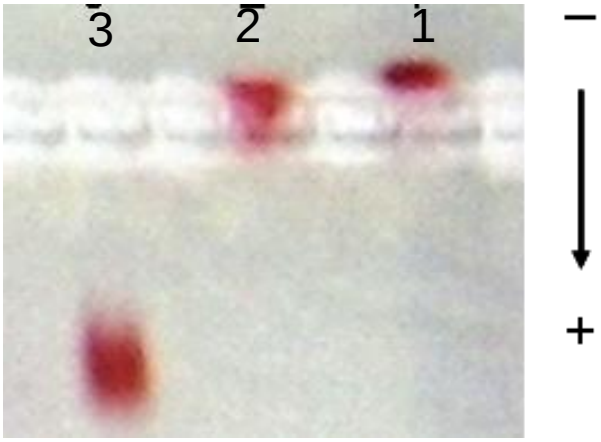


Figure 3.27. *Agarose gel electrophoresis of PEG-NTA functionalised MPCs; lane 1: ME14A (1%), lane 2: ME14B (10%) and lane 3: ME14C (50%).*

The formation of patterned assemblies of the MPCs is observed with the increase in the PEG-NTA surface loading. This effect can be attributed to the hydrogen bonding by the three carboxyl groups of the NTA moiety; representing six possible hydrogen bonding sites between neighbouring NTA moieties of the two particles [62]. This is however not strictly followed in solution due to the ionisation of the carboxyl groups. Also, there is a propensity for hydrogen bonding to occur between the carboxyl groups of the same NTA moiety. Previous studies for the determination of the surface pKa of the NTA determined concluded a value centred around 5.8 [63,64]. The synthesis protocol in this approach was conducted at pH of 5-6 and therefore a reasonable proportion of the NTA is expected to be ionised in solution due to the low dissociation constant.

The formation of the close-packed MPC dispersions was thus concluded to be due to interparticle hydrogen bonding. Due to this effect, 100% PEG-NTA surface coverage proved unsuccessful, with the MPCs aggregating and settling out of solution. Agarose gel electrophoresis was conducted to investigate the binding events of the PEG-NTA on the surface (Figure 3.26). A systematic increase in mobility was observed with the increase in the PEG-NTA content, signify an increase in surface negative charge. Lane 3, representing the highest PEG-NTA content (ME14C) migrated substantially faster than ME14C (lane 2, 10%) as well as ME14A (lane 1, 1%).

The synthesis of PEG-NTA gold MPCs costabilised with PEG-COOH was also attempted. Measurements such as UV-vis, TEM (Figure 3.28) and agarose gel

electrophoresis (Figure 3.29) were done. The absorption UV-vis absorption measurements showed narrow peaks in the absorption spectra due to the lack of aggregation of the MPCs, as also demonstrated in the TEM measurements (Figure 3.27A, B and C).

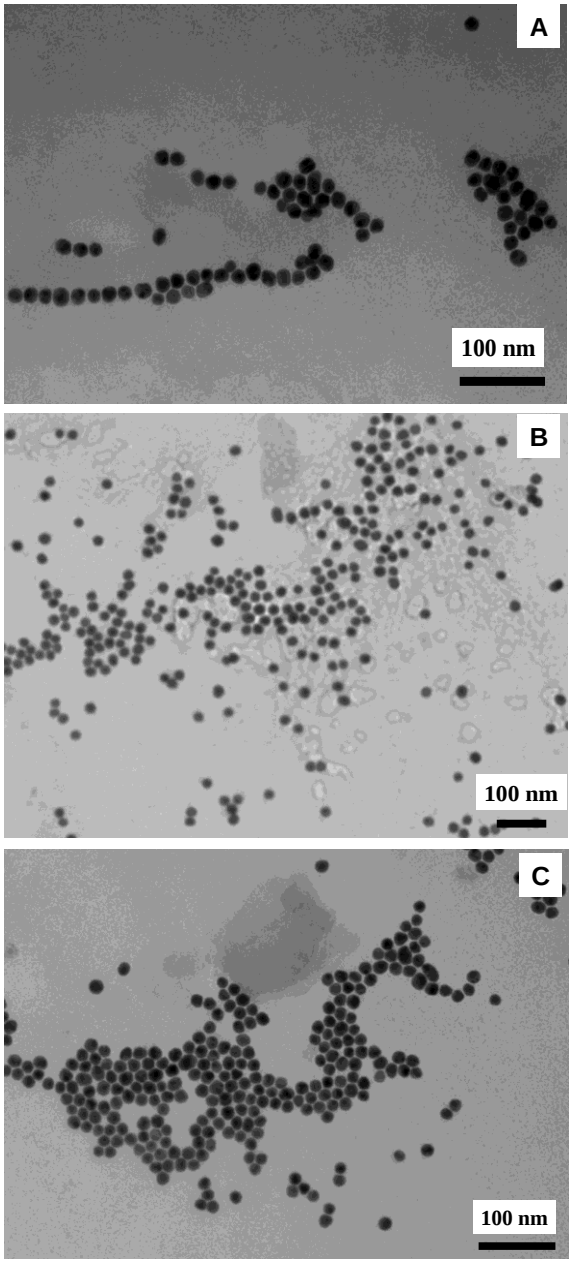


Figure 3.28. *Analysis of PEG-NTA, PEG-COOH costabilised gold MPCs (14 nm). A1, B1 and C1, optical absorption of 1% [ME15A, 14 nm], 10% [ME15B, 14 nm] and 50% [ME15C, 14 nm] and A2, B2 and C2, corresponding TEM micrographs of 1%, 10% and 50% PEG-NTA gold MPCs.*

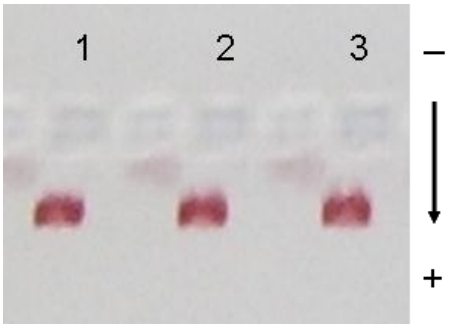


Figure 3.29. *Agarose gel electrophoresis of PEG-NTA functionalised MPCs costabilised with PEG-COOH; lane 1: ME15A (1%), lane 2: ME15B (10%) and lane 3: ME15C (50%).*

The agarose gel electrophoresis analysis was conducted and is presented in Figure 3.28. The migration rate for all the samples (1% - lane 1, 10% - lane 2 and 50% - lane3) was shown to be similar under TBE buffer environment (pH 8). This was due to the uniformity of the surface charge from both the contributions of the -COOH and NTA functionalities. This result demonstrated the resolving ability of agarose gel electrophoresis in probing ligand-place exchange reactions on the surface of the gold core.

The synthesis of PEG-NTA MPCs co-stabilised with PEG-OH was also conducted for the smaller gold core MPCs. Figure 3.20 depicts the TEM results. Similarly, the higher PEG-NTA loading showed patterned growth due to hydrogen bonding effects. The reaction was also investigated with agarose gel electrophoresis (Figure 3.31). The higher concentrations of the PEG-NTA (lane 2, ME16B) showed higher mobility as the response to the addition of negative -COOH moieties on the surface.

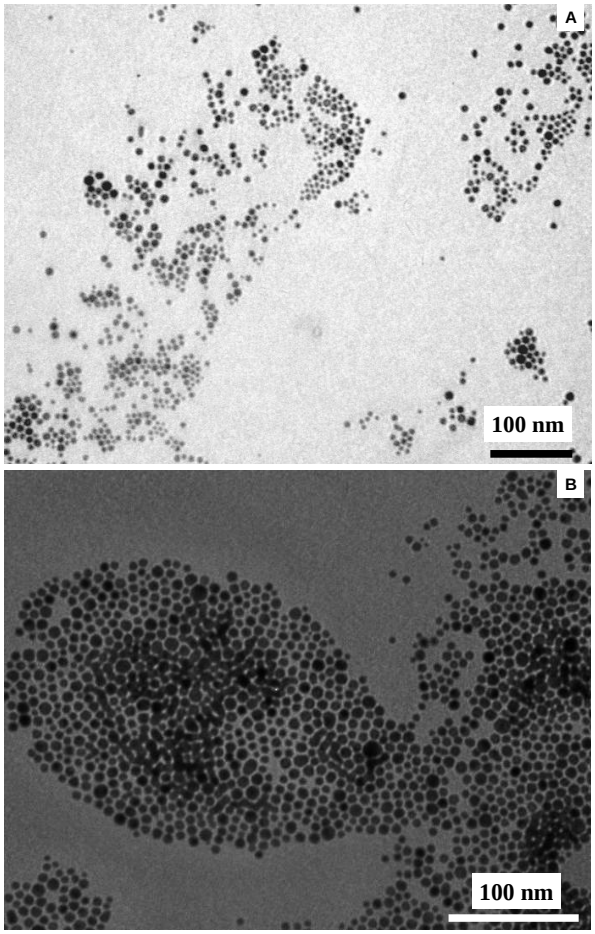


Figure 3.30. *TEM micrograph of PEG-NTA MPCs, costabilised with PEG-OH (A) ME16A and (B) ME16B.*

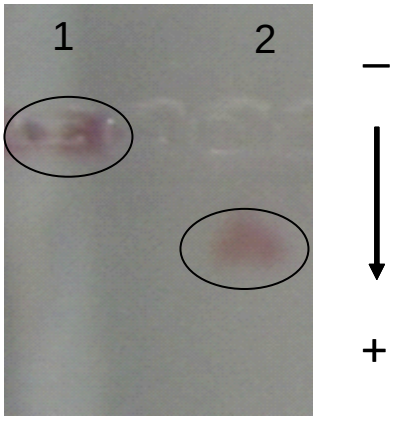


Figure 3.31. *Agarose gel electrophoresis; lane 1: 1% [ME16A, 5.5 nm] and lane 2: 10% PEG-NTA MPCs [ME16B, 5.5 nm].*

The NTA-containing MPCs present a versatile possibility of incorporating histidine-tagged biomolecules via the nickel chelation procedure. This reaction was also investigated in this work.

***Part II: Incorporation of $Ni^{2+}$ Cations.***

The incorporation of the bivalent hexadentate Ni(II) into the NTA matrix was conducted as depicted in Figure 3.31. The quadridentate NTA occupies four coordination positions on the hexadentate central nickel cation allowing for the availability of the two vacant binding sites for a 6xHis-tagged biomolecules to attach. This approach seeks to address the simplicity in the Ni-NTA protein purification and enrichment techniques, by employing a versatile liquid phase probe as opposed to the conventional solid phase resin-based immobilisation techniques.

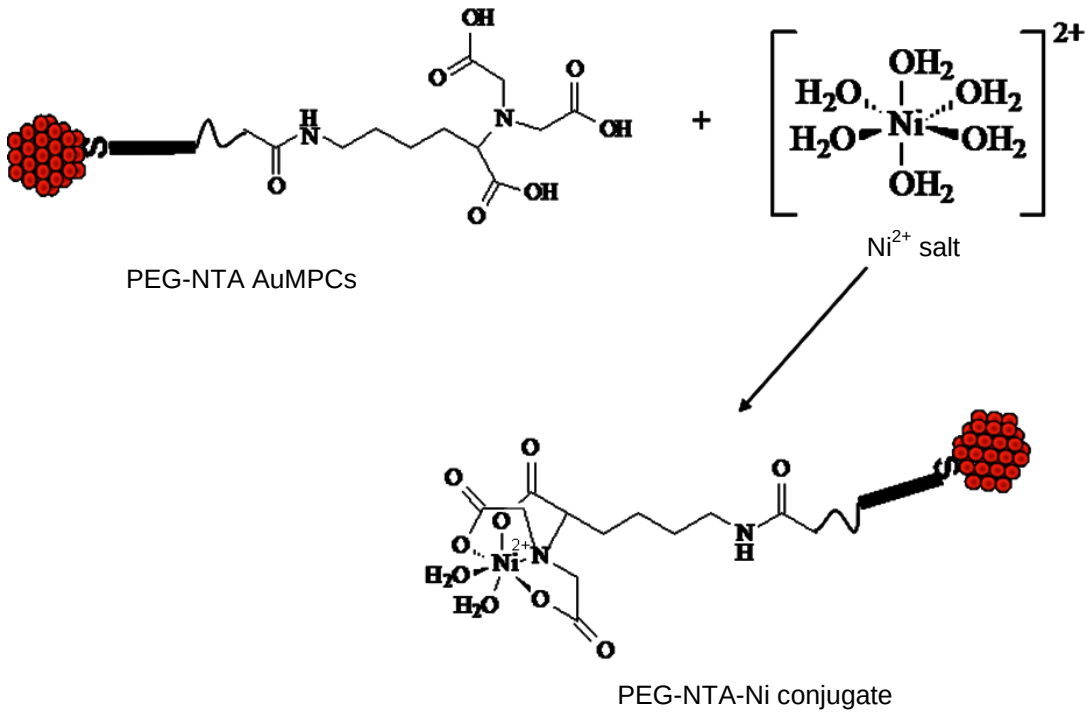


Figure 3.32. *The introduction of the $Ni^{2+}$ cations into the NTA of the PEG-NTA gold MPCs.*

Following the reaction of the 1% PEG-NTA MPCs [ME14A, 14 nm] with excess $NiCl_2$, there was a distinct change in the colour and behaviour of the resultant PEG-NTA-Ni

conjugates [**ME17**, 14 nm]. The optical absorption measurements are presented in Figure 3.33.

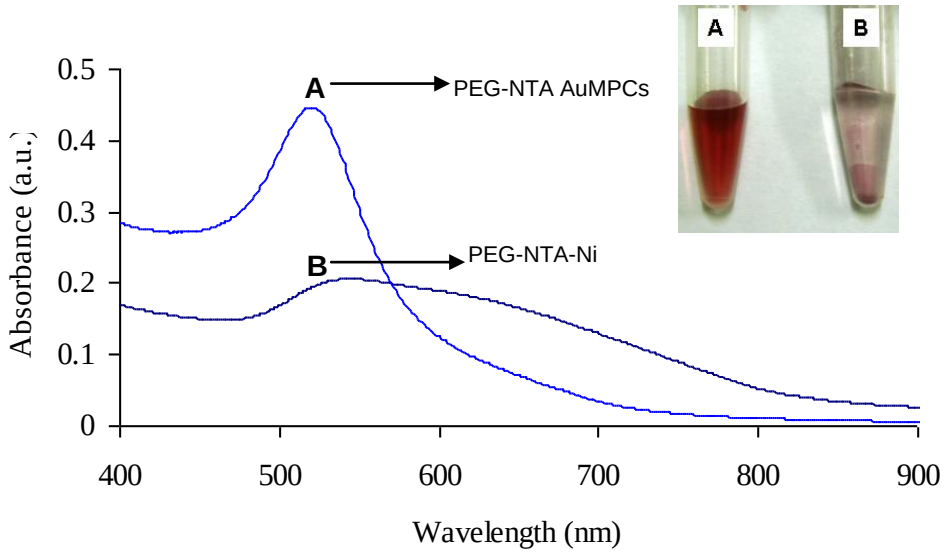


Figure 3.33. *UV-Vis absorption spectrum for the PEG-NTA-Ni (B, ME17) compared with the 1% PEG-NTA MPCs (B, ME14A) from which it was synthesised. Inset: the distinct physical changes on addition of the Nickel (II).*

The optical absorption of the PEG-NTA-Ni gold conjugates presented in Figure 3.32 (B) showed a broad SPR absorption peak with low intensity located at 543 nm, a large red-shift (15 nm) from 528 nm of the PEG-NTA MPCs. The addition of the highly cationic nickel (II) diminishes the negative charge on the surface of the MPCs thus lowering the Coulombic repulsions among the MPCs. This lowering of electrostatic repulsions promotes the dominant effective van der Waals attractive interactions and therefore lead to particle aggregation [64,65]. The MPCs were observed to stick onto the sample tubes and were poorly dispersible in the solvent of choice, and thus the yield dropped considerably during centrifugation (inset, Figure 3.32), signifying high nonspecific binding.

***Part III: Immobilisation of 6xHis-tagged MAP kinase.***

Mitogen-activated protein kinase (MAP Kinase) belongs to a family of proteins activated as a response to cellular stresses as well as to inflammatory cytokines [67]. This response

is both effected by chemical and physical property changes altering cellular functions such as survival, proliferation potential and other cellular processes engaged in the homeostasis and health of the organism. Changes in the nutrients, growth factors, osmolarity and cytokines lead to the dual phosphorylation of tyrosine and threonine residues in a conserved Thr-Xaa-Tyr (Xaa representing any other amino acid residue) sequence in the activation loop of kinase subdomain VIII [68,69]. The MAP kinase transduction pathway presents a rapid method for the study of intricate systems by tracking the critical housekeeping molecular activities of MAP kinase [70]. The MAP kinase activities have been applied in tracking and identifying human diseases such as Alzheimer's disease, a progressive neuronal degeneration commonly responsible for the dementia syndrome [71].

The strategy for the introduction of the MAP kinase was conducted through the Ni-NTA affinity strategy employing a histidine-tagged fusion version of MAP kinase. The attachment of the 6xHis-tagged proteins onto the Ni-NTA derivatised materials occurs at the nitrogen of two separate imidazole rings of the histidine amino acids (Figure 3.34).

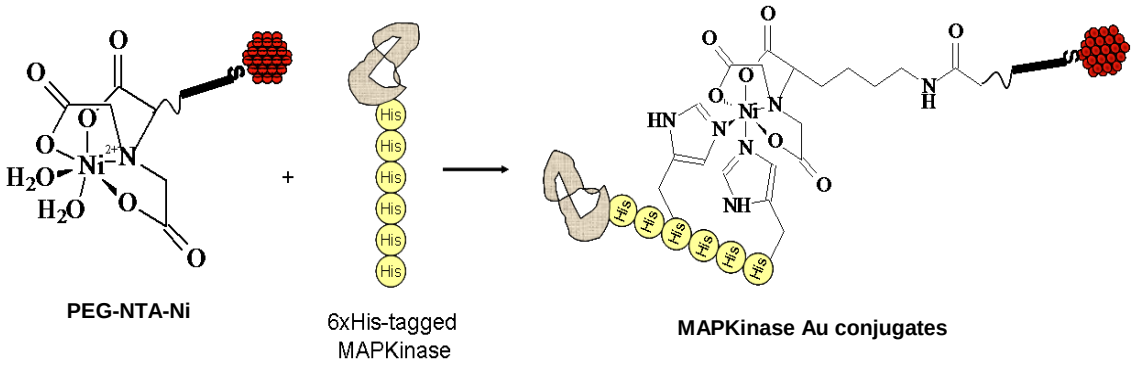


Figure 3.33. *The attachment strategy of 6xHis-tagged MAP kinase onto the surface of the Ni(II) bound gold MPCs.*

The histidine imidazole side chain with a pKa value of 6.0 requires the histidine to possess a near neutral charge at neutral pH and by so doing allows histidine to play a major role as a proton donor and acceptor in many enzyme reactions [72].

The immobilisation of the hexahistidine-tagged MAP kinase was achieved by the direct reaction of the PEG-NTA-Ni conjugates [ME16, 14 nm] with the protein. On

visual inspection, the formation of the soluble MAP kinase showed a marked physical change on formation (Figure 3.35 inset). The resultant MAP kinase bioconjugates were readily soluble in water and showed the typical red colour of gold clusters. Optical absorption measurements showed a sharp peak in the expected gold SPR region of 520 nm. Optical absorption comparisons of the PEG-NTA MPCs with PEG-NTA-Ni conjugates and MAP Kinase conjugates (Figure 3.35) showed that the peak sharpness is restored after the addition of the MAP Kinase protein. The immobilisation of the protein was also studied through the agarose gel electrophoresis experiment as presented in Figure 3.36.

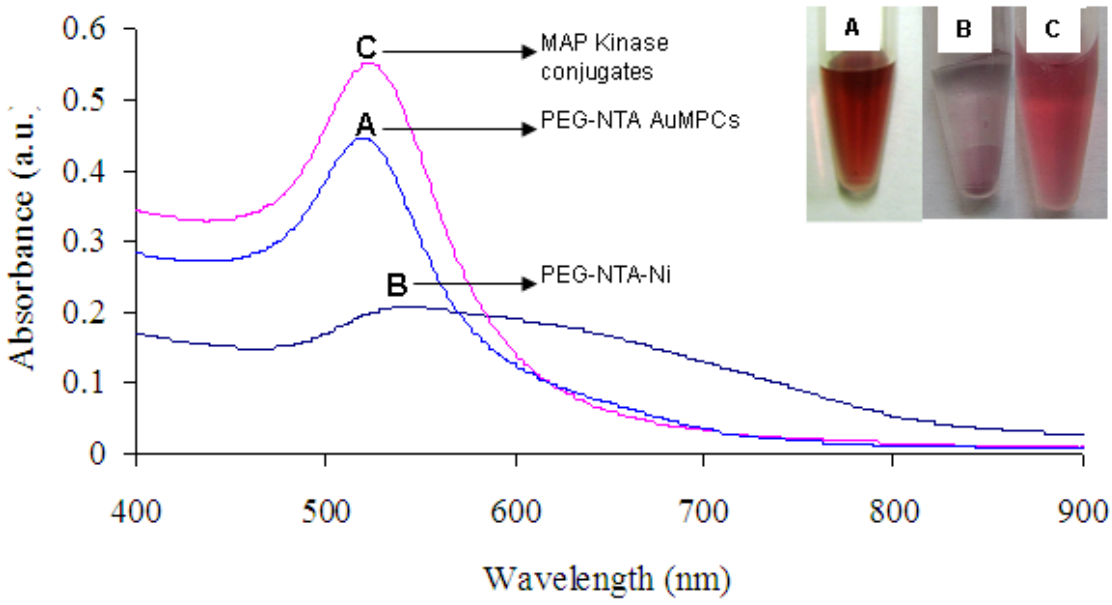


Figure 3.35. *Optical absorption measurements for the 6xHis-tagged MAP kinase bioconjugates (ME18, 14 nm). Inset: Visual comparison of (A) PEG-NTA conjugates, (B) PEG-NTA-Ni gold conjugates (ME17) and (C) the MAP kinase gold bioconjugates.*

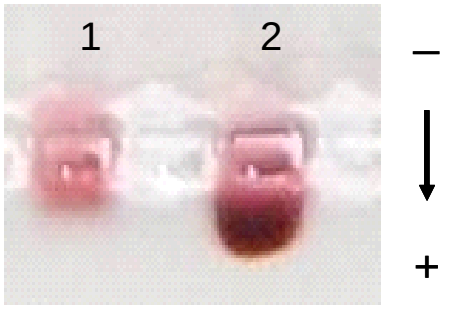


Figure 3.36. *Agarose gel electrophoresis analysis of the 6xHis-tagged MAP kinase bioconjugates. Lane 1: MAP kinase bioconjugates (ME18, 14 nm) and lane 2: 1% PEG-NTA gold MPCs (ME14A, 14 nm).*

The additional highly conformational bulky protein showed a slower mobility in the gel electrophoresis (lane 1, ME18) compared with the precursor 1% PEG-NTA gold MPCs (lane 2, ME14A). The TEM micrograph of the MAP kinase bioconjuagates is presented in Figure 3.37. No apparent aggregation was observed although there was some degree of self-assembly. This can be attributed to interparticle interactions between PEG-NTA-Ni MPCs and those containing the 6xHis-tagged MAP kinase.

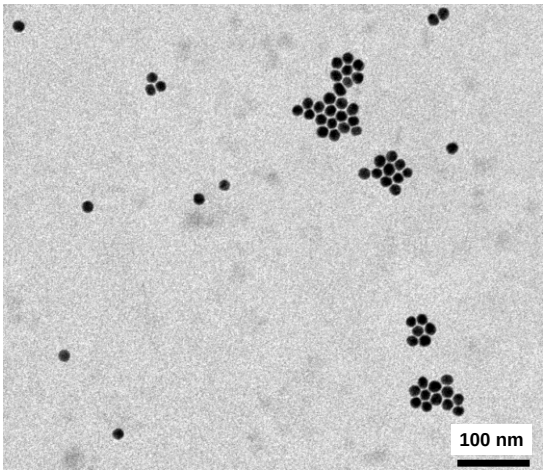


Figure 3.37. *TEM structural analysis micrograph of the 6xHis-tagged MAP kinase bioconjugates (ME18, 14 nm).*

In principle since each bivalent nickel accepts two electron densities from the two imidazole rings, a total of three binding events can occur on one MAP kinase conjugate.

This result adds to the arsenal of high-affinity protein immobilisation strategies on the surface of gold monolayer protected clusters.

## 3.4. SUMMARY AND CONCLUSIONS

The synthesis of monolayer protected clusters was achieved via the direct ligand place-exchange reactions. The MPCs revealed high water solubility and good resistant to aggregation under the vigorous purification conditions. This was followed by the introduction of various biomolecules using four protocols, (i) the carbodiimide coupling method, (ii) the biotin-streptavidin interaction method, (iii) the biotin-streptavidin-biotin (BAB) method and (iv) the Ni-NTA based immobilisation of 6xHis-tagged proteins. An illustration of the various entities introduced on the gold core is presented in Figure 3.38.

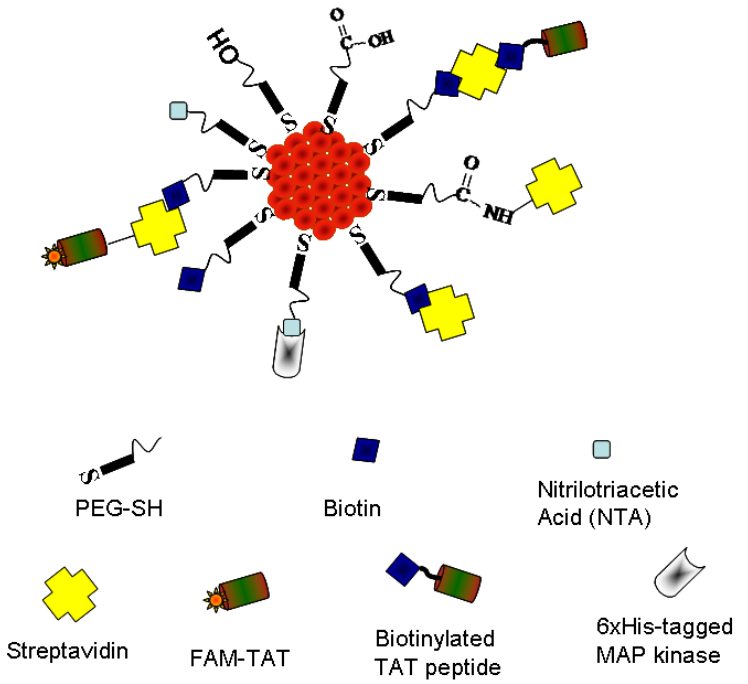


Figure 3.38. *A schematic demonstration of the different functionalities that have been successfully incorporated onto the gold core, using various protocols.*

The MPCs present facile molecular handles for the immobilisation of biomolecules, whilst possessing interesting properties such as non-specific binding, hydrophilicity and biocompatibility as a consequence of the incorporation of the PEG polymer. Through this

investigation a foundation for applications ranging from targeted drug delivery (TAT peptide), biorecognition and biodiagnostics (BAB and Ni-NTA systems) was laid. MPC-based bioconjugates of the different biomolecules showed significant stabilities through the purification experiments. Charge distribution, size and conformation was used as a mode of following the binding effects on the surface of the MPCs through the agarose gel electrophoresis.

## 3.5. REFERENCES


1. Giersig M. and Mulvaney P., *Langmuir*, 1993, **9**, 3408.
2. Brust M., Walker M., Bethell D., Schiffrin J and Whyman R., *Chem. Commun*., 1994, 801.
3. Brust M., Fink J., Bethell D., Schiffrin J and Kiely C., *Chem. Commun*., 1995, 1655.
4. Yee C., Scotti M., Ulman A., White H., Rafailovich M. and Sokolov J., *Langmuir*, 1999, **15**, 4314.
5. Quiros I., Yamada M., Kubo K., Mizutani J., Kurihara M and Mishihara H., *Langmuir*, 2002, **18**, 1413.
6. Pasquato L., Pengo P. and Scrimin P., *J. Mater. Chem*., 2004, **14**, 3481.
7. A.G. Barrientos, J.M. de la Fuente, T.C. Rojas, A. Fernandez and S. Penades, *Chem. Eur. J*., 2003, **9**, 1909
8. G.F. Paciotti, L. Myer, D. Weinreich, D. Goia, N. Pavel, R.E. McLaughlin and L. Tamarkin, *Drug Delivery*, 2004, **11**(3), 169
9. Wuelfing W.P., Gross S.M., Miles D.T. and Murray R.W., *J. Am. Chem. Soc*., 1998, **120**, 12696.
10. Foos E.E., Snow A.W., Twigg M.E. and Ancona M.G., *Chem. Mater*., 2002, **14**, 2401.
11. a) Hong R., Fischer N.O., Emrick T. and Rotello V.M., *Chem. Mater*., 2005, **17**, 4617; b) Shenhar R. and Rotello V.M, *Acc. Chem. Res*., 2003, **36**, 549
12. Kanaras A.G., Kamounah F.S., Schaumburg K., Kiely C.J. and Brust M., *Chem. Commun*., 2002, 2294.
13. Tshikhudo T.R., Wang Z. and Brust M., *Mater. Sci. and Technol*., 2004, **20**, 980.

14. Tshikhudo R.T., Demuru D., Wang Z., Brust M., Secchi A., Arduini A. and Pecchini A., *Angew. Chem. Int. Ed*., 2005, **44**, 2
15. Templeton A.C., Cliffel D.E. and Murray R.W., *J. Am. Chem. Soc.*, 1999, **121**, 7081
16. Kim Y.-S., Cho J.-H., Ansari S.G., Kim H.-Il, Dar M.A., Seo H.-K., Kim G.-S., Lee D.-S., Khang G. and Shin H.-S., *Synthetic Met.*, 2006, **156**, 938
17. Bayer M.W. and Bayer E.A., *Methods Enzymol.*, 1990, **184**, 14.
18. Chaiet L. and Wolf F.J., *Arch. Biochem. Biophys.*, 1964, **106**, 1
19. Weber P.C., Wendoloski J.J., Pantoliano M.W. and Salemme F.R., *Science*, 1989, **243**, 85
20. Porath J., Carlsson J., Olsson I. and Belfrage G., *Nature*, 1975, **258**, 598
21. Hochuli E., Dobeli H. and Schacher A., 1987, *J. Chromatogr*., 1988, 411, 177
22. Hull J.A., davies R.H. and Staveley L.A.K., J. *Chem. Soc. A*, 1964, 5422
23. Irving H.M.N.H. and Miles M.G., *J. Chem. Soc. A*., 1966, 1268
24. Paborsky L.R., Dunn K.E., Gibbs C.S. and Dougherty J.P., *Anal. Biochem.*, 1996, 234, 60
25. Turkevitch J., Stevenson P.C. and Hillie J., Discuss. Faraday Soc., 1951, 11, 55.
26. Harmison G.T., *Bioconjugate Techniques, A*cademic Press, Elsevier, London, p597.
27. Liz-Marzan L.M., *Langmuir*, 2006, **22** (1), 32.
28. Papavassiliou G.C., *Prog. Solid State Chem.*, 1979, **12**, 185.
29. Mulvaney P., *Langmuir*, 1996, **12**, 788.
30. Nie S. and Emory S.R., *Science*, 1997, **275**, 1102.
31. a) Eustis S and M. El-Sayed M., *Chem. Soc. Rev.*, 2006, **35**, 209; b) Link S. and el-Sayed M., *Annu. Rev. Phys. Chem.*, 2003, **54**, 331.
32. Shi W., Sahoo Y. and Swihart M.T., Colloids and Surfaces A: Physicochem. Eng. Aspects, 2004, 246, 109
33. Fu S., Li D. and Lucy C.A., *Analyst*, 1998, **123**, 1487
34. D.F. Detar and R. Silverstein, *J. Am. Chem. Soc.*, 1996, **88**, 1013
35. Savage D., Matson G., Desai S., Nielander G., Morgensen S. and Conklin E., *Avidin-Biotin Chemistry: A Handbook*, Pierce Chemical Co., Rockford, Illinois, 1992
36. Henrickson W.A., Pahler A., Smith J.L., Satow Y., Merritt E.A. and Phizackerley R.P., *Proc. Natl. Acad. Sci. U.S.A.*, 1989, **86**, 2190

37. Freitag S., Le Trong I., Stayton P.S. and Stenkamp R.E., *Protein Sci.*, 1997, **6**, 1157
38. Cao G., Pei W., Ge H., Liang Q., Luo Y., Sharp F.R., Lu A., Ran R., Graham S.H. and Chen J., *J. Neurosci.*, 2002, **22** (13), 5423
39. Kaplan I.M., Wadia J.S. and Dowdy S.F., *J. Controlled Release*, 2005, **102**, 247
40. Schwarze S.R., Ho A., Vocero-Akbani A. and Dowdy S.F., *Science*, 1999, **285**, 1569
41. Wadia J.S., Stan R.V. and Dowdy S.F., *Nat. Med.*, 2004, **10**, 310
42. Conner S.D. and Schmid S.L., *Nature*, 2003, **422**, 37
43. Shimazaki K., Urabe M., Monahan J., Ozawa K. and Kawai N., *Gene Ther.*, 2000, 7, 1244
44. Bolton S.J., Jones D.N., Darker J.G., Eggleston D.S., Hunter A.J. and Walsh F.S., *Eur. J. Neurosci.*, 2000, **12**, 2847
45. Ignatovich I.A., Dizhe E.B., Pavlotskaya A.V., Akifiev B.N., Burov S.V. and Orlov S.V., *J. Biol.Chem.*, 2003, **278**, 42625
46. Dietz G.P., Kilic E. and Bahr M., *Mol. Cell. Neurosci.*, 2002, **21**, 29
47. Antonawich F.J., Federoff H.J. and Davis J.N., *Exp. Neurol.*, 1999, **156**, 130
48. Shen J., Mai J.C., Qiu L., Cao S., robbins P.D. and Cheng T., *Hum. Gene Ther.*, 2004, **15**, 415
49. Lundberg M. and Johansson M., *Biochem. Biophys. Res. Commun.*, 2002, **19**, 713
50. Cutrona G., Carpaneto E.M., Ulivi M., Roncella S., Landt O., Ferrarini M. And Boffa L.C., *Nat. Biotechnol.*, 2000, **18**, 300
51. Soane L. and Fiskum G., *J. Neurochem.*, 2005, **95**, 230
52. Krautwald S., Ziegler E., Tiede K., Pust R. And Kunzendorf U., *J. Biol. Chem.*, 2004, **279**, 44005
53. Marty C., Meylan C., Schott H., Ballmer-Hofer H. and Schwendener R.A., *Cell. Mol. Life Sci.*, 2004, **61**, 1785
54. Nur-e-Kamal M.S., Qureshi M.M., Kamal J.M., Montague W. and Maruta H., *Ann. N.Y. Acad. Sci.*, 1999, **886**, 285
55. Brooks H., Lebleu B. and Vives E., *Adv. Drug Deliver. Rev.*, 2005, 57, 559
56. Tansil N.C. and Gao Z., *Nanotoday*, 2006, **1**(1), 28.
57. Riggs H.J.L., Am. J. Pathol., 1958, **34**, 1082
58. Albarran B., To R. and Stayton P.S., *Protein Eng. Des. Sel.*, 2005, **18** (3), 147

59. Sosibo N.M., Tshikhudo R.T. and Revaprasadu N., in *Quantum-Dot and Nanoparticle Bioconjugates - Tools for Sensing and Biomedical Imaging*, edited by J. Cheon, H. Mattoussi, C.M. Niemeyer, and G. Strouse, Warrendale, PA, 2008, 1064-10
60. Xu. C., Hu K., Gu H., Zhong X., Guo Z., Zheng R., Zheng X. and Xu B., *J. Am. Chem. Soc.*, 2004, **126**, 3392
61. Li Y.-C., Lin Y.-S., Tsai P.-J., Chen C.-T., Chen W.-Y. and Chen Y.-C., *Anal. Chem.*, 2007, **79**, 7519
62. Tereste D., Pincet F., Perez E., Rickling S., Mioskowski C. and Lebeau L., *Biophysical J.*, 2002, **83**, 3675
63. Zhao X., Ong S., Wang H. and Eisenthal K.B., *Chem. Phys. Lett.*, 1993, **214** (2), 203
64. Betts J.J. and Pethica B.A., *Trans. Faraday*, 1956, 1581
65. Creighton J.A., Alvarez M.S., Weitz D.A. and Kim M.W., *J. Phys. Chem.*, 1983, **87**, 4793
66. Blatchford C.G., Campbell J.R. and Creighton J.A., *Surf. Sci.*, 1982, **120**, 435
67. Cuenda A. and Rousseau S., *Biochim. Biophys. Acta*, 2007, **1773**, 1358
68. Bardwell L. and Thorner J., *Trends Biochem. Sci.*, 1996, **21**, 373
69. Biondi R.M. and Nebreda A.R., *Biochem. J.*, 2003, **372**, 1
70. Koch W., Calder M. and Gilbert D., *FEBS Lett.*, 2005, **579**, 1891
71. Johnson G.V.W. and Bailey C.D.C., *Exp. Neurol.*, 2003, **183**, 263
72. Garrett R.H. and Grisham C.M., *Biochemistry*, Saunders College Publishers, Fort Worth, 1995, p86

# CHAPTER 4: CYTOTOXICITY EVALUATION OF COLLOIDAL GOLD NANOPARTICLES, MONOLAYER PROTECTED CLUSTERS AND BIOMOLECULAR CONJUGATES

## 4.1. INTRODUCTION

The application of nanosized inorganic materials in chemical, biomedical and diagnostics among others has spawned a multidisciplinary effort in the design and fabrication of smart and stealth hybrid materials [1]. The power of these nanomaterials lies in their exploitable physico-chemical properties through structural design, which greatly improves and fine-tunes their electronic, diagnostic and therapeutic functions and performances [2]. Due to the intended applications of nanomaterials, coupled with the ill-defined fundamental cause-effect relationships to suggested toxicological effects of these entities, their interactions with biological systems such as living cells has become an urgent area of collaborative research in biology and materials [3].

The induction abilities of metabolic and immunogenic responses by nanomaterials are currently poorly understood. This is in contrast to common chemical compounds (drugs and therapeutics) that are routinely subjected to well-established toxicological testing prior to public release, a scenario missing for nanomaterials [4]. In light of these shortfalls and the sporadic conflicting reports of similar nanomaterials reported as both toxic [5] and non-toxic [6], concerted efforts have therefore been dedicated in the elucidation of toxicity of nanomaterials. This toxicity has been approached in a three-pronged strategy [7]:

i. Composition of the nanoparticles: the nanomaterials can be composed of toxic materials such as CdSe, which can release toxic cadmium ions inside a live organism that will eventually poison the cell by competing with zinc for binding sites on metallothionein, which is important for storage and transport of zinc during development [8]. Compared to the corresponding bulk materials, partial decomposition and release of ions is highly likely for nanosized CdSe due to the large surface-to-volume ratio.

ii. Chemical properties of the nanoparticles: nanoparticles have been shown to adhere to cell membranes [9] and also be ingested by cells [10]. The breaching of the cell membrane and the intracellular storage may have a negative effect on the cells regardless of the toxicity of the particles and their subsequent functionality.

iii. Nanoparticle morphology: distinctly shaped materials such as carbon nanotubes can rip cells like needles [11]. This in turn suggests that nanomaterials of the same composition would have different biologic responses for different morphologies.

The use of conventional *in vivo* techniques in the study of biologic effects and cytotoxicity caused by nanomaterials is highly informative but also inherently costly and labour-intensive [12]. This has rendered *in vivo* techniques ill-suited for systematic and routine biologic investigations in light of the sheer number of diverse nanomaterials currently in development. Various mammalian cell culture models have long been considered as a simpler, cost-effective and convenient alternative in the assessment of nanomaterial toxicity as compared to the use of live animal models [13]. Advantages of the *in vitro* approach include simplicity, consistency of the experimental setup and the reproducibility of the experimental results [14].

The *in vitro* approach encompasses the testing of viability or fluctuations in a designated inherent biological pathway selected against the nanomaterials of interest. Such testing is also motivated by the ever increasing scope of applications of engineered nanomaterials requiring the design and development of effective and reliable *in vitro* assays [15, 16]. Common assays for toxicity studies use the measurements of triozonium salt cellular metabolic activities such as the 3-(4,4-dimethylthiozol-2-yl)-2,5 diphenyl tetrazonium bromide test (MTT), cellular plasma membranes such as lactate-dehydrogenase (LDH) release assay or the activities of glucose-6-phosphate dehydroginase [17]. *In vitro* assays are robust in nature and have been used extensively in the elucidation of mechanisms of toxicity as well as demonstrating the relevant biological processes that are involved in the response to specific test materials.

*In vitro* measurements of apoptosis as a form of toxicity elucidation has been reported in literature [18]. The approach was based on the measurements of DNA fragmentation occurring in apoptotic cells. Alternatively, the distinct morphological changes accompanying the process of apoptosis (decrease in cell size and membrane phosphotidylserine externalisation) can be used to measure apoptosis as a function of the light scattering properties of the cells (flow cytometry). Information such as the changes in cell size and granularity can be elucidated in this way. Due to the overall loss of size for apoptotic cells through water loss and nuclear fragmentation, apoptotic cells give lower forward scatter and higher side scatter values compared to viable and necrotic cells (loss of cell membrane intergrity), indicating the smaller size as well as different nucleus/ cytoplasm consistency [19].

The neutral red assay procedure is another method for the identification of surviving/ viable cells after treatment with the materials of choice. The assay is based on the ability of viable cells to incorporate and bind neutral red (3-amino-*m*-dimethylamino-2-methyl-phenazine hydrochloride), a weakly cationic supravital dye that penetrates the cell membrane through a non-ionic diffusion process and then subsequently accumulates in the lysosomes [20]. Changes in the cell surface and lysosomal membrane lead to decreased neutral red uptake and binding thus making it possible to distinguish between damaged and viable cells through spectrophotometric measurements [21]. The quantification of dye extracted from the treated cells has been shown to be linear with cell numbers; with cytotoxicity expressed as a concentration dependent reduction of the neutral red uptake, giving a robust, sensitive signal for both cell integrity and growth inhibition [22].

Staining techniques have also been shown to effectively quantify the DNA loss as a function of apoptosis, for instance the use of intercalating DNA dyes such as propidium iodide (PI) and 7-aminoactinomycin D (7-AAD) [23]. Hypotonic solutions of PI dye have been shown as one of the easiest and most rapid methods of DNA staining for apoptosis measurements, strengthening the use in large scale *in vitro* investigations [24]. A staining technique using APOP*ercentage*™ dye assays based on Fluorescence-Activated Cell

Sorting (FACS) has been reported by Meyer *et al*. as an inexpensive, high throughput detection and enumeration tool for apoptosis [25]. The APOP*ercentage*™ assay employs the disodium salt of 3,4,5,6,-tetrachloro-2′,4′,5′,7′-tetraiodofluorescein, a dye that enters the cells during the phosphatidylserine (PS) externalisation process; a development specific only to apoptotic cells. A linear increase in the dye uptake with the extent of apoptosis was observed [25].

Another technique based on the externalisation of PS is annexin V staining. Annexin V binds preferentially to PS, offering a rapid and simple tool for the detection of early apoptosis [26]. The major shortcoming of the annexin V technique is the inability to differentiate between late apoptotic cells and necrotic cells due to increased cell membrane permeability [26]. A combination of annexin V and PI or 7-AAD is used in order to discriminate between late apoptosis to necrotic cells that have lost membrane integrity to early apoptotic cells which still have intact membranes by dye exclusion. The choice between the dyes is guided by the spectral region at which the fluorescence-labelled annexin V (FITC) will be measured so that spectral overlaps are circumvented.

### 4.1.1. Chapter Strategy

Due to the envisaged applications of the colloidal gold nanoparticles (NPs), monolayer protected clusters (MPCs) and biomolecular conjugates, there is a need to interrogate their immediate toxicity. Due to the diverse properties of the gold core nanoparticle such as size, coating, surface functionalization and other physico-chemical properties, a series of different *in vitro* cytotoxicity assays were attempted. The absorption properties and fluorescence quenching properties of gold nanoparticles also played a major role in the subsequent outcomes of the assays. This chapter presents some *in vitro* assay results for ascertaining some toxicity properties of a cross-section of the gold NPs, MPCs and bioconjugates. A choice selection of healthy Chinese ovarian hamster cells (CHO22) and human Jurkat cells were used for this study. This work was carried out in collaboration with Ms. Cleo Dodgen at the University of the Western Cape, Department of Biotechnology, Bellville, RSA, under the supervision of Dr. Mervin Meyer. All the cell

culture work was conducted at the University of Western Cape and the nanomaterials synthesis and characterisation conducted at Mintek laboratories.

## 4.2. EXPERIMENTAL MATERIALS AND METHODS

### 4.2.1. Tissue Culture Media and Cell Lines

Dulbecco's modified eagle medium (DMEM) (with 4.5g/L glucose, Glutamax ™), hams F-12 media (with L-glutamine), RPMI 1640 medium (with L-glutamine), phosphate buffered saline (PBS) (with $CaCl_2$ and $MgCl_2$), trypsin, 100x penicillin-streptomycin and foetal calf serum (FCS). All the cell tissue culture reagents were supplied by Invitrogen. Ethanol (Merck), DMSO (dimethyl sulfoxide) (Sigma), PI (propidium iodide) (Sigma). The cell lines, origin and the media used are tabulated in Table 4.1 below.

Table 4.1 Cell lines

| **Cell line** | **Species of origin** | **Media** |
|---|---|---|
| CHO22 cells | Hamster | Hams F-12 |
| Jurkat cells | Human | Hams F-12 |

### 4.2.2. Cell Culturing

#### *4.2.2.1. Thawing of Cells*

The screw-cap vials containing the frozen cells were removed from storage at -150 °C and placed immediately in a warm 37 °C water bath with constant agitation to thaw the cells rapidly. The contents of the vials were slowly transferred into a 15 mL tube containing 5 mL pre-warmed Hams F-12 media. The tube was then centrifuged at 3000 rpm for two minutes using the Eppendorf Multipurpose Centrifuge, 5800 Series. The resultant supernatant was discarded and the pellet was resuspended in Hams F-12 media and transferred into a 25 $cm^2$ tissue culture flask and incubated in a humidified cell incubator at 37 °C with a 5 % $CO_2$ atmosphere.

#### *4.2.2.2. Trypsinization of Cells*

The cells were viewed under the microsope (Nikon microscope at 20X magnification, images captured using a Leica EC3 digital camera) to assess the degree of confluency (80-90%). The spent Hams F-12 media was discarded and the cell monolayer was washed with PBS. The trypsinization was achieved by pipetting pre-warmed 3 mL of 0.0625% trypsin onto the cell monolayer. The cells were then returned into the incubator for 3 minutes to complete the trypsinization process after which 12 mL Hams F-12 was added to stop the process. The cells were then transferred into labelled cell culture flasks at desired populations and incubated in Hams F-12 media.

#### *4.2.2.3. Cell Seeding*

Adherent confluent cells were trypsinized and centrifuged to remove the spent media and the cells were resuspended in 10 mL Hams F-12 media. The cells were counted by filling the chambered coverslip with 1 mL of the cell suspension and counted on a haemocytometer. Once the correct volume of cells was determined, it was made up to the final volume with complete media. Volumes of 1 mL were then transferred to the required number of wells in a 24-well plate and incubated at 37 °C with 5 % $CO_2$ until they reached 80-90 % confluency.

#### *4.2.2.4. Morphological Analysis*

Throughout the growth and treatment processes, the morphology of cells was monitored with the use of a Nikon microscope at 20X magnification. Images were captured using a Leica EC3 digital camera.

#### *4.2.2.5. Cryo-preservation of Cells*

The cells were brought into suspension by trypsinization and were centrifuged to remove the media. The cell pellet was re-suspended in freeze media composed of 10% of 1%

dimethylsulfoxide (DMSO) and 90 % Hams F-12 media. The cell suspensions were aliquoted (1.5 mL) into sterile 2 mL cryo-vials. The cells were frozen at -80 °C overnight followed by transferring the cryo-vials into a -150 °C freezer for long term storage.

#### *4.2.2.6. Neutral Red Cytotoxicity Assay*

CHO22 cells were seeded at a population of $1.5x10^4$ cells per well in a 96 well plate. The cells were incubated for 24 hours and reached 80-90 % confluency. The spent media was removed and the cells were washed with PBS (0.01 M phosphate buffer, 0.0027 M KCl and 0.137 M NaCl) and 1 μL fresh media was added. The media was then replaced with test nanoparticles mixed with fresh media. The plates were then incubated for 24 hours at 37 °C in a humidified incubator with a 5 % $CO_2$ environment. Following the incubation period, the cells were washed twice with PBS (0.01 M phosphate buffer, 0.0027 M KCl and 0.137 M NaCl) and 100 μL serum free media containing neutral red (100 μg/mL) was added to each well and incubated for 2-3 hours. After the incubation, the cells were washed twice with PBS (0.01 M phosphate buffer, 0.0027 M KCl and 0.137 M NaCl) thereafter 50 μL of dye release agent (a solution of 1 % acetic acid:50 % ethanol) was added to each well and the plates were incubated for a further 10 minutes. The plate was placed on a shaker (Vortex Genie Shaker) for 30 minutes after which the optical density at 540 nm ($OD_{540}$) was determined on a multiwell spectrophotometer.

#### *4.2.2.7. APOPercentage™ Assay* [25]

The cells were plated at a density of $1.5 \times 10^4$ cells per well. The cells were then treated with nanoparticles for 24 hours. Following this, the cells were trypsinized, washed with PBS (0.01 M phosphate buffer, 0.0027 M KCl and 0.137 M NaCl) and stained with APOP*ercentage*™ dye (1:160 dilution) for 30 minutes at 37 °C. The cells were washed with PBS to remove excess dye and the cell staining was measured with flow cytometry at 670 nm (FL3) on a Beacon Dickinson FACScan instrument (BD Sciences). Cells were acquired by setting the forward scatter (FSC) and side scatter (SSC) on a log scale dot plot. A linear histogram dot plot was used to measure APOP*ercentage*™ on the FL-3

channel, which was measured against relative cell number. A minimum of 10 000 cells per sample were acquired and analysed using CELLQUEST Pro software.

## 4.3. RESULTS AND DISCUSSION

### 4.3.1. Gold NPs, MPCs and Bioconjugates

The nanomaterials for testing were synthesised and characterised as described in Sections 2.4 (Table 2.2) and 3.3 (Table 3.2) in the preceding chapters. A selection of the materials was used for the cytotoxicity testing as tabulated below:

Table 4.2. Sample codes of the investigated materials.

| CODE | Au CORE SIZE | SURFACE FUNCTIONALITIES |
|---|---|---|
| SM1 | 14 nm | Citrate |
| SM2 | 16 nm | |
| SM3 | 20 nm | |
| SM5 | 30 nm | |
| ME4 | 5.5 nm | 100 % PEG-COOH |
| ME2 | | 100 % PEG-OH |
| ME7A | | 1 % Biotin |
| ME6B | 14 nm | 10 % Biotin |
| ME1 | | 100 % PEG-OH |
| ME3A | | 100 % PEG-COOH |

| | | |
|---|---|---|
| ME8 | | PEG-NTA-Ni-MAP Kinase |
| ME10 | | Biotin-TAT |
| MG12 | | FAM-TAT (by EDC/NHS) |
| ME14C | | 50 % PEG-NTA (50 % PEG-OH) |

### 4.3.2. Neutral Red Cytotoxicity Assay on CHO22 Cell Lines

The mammalian Chinese hamster ovary (CHO22) cell line was used in the elucidation of cytotoxicity effects of the selected gold nanomaterials by neutral red assay. The CHO22 cell line has been employed extensively in many biopharmaceutical manufacturing studies, ranging from analysis of intermediary metabolisms and cell cycle to toxicology studies. This cell line has been termed as the mammalian equivalent of the model bacterium *E. coli* [27]. Important medical and cell biology breakthroughs, such as the work on mutagenesis of CHO22 cells and auxotroph isolation using CHO22 cells was approved for clinical use in 1987 [28]. A diverse contingent of CHO-based therapeutics continues to revolutionise the field of medicine to this day and holds the key in the therapeutic protein production going forward [27].

For the elucidation of the cytotoxicity of the NPs, MPCs and bioconjugates of gold; the CHO22 cells were treated with the nanomaterials for 24 hours. Two differently sized gold cores were investigated at two doses ($10^{10}$ and 2.5 x $10^{10}$ NPs) (the particle numbers were deduced from the optical absorption peaks of the nanoparticles; using the physical constants of the gold bulk metal). Following the neutral red dye uptake and release; spectrophotometric measurements were done. Viability assay data for comparison of particle functionality, biomolecular functionality and size is presented in Figure 4.1. As shown in the viability quantifications, the gold particles seemed to absorb light as the plate reader operated at the SPR region of the gold nanoparticles.

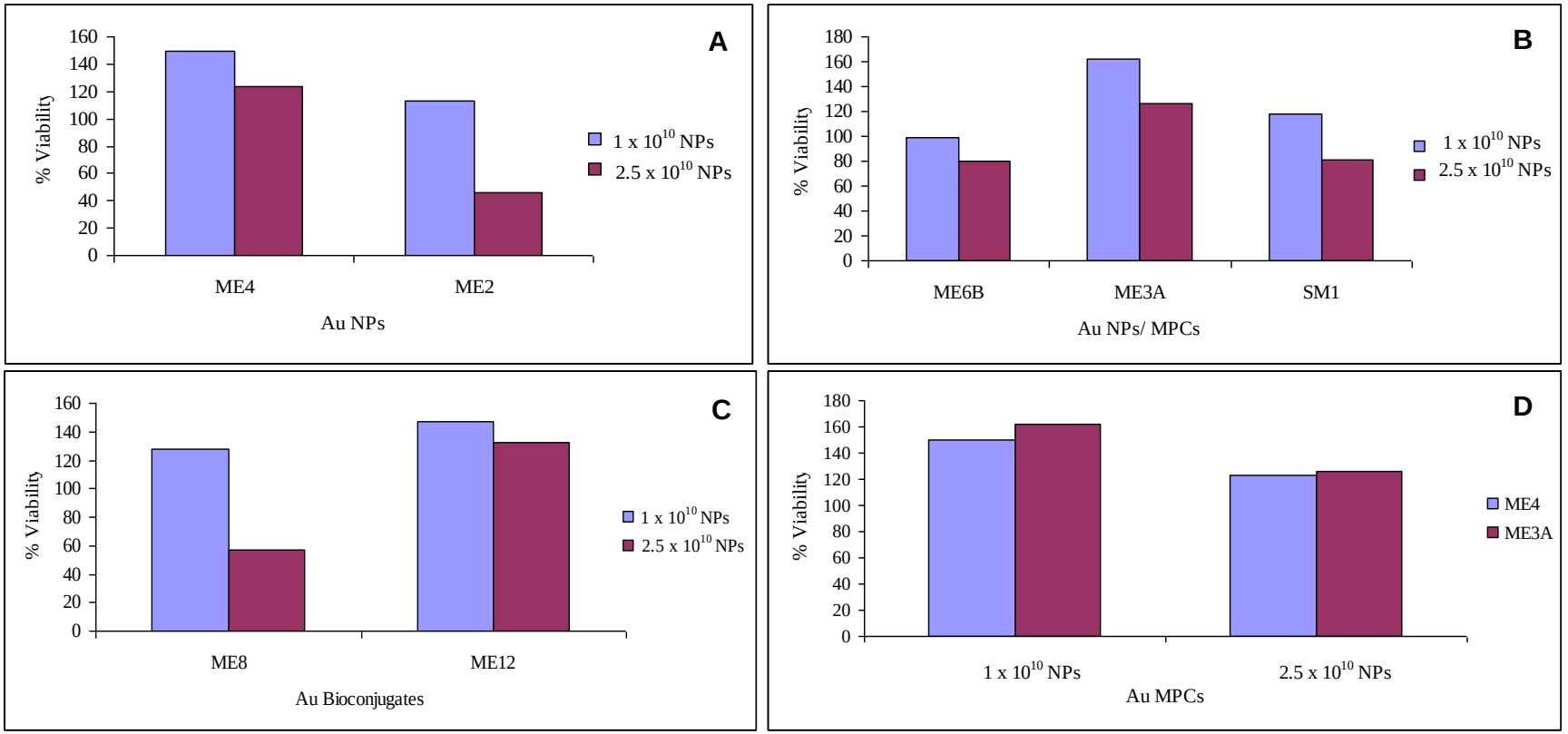


Figure 4.1. *Quantitative representation of the gold MPCs and bioconjugates induced cytotoxicity responses for the CHO22 cells. Functionality-dependent responses of MPCs, 5.5 nm (A) and 14 nm (B), biomolecular functionality comparisons for 14 nm particles (C) and size comparisons for MPCs (1 % carboxy of 5.5 and 14 nm) (D).*

The optical density (absorbance) measurements were therefore biased by the gold nanoparticles and thus exaggerating the subsequent correlations to beyond 100 % viability levels. Despite this drawback, useful observations were made:

i. Dose dependent responses: Cell survival rate of the different gold MPCs and bioconjugates obtained at two concentrations ($1 \times 10^{10}$ and $2.5 \times 10^{10}$ NPs) showed a marked variation with the increase in the concentrations of the test materials. Higher doses of the MPCs and bioconjugates showed lower cell survival rates (Figure 4.1. A, B and C).

ii. Surface functionality dependent responses: Comparison of functionality relationships revealed that PEG-COOH MPCs produced benign responses from the cells. The COOH showed higher survival rate compared with the corresponding OH functionalised MPCs of the same size (5.5 and 14 nm) respectively (Figure 4.1A and B). The OH functionalised MPCs showed a more pronounced response and sensitivity to the dose changes; with the higher dosages showing less viability.

iii. Biomolecular functionality dependent responses: The biomolecular functionality assessment showed a similar dosage response as the MPCs, with the TAT-derivatised conjugates (ME8) showing much higher survival rates. The MAP kinase-functionalised conjugates (ME12) showed less viability as well as a sharp negative response to the dosage increase (Figure 4.1C).

iv. Size dependent responses: The evaluation of two different sizes of similar functionality showed that smaller particles imparted lower survival rates on the cells (Figure 4.1D). The dosage responses of both the sizes (5.5 nm and 14 nm) showed approximately a similar negative response by the cell as the dose increased.

Although the neutral red assay presented a simple, rapid, quantitative assay with reproducible results, the inherent shortfall presented by the absorption of light by the gold nanoparticle cores proved to be a challenge for this protocol to be applied in gold MPCs and bioconjugates cytotoxicity elucidation. A similar shortfall has been observed by

Huang *et al*. in their report of iron oxide cytotoxicity studies [29]. The assay results showed good experimental reproducibility patterns and repeat experiments demonstrated a practically good predictive capability of this assay. Contributions by gold core size, functionality and the subsequent biomolecular functionality were demonstrated.

### 4.3.3. Apoptosis Induction Studies on CHO22 Cell Lines

APOP*ercentage*™ assay was conducted in the investigation of the apoptosis induction capabilities of the different functionalised nanomaterials. The process of apoptosis or programmed cell death is characterised by a sequence of energy-dependent events that culminate in the nuclei fragmentation and the transformation of cytoplasmic organelles into small membrane-sealed apoptotic bodies that can be swiftly and cleanly phagocytosed. During these processes, an externalisation of phosphatidylserine (PS) to the outer leaflet of the cell occurs, this allows the uptake of the APOP*ercentage*™ into the cell [25].

#### *4.3.3.1. The Effect of Gold Nanoparticle Size on Apoptosis*

The CHO22 cells were treated with gold nanoparticles of different sizes for a nominal time period of 24 hours. The time course choice was motivated by the knowledge of the growth and proliferation patterns of the cells and to allow the complete effect of the exposure. Figure 4.2.A depicts the subsequent apoptosis induction abilities of the nanoparticles of sizes 14 nm (SM1), 16 nm (SM2), 20 nm (SM3) and 30 nm (SM5). Relative to the untreated cells (negative) it was observed that the nanoparticles had a benign effect on the cells. The apoptosis ranged between 6 – 8% well within the untreated range. There was however a slight peak for particles at 16 nm, followed by a slight gradual decrease from 20 to 30 nm. Similar observations have been made of size-dependence of apoptosis [30]. The overall dependence of apoptosis to size at this range was shown to be minimal. Factors such as charge, state of aggregation, zeta potential could all contribute, but were not investigated in this study.

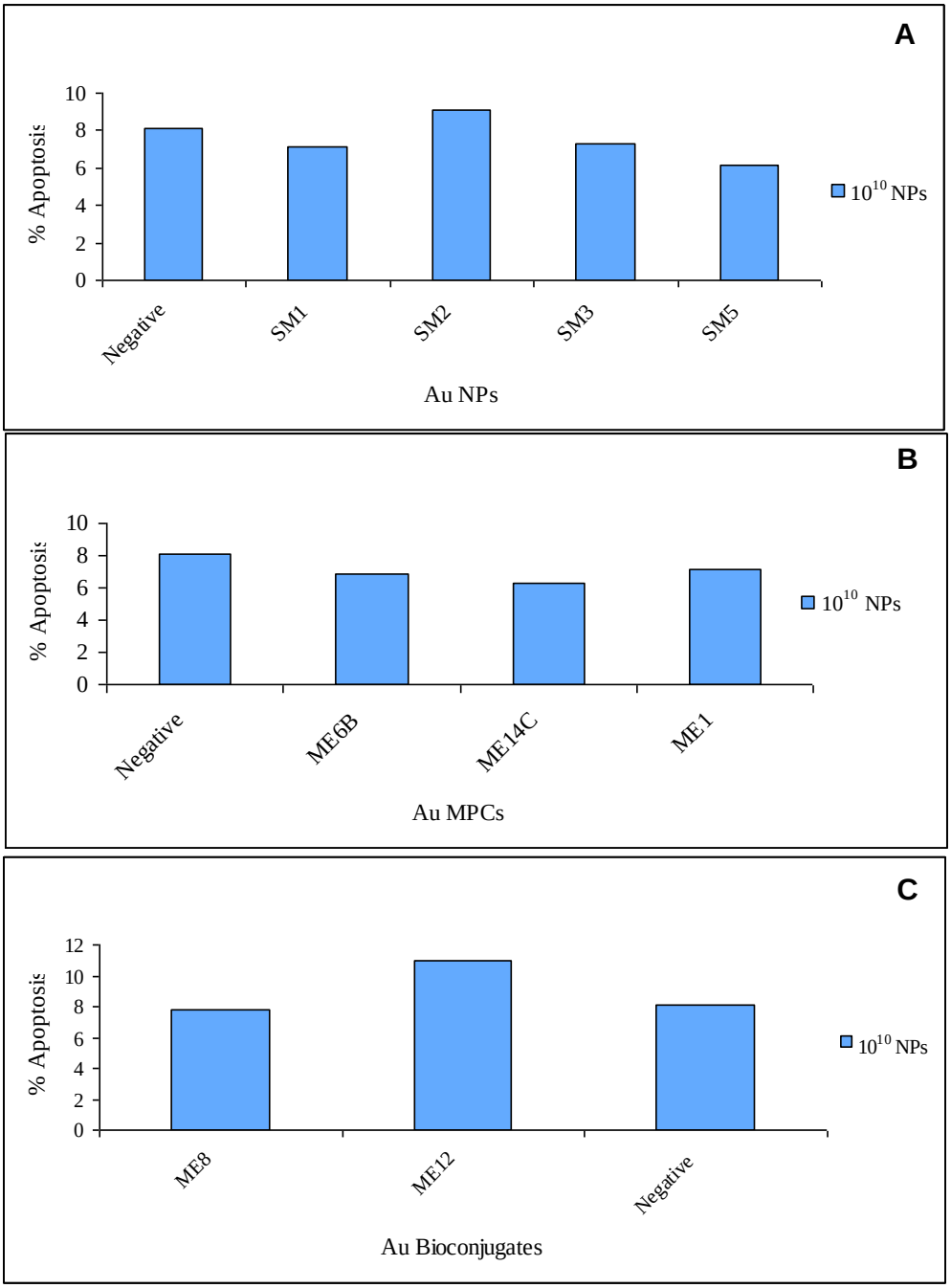


Figure 4.2. *Apoptosis quantification histograms of gold nanoparticles showing size effects (A), MPCs demonstrating the effect of functionality (B) and different bioconjugates (C) on CHO22 cells.*

#### *4.3.3.2. The Effect of MPCs Functionality on Apoptosis*

The effect of the ligand type on the induction of apoptosis by similar sized (14 nm) and shape MPCs (Figure 4.2B) was also investigated. The incorporation of the PEG functionality, which renders the MPCs biocompatible and also imparts the "stealth" character to the MPCs interacting with living systems, adds a dimension onto the expected responses [31]. PEG ligand has also been shown to alter pharmacokinetic properties of delivering parenteral therapeutic reagents [32]. A comparison of three functionalities of MPCs, M6B (10 % biotin), M14C (50 % NTA) and ME1 (100 % OH) showed unremarkable and comparable apoptotic abilities. Compared with the untreated cells, the response levels were relatively similar. These data show that the functionalities alone, coupled with the biocompatible tethered ligand (PEG), have very little effect. A similar observation for a set of different sized nanoparticles was reported by Pan *et al.* [24] showing that naturally benign ligands do not contribute to the outcome of the nanomaterials responses.

#### *4.3.3.3. The Effect of Biomolecular Functionality*

The biomolecular functionality type responses were also investigated as represented in Figure 4.2C. The responses showed very low pro-apoptotic activities. The cell penetrating peptide, TAT conjugates (ME8) showed slightly elevated induction abilities compared with the MAP kinase bioconjugates (ME12). From these observations, it was obvious that the biomolecules on the surface did not add any biologic ability to the core MPCs.

### 4.3.4. Apoptosis Induction Studies on Jurkat Cell Lines

Following the investigation on the CHO22 cell lines, a number of MPCs were investigated in the biologic activities of Jurkat cells. The Jurkat cells are T-lymphocyte-derived cell line, which is known to be apoptosis-sensitive both by the triggering of the intrinsic as well as the extrinsic apoptosis pathways [33]. This cell line has gained recognition in the identification of simple prognostic markers and methods for predicting

the onset and progression of cervical cancer among others [34]. These cells were used as models for apoptosis induction of the gold MPCs.

#### *4.3.4.1. Dose-Dependent Apoptosis Induction in Jurkat Cell Lines*

After treating the Jurkat cells with two doses of the MPCs (ME2 – 100 % OH, 5.5 nm; ME4 – 100 % COOH, 5.5 nm; ME7A – 1 % biotin, 5.5 nm), apoptosis induction was measured via flow cytometry.

Figure 4.3 shows the responses of the cells to the relevant doses. Notable was that the lower doses (1 x $10^{11}$ NPs) showed comparable activities as with the untreated cells. This was in good agreement with the corresponding results for the other cell line (CHO22). However, there was a remarkable jump for the biotin-functionalised MPCs at higher doses (ME7A, 2.5 x $10^{11}$ NPs). This phenomenon was thought to be related with the manner in which biotin may interact with pericellular components.

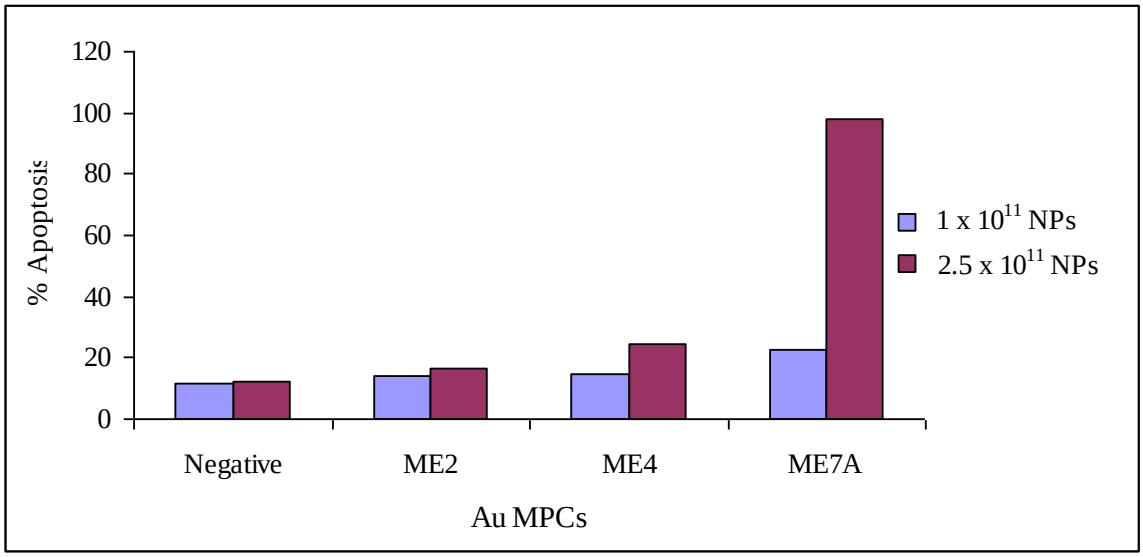


Figure 4.3. *Apoptosis measurements of gold MPCs at two doses on Jurkat cells.*

Biotin is known to bind strongly to glycoproteins, which in turn renders them unsuitable for binding purposes. The two other functionalities, -OH and -COOH, were benign in their activities suggesting no additional activities by the ligand. An increase in the

apoptosis was also observed with the increase in the MPCs dosages. These data presented a platform for the use of MPCs as core carriers in the design of drug and therapeutic delivery systems.

### *4.3.4.2. Cellular Morphological Changes of Jurkat Cell Lines*

Following the treatment of cells (2.5 x $10^{11}$ NPs), the morphological changes were imaged and assessed as presented in Figure 4.4. The process of apoptosis is accompanied by tightly regulated processes including the nuclear condensation and cell shrinkage with plasma membrane preservation. These processes are irreversible and can be visualised by light microscope.

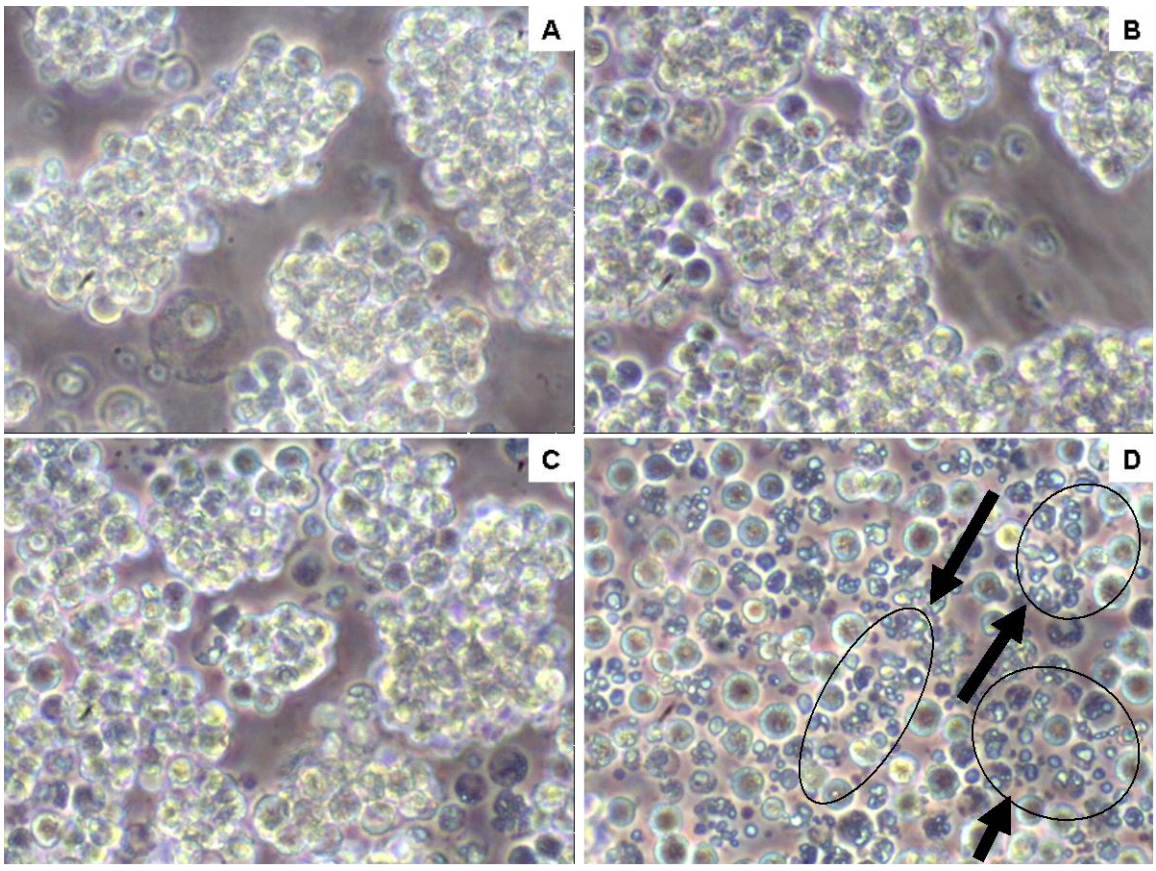


Figure 4.4. *Cellular morphology changes in Jurkat cells treated with 2.5 x $10^{11}$ NPs over a period of 24 hours. PBS treated cells (negative control, A), and the corresponding -OH functionalised (B), -COOH functionalised (C) and 1% biotin functionalised (D) MPCs responses.*

Figure 4.4A shows the untreated Jurkat cells with the expected roundedness and no obvious loss of cell size. Cells treated with hydroxyl (B) and carboxyl (C) functionalised MPCs show cells that have undergone apoptosis, represented as small, bluish-green cells (circled and pointed with bold arrows). Figure 4.4D shows the highly apoptotic cells treated with 1 % biotin functionalised MPCs. As can be seen from the micrograph, small fragments (green, indicated by arrows inside the circles) of the cells dominated the population. This can be expected from the corresponding cytometry quantification (Figure 4.2). The cell membrane preservation on all the cells confirmed that all cell death was via apoptosis only.

## 4.4. SUMMARY AND CONCLUSIONS

In this chapter, descriptions of end-point based cytotoxicity techniques have been illustrated and attempted. The neutral red assay findings showed that all the NPs, MPCs and bioconjugates had high levels of neutral red uptake and retention; signifying the lack of necrotic cell death induction by these materials. Although this assay proved informative, the gold absorption biased the overall optical densities of the uptake dye. The apoptosis induction was investigated using the APOP*ercentage*™ assay. Of note was the benign activities imposed by the test materials on both the CHO22 and Jurkat cells. These findings show a good starting point in the use of these materials for the development of highly functional delivery systems as they inflict minimal biologic response in the cells.

## 4.6. REFERENCES

1. E. Katz and I. Willner, *Angew. Chem. Int. Edit.*, 2004, **43**, 604.
2. Elder A., Yang H., Gwiazda R., Teng X., Thurston S., He H. and Oberdorster G., *Adv. Mater.,* 2007, **19**, 3124.
3. Nel A., Xia T., Madler L. and Li N., *Science,* 2006, **311**, 622.

4. Brunner T.J., Wick P., Manser P., Spohn P., Grass R.N., Limbach L., Bruinink A. and Stark W.J., *Environ. Sci. Technol.*, 2006, **40**, 4374.
5. Connor E.E., Mwamuka J., Gole A., Murphy C.J. and Wyatt M.D., *Small*, 2005, **1**, 325.
6. Goodman C.M., McCusker C.D., Yilmaz T. and Rotello V.M., *Bioconjugate Chem.*, 2004, **15**, 897.
7. Kirchner C., Liedl T., Kudera S., Pellegrino A.M.J., Gaub H.E., Stolzle S., Fertig N. and Parak W.J., *Nano Lett.*, 2005, **5**(2) 331.
8. Goyer R.A., *Am. J. Clin. Nutr.*, 1995, **61**, 646.
9. Ghuitescu L. and GFisman A., *J. Cell Biol.*, 1984, **99**, 639.
10. Parak W.J., Boudreau R., Gros M.L., Gerion D., Zanchet D., Micheel C.M., Williams S.C., Alivisatos A.P. and Larabell C.A., *Adv. Mater.*, 2002, **14**, 882.
11. Warheit D.B., Laurence B.R., Reed K.L., Roach D.H., Reynolds G.A.M. and Webb T.R., *Toxicol. Sci.*, 2004, **77**, 117.
12. Shaw S.Y., Westly E.C., Pitter M.J., Subramanian A., Schreiber S.L. and Weissleder R., *Proc. Natl. Acad. Sci. USA*, 2008, **105** (21), 7387.
13. Judson R., Richard A., Dix D.J., Houck K., Martin M., Kaylock R., Dellarco V., Henry T., Holderman T., Sayre P., tan S., Carpenter T. and Smith E., *Enviro. Health Persp.*, 2008, **1**, 1.
14. Ying Z and WenXin L., *Sci. China Ser. B-Chem.*, 2008, **51**(11), 1021.
15. Daniel C.-M. and Astruc D., *Chem. Rev.*, 2004, **104**, 293.
16. Long T.C., Saleh N., Tilton R.D., Lowry G.V. and Veronesi B., *Environ. Sci. Technol. Technol.*, 2006, **40**, 4346.
17. Tarantola M., Schneider D., Sunnick E., Adam H., Pierrat S., Rosman C., Breus V., Sonnichsen C., Basche T., Wagener J. and Janshoff A., *ACSNANO*, 2009, **3**(1), 213
18. Matzinger P., *J. Immunol. Methods*, 1991, **145**, 185.
19. Carbonari M., Cibati M., Cherich M., Sbarigia D., Pesce A.M. Dell'Anna L., Modica A. and Fiorilli M., *Blood*, 1994, **83**, 1268.
20. DeRenzis F.A. and Schechtman A., *Technol. J. Microtechn. Histochem.*, 1973, **48**, 135.
21. Borenfreund E. and Puerner J.A., *J. Tissue Culture Meth.*, 1984, **9**, 7.

22. a)Borenfreund E. and Puemer J.A., *Toxicol. Lett.*, 1985, **24**, 119; b) Borenfreund E. and Puemer J.A., *Toxicology*, 1986, **39**, 121.
23. Elford W.G., King L.E. and Franker P.J., *Cytometry*, 1992, **13**, 137.
24. Nicoletti I., Migliorati G., Pagliacci M.C., Grignani F. and Riccardi C., *J. Immunol. Methods*, 1991, **139**, 271.
25. Meyer M., Essack M., Kanyanda S. and Rees J.G., *BioTechniques*, 2008, **45**, 317.
26. Koopman G., Reutelingsperger C.P., Kuitjen G.A., Keehnen R.M., Pals S.T. and van Oers M.H., *Blood*, 1994, **84**, 1415.
27. Puck T.T. and Kao F.T., *Proc. Natl. Acad. Sci. USA*, 1967, **58**(3), 1227.
28. Jayapal K.P., Wlaschin K.F., Yap M.G.S. and Hu W.-S., *Chem. Eng. Prog.*, 2007, **103**(7), 40.
29. Huang J.-H., Parab H.J., Liu R.-S., Lai T.-C., Hsaio M., Chen C.-H., Sheu H.-S., Chen J.-M., Tsai D.-P. and Hwu Y.-K., *J. Phys. Chem. C*, 2008, **112**, 15684.
30. Pan Y., Neuss S., Leifert A., Fischler M., Wen F., Simon U., Schmid G., Brandau W. and Jahnen-Dechent W., *Small*, 2007, **3**(11), 1941.
31. Kinstler O., Molineux G., Treuheit M., Ladd D. and Gegg C., *Adv. Drug Deliv. Rev.*, 2002, **54**, 477.
32. Harris J.M., Martin N.E. and Modi M., *Clin. Pharmacokinet.*, 2001, **40**(7), 539.
33. Gottlieb R.A., Nordberg J., Skowronski E. and Babior B.M., *Proc. Natl. Acad. Sci. USA*, 1996, **93**, 654.
34. Aguilar-Lemarroyl A., Romero-Ramos J.E., Olimon-Andalon V., Hernandez-Flores G., Lerma-Diaz J.M., Ortiz-Lazareno P.C., Morgan-Villela G., del Toro-Arreaola S., Bravo-Cuellar A. and Jave-Suarez L.F., *BMC Cancer*, 2008, **8**, 99.

# CHAPTER 5: CONCLUSIONS AND FUTURE OUTLOOK

## 5.1. CONCLUSIONS

The approach of this investigation involved the synthesis of gold nanoparticles and their subsequent conversion to monolayer protected clusters (MPCs). The MPCs were multi-functional and further biofunctionalisation reactions were conducted. Finally, the nanoparticles, MPCs and bioconjugates were subjected to both cytotoxicity and apoptosis-induction studies. In summary, the conclusions that arose are further listed by subject below:

### 5.1.1. Colloidal Gold Nanoparticles and Monolayer Protected Clusters

Gold nanoparticles of different sizes and capping agents were synthesised by various wet chemistry methods. A number of experimental procedures were developed both in aqueous and non-aqueous media and the results were highly reproducible. The citrate-capped colloidal nanoparticles (14 nm) and the borohydride-capped colloidal nanoparticles (6 nm) were envisaged as suitable core materials in the development of highly functional monolayer protected clusters (MPCs) and bioconjugates. The synthesis of monolayer protected clusters (MPCs) was conducted using multifunctional thiolated ligands possessing such groups as $–NH_2$, -COOH and –OH.

The amino residue, L-cysteine and the tripeptide L-glutathione (GSH) were used as capping agents by anchoring through the thiol (-SH) group. The success of these one-step reactions allowed for simple and reproducible introduction of biologically important functionalities. Synthesis following the Brust biphasic approach for the synthesis of long-chain alkulthiol-capped gold MPCs was conducted. This collection of experimental procedures laid a foundation for the development of functionalised hybrid systems for possible biomedical applications.

### 5.1.2. PEGylated Gold Monolayer Protected Clusters

Following the synthesis of colloidal gold nanoparticles, further surface chemistry was conducted in the form of ligand place-exchange reactions. Such reactions enable the fabrication of poly-homo and -hetero-functionalised MPCs which are useful templates for

biomolecular functionalisation. The incorporation of polyethylene glycol (PEG) addressed water solubility, biocompatibily as well as lowering non-specific interactions of nanomaterials with biomolecules. This was conducted via ligand place-exchange reactions employing the citrate- (14 nm) and borohydride-capped (6 nm) colloidal gold nanoparticles as the core. The (mixed) monolayer protected clusters (MPCs) were hydrophilic and stable throughout all environments. The thioalkylated-PEG (PEG-SH) ligand was used as a heterobifunctional stabiliser equipped with a secondary functional group for the facile attachment of further biomolecules on the surface. Hydroxylated, carboxylated, biotinylated and nitrilotriacetic acid (NTA)-derivatised PEG-SH were successfully introduced onto the surface of borohydride- and citrate-capped colloidal gold nanoparticles.

The high stability of the PEGylated MPCs allowed for their use in the introduction of further biomolecules on the particle surfaces. The –COOH-derivatised MPCs were assigned as precursors for the attachment of amine-functionalities on the surface via the carbodiimide coupling reaction, whereas the nitrilotriacetic acid (NTA) functionalised MPCs offered a perfect platform for the surface introduction of hexahistidine-tagged biomolecular functionalities. The biotinylated MPCs were assigned as core materials for the introduction of streptavidin on the surface via the strong biotin-streptavidin binding affinity. Overall, the preparation of the PEGylated MPCs proved to be versatile and reproducible.

### 5.1.3 Gold Bioconjugates

Applications of nanoparticle systems in targeted drug delivery and diagnostics requires the immobilisation of relevant biomolecules on the surface of gold MPCs. A number of biomolecules were introduced on the gold MPCs using various reactions. The introduction of streptavidin protein, on the surface of carboxylated PEG-SH functionalised gold MPCs was conducted via the carbodiimide coupling reaction. This approach offered a simple two-step route for the development of stable biomolecular conjugates. Due to the high number of amine-containing biomolecules, this method holds promise in their incorporation onto gold MPCs. Streptavidin was also introduced onto the surface of biotinylated gold MPCs by the direct attachment onto biotinylated gold

MPCs. Another biotinylated functionality, biotin-TAT, was immobilised on the streptavidin protein via the biotin-(strept)avidin-biotin (BAB) interaction. The resultant bioconjugates were highly stable.

A second approach for the introduction of a TAT peptide was successfully attempted via the carbodiimide coupling protocol using fluorescence-labelled TAT peptide; FAM-TAT on the streptavidin gold conjugates (6 and 14 nm). This was done by amide bond formation between the –COOH group of the streptavidin and the $–NH_2$ of the peptide. The cell penetrating TAT peptide (YGRKKRRQRRR) is a well established and potent intracellular delivery agent that translocates via a lipid raft-dependent process into the cells. Coupled with gold particles, the method presented an excellent delivery vehicle. The introduction of hexahistidine-tagged mitogen-activated protein kinase (MAP kinase) was conducted through the Ni-NTA affinity protocol. Firstly, bivalent hexadentate Ni(II) was introduced into the NTA matrix of the MPCs to form a Ni(II) chelate species. The resultant gold MAP kinase bioconjugates showed good stability. The simplicity of this approach gave rise to its possible application as a liquid phase probe for the purification and quantification of tagged fusion biomolecules.

### 5.1.4. Cellular Interactions of Colloidal Gold Nanoparticles, MPCs and Bioconjugates

Due to the intended applications of the colloidal gold nanoparticles, MPCs and bioconjugates in drug delivery and diagnostics, their inherent biologic effects were studied. This study was done to ascertain some biological responses caused by these materials through a series of end-point based *in vitro* assays. An investigation into the cytotoxicity of these nanomaterials was conducted via the neutral red assay on CHO22 cells. A general decrease in cell survival rates was observed with an increase in doses across all the different test gold NPs, MPCs and bioconjugates. A comparative study of the sizes, surface functionality (MPCs) and biomolecular functionality was conducted. This assay proved to be a simple tool for the elucidation of cytotoxicity of these materials although the gold absorption hampered the readings.

A second approach investigating further into the apoptosis induction by gold NPs, MPCs and bioconjugates was conducted using the APOP*ercentage*™ assay. A general

observation was that the materials impose very little apoptosis activity on the cells. As well, the APOP*ercentage*™ assay proved invaluable for the elucidation of nanomaterial apoptosis induction. The technique was also applied successfully in Jurkat cells. Overall, the gold NPs, MPCs and bioconjugates showed low cytotoxicity margins and thus will be suitable for biomedical applications.

## 5.2. FUTURE OUTLOOK

Applications of the techniques developed for the biomolecular functionalisation of gold monolayer protected clusters are currently being evaluated as possible replacements for conventional methods such as solid-phase protein harvesting. The prospective use of L-glutathione-derivatised gold MPCs for possible trapping and purification of glutathione *S*-transferase (GST)-tagged fusion proteins is currently in feasibility studies. This approach would offer a cheap and fast probe towards protein beneficiation. A similar approach has been designated for the use of Ni-NTA-derivatised gold MPCs for the beneficiation of hexahistidine-tagged fusion proteins. These two systems would offer simple liquid phase probe alternatives to the common costly solid phase approaches.

The attractive properties of nanosized gold materials, based on their size have shown the possibility of drawing many uncertain biologic effects, when their physico-chemical properties are evaluated. Further cytotoxicity studies are being conducted to extend the scope of the work explored herein. Various mammalian cells have been identified, both healthy and diseased, and are currently being investigated. In future, other aspects of the gold nanomaterials will be incorporated, such as the shape, charge, zeta potentials, state of aggregation and other physico-chemical properties. Other aspects such as exposure duration, media-nanoparticle interactions, generation of reactive oxidative species (ROS) as well as house-keeping molecules will be investigated.

Findings reported in this work have strengthened the case for the use of these gold nanoparticles, monolayer protected clusters and bioconjugates as core carriers in targeted drug delivery studies and in diagnostics applications. A series of differently sized gold nanoparticles are currently being evaluated in various human cancerous cell lines for their potential as delivery vehicles for antiangiogenic drugs. Other avenues being explored include the use of the gold nanoparticles as carriers for pro-apoptotic agents and their

evaluation in cancer treatment. The power of these materials lies in their versatility and the many possibilities associated with their surface chemistry.